

General Disclaimer

One or more of the Following Statements may affect this Document

- This document has been reproduced from the best copy furnished by the organizational source. It is being released in the interest of making available as much information as possible.
- This document may contain data, which exceeds the sheet parameters. It was furnished in this condition by the organizational source and is the best copy available.
- This document may contain tone-on-tone or color graphs, charts and/or pictures, which have been reproduced in black and white.
- This document is paginated as submitted by the original source.
- Portions of this document are not fully legible due to the historical nature of some of the material. However, it is the best reproduction available from the original submission.

NASA CR-137,857
Available to the Public

**GROUND SIMULATION AND TUNNEL BLOCKAGE
FOR A JET-FLAPPED, BASIC STOL MODEL
TESTED TO VERY HIGH LIFT COEFFICIENTS**

(NASA-CR-137857) GROUND SIMULATION AND
TUNNEL BLOCKAGE FOR A JET-FLAPPED, BASIC
STOL MODEL TESTED TO VERY HIGH LIFT
COEFFICIENTS (Lockheed-Georgia Co.)
HC \$6.00

N76-28227

133 p
CSCL 01C G3/05
Unclass
47837

By

J. E. Hackett
R. A. Boles
D. E. Lilley

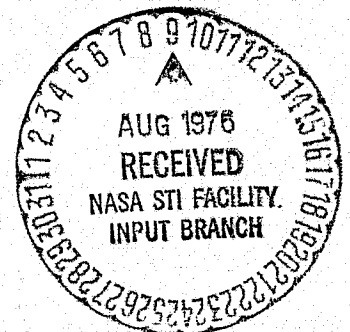
MARCH 1976

Distribution of this report is provided in the interest of
information exchange. Responsibility for the contents
resides in the authors or organization that prepared it.

Prepared under Contract No. NAS2-8745 by
LOCKHEED-GEORGIA COMPANY
Marietta, Georgia

for Ames Research Center

NATIONAL AERONAUTICS AND SPACE ADMINISTRATION



CONTENTS

Section	Page
LIST OF FIGURES	v
LIST OF SYMBOLS	x
SUMMARY	xii
1. INTRODUCTION	1
2. WIND TUNNEL MODELS AND THEIR CALIBRATION	3
2.1 The Basic Model	3
2.2 Slot Momentum and Thrust Calibrations	4
3. TEST FACILITIES, INSTRUMENTATION, AND SCHEDULES	5
3.1 The Lockheed-Georgia 30' x 42' Low Speed Wind Tunnel	5
3.2 The NASA/AAMRDL 7' x 10' Wind Tunnel	5
3.3 Ground Plane Configurations	6
3.4 Data Reduction	7
3.5 Test Section Flow Calibration and Control in the 30' x 42' Tunnel	7
3.6 Run Schedules and Procedures	8
4. WIND TUNNEL INTERFERENCE STUDIES: INTRODUCTION	11
4.1 The General Nature of the Flow	11
4.2 Flow Near the Tailplane Position	12
4.3 Wing Aerodynamics	14
5. WIND TUNNEL INTERFERENCE STUDIES: "PRODUCTION" RUNS	15
5.1 Wind Tunnel Correction Equations	15
5.2 General Comments	16
5.3 Test Results for Basic Configurations (A1 and F)	16
5.4 Configurations with Tips (B, G, and E)	17
5.5 Tailplane effects	18
5.6 Review of Force and Moment Results in Two Tunnels	19
5.7 Discussion of Wind Tunnel Blockage Corrections	20
6. GROUND EFFECTS EXPERIMENTS: INTRODUCTION	22
6.1 Determination of Ground-Blowing Requirements	22
6.2 Skin Friction at the Ground	23
6.3 Tailplane Setting Angle	24
6.4 Flow Measurements Near the Tail Position	24
6.5 Limit Lift in Ground Effect	25

Section	Page	
7.	GROUND EFFECTS EXPERIMENTS: "PRODUCTION" RUNS	27
	7.1 General Comments	27
	7.2 Lift and Drag in Ground Effect	27
	7.3 Pitching Moments Tail-off and Tail-on	28
	7.4 Discussion	29
	7.5 Tests with Simulated Strut Shrouds	30
	7.6 Summary	30
8.	CONCLUSIONS AND RECOMMENDATIONS	32
	8.1 Wind Tunnel Interference Studies	32
	8.2 Ground Effects Experiments	33
	8.3 Tests with Simulated Strut Shrouds	34
	8.4 Recommendations	35
9.	REFERENCES	36
	TABLE OF MODEL DIMENSIONS	37
	APPENDIX	39
	FIGURES	41

LIST OF FIGURES

Figure Number	Title	Page
1.1	Model tested under Contract No. NAS2-6690	41
1.2	Formation of a trapped, underwing vortex at low altitude and high jet momentum	42
1.3	The present KBF model (configuration A2) in the Lockheed 30 x 42 Inch Wind Tunnel (moving ground present)	43
1.4	Configuration H in the NASA/AAMRDL 7 x 10 Foot Wind Tunnel	44
2.1	Model general arrangement	45
2.2	Model wing section ordinates	46
2.3	Balance and air-bridge details	47
2.4	Dynamic and static pressure tare calibration rig	48
2.5	Axial force pressure tare	49
2.6	Static thrust calibration	50
3.1	The 30 x 42 Inch Low-Speed Wind Tunnel	51
3.2	The moving belt ground plane	52
3.3	The boundary layer control ground plane	53
3.4	Dimensions of the moving belt and the blown ground planes	54
3.5	On-line generation of corrected 'q'	55
3.6	Run schedule for center tunnel production runs	56
3.7	Run schedule for ground effects production runs	58
4.1	Conditions for floor impingement: basic configuration (A-1)	60
4.2	Lift and center tunnel: fixed versus moving ground	61
4.3	Cross-flow vectors just aft of tailplane position (x/c = 3.88)	62

Figure Number	Title	Page
4.4	Upwash angles in the vicinity of a flap-end vortex	63
4.5	Measured vortex positions in large and small wind tunnels, $x/c = 3.88$	64
4.6	Measured trailing vortex positions in large and small wind tunnels (tabulation), $x/c = 3.88$	65
4.7	Conditions for positive and negative tail stall	66
4.8	Upwash aft of tailplane location in large and small tunnels. Basic configuration (A) with and without tailplane, $\alpha = 0$	67
4.9	Upwash aft of tailplane location in large and small tunnels. Configuration with tips (B) at $\alpha = 0^\circ$	68
4.10	Lift performance in relation to 'limit lift'	69
4.11	Typical stall patterns, from tuft observations, $C_{\mu} = 2.0$	70
4.12	Conditions for wing stall	71
5.1	Application of corrections to small tunnel results	72
5.2(a)	Basic lift data, basic wing with slats (A1)	73
5.2(b)	Basic drag data, basic wing with slats (A1)	74
5.2(c)	Basic pitching moment data, basic wing with slats (A1)	75
5.3(a)	Basic lift data, basic wing - slats removed (F)	76
5.3(b)	Basic drag data, basic wing - slats removed (F)	77
5.3(c)	Basic pitching moment data, basic wing - slats removed (F)	78
5.4(a)	Basic lift data, with tips - fully slatted (B)	79
5.4(b)	Basic drag data, with tips - fully slatted (B)	80
5.4(c)	Basic pitching moment, with tips - fully slatted (B)	81
5.5(a)	Basic lift data, with tips - outer slat removed (G)	82
5.5(b)	Basic drag data, with tips - outer slat removed (G)	83

Figure Number	Title	Page
5.5(c)	Basic pitching moment data, with tips - outer slat removed (G)	84
5.6(a)	Basic lift data, with tips - inner slat removed (E)	85
5.6(b)	Basic drag data, with tips - inner slat removed (E)	86
5.6(c)	Basic pitching moment data, with tips - inner slat removed (E)	87
5.7	Tail-on and tail-off pitching moments, basic configurations (A1, A2)	88
5.8	Tail-on and tail-off pitching moments, with tips (B, C)	89
5.9	Summary of small/large tunnel comparisons for basic configurations	90
5.10	Summary of small/large tunnel comparisons for tipped configurations	91
5.11	Effect of solid blockage on wake blockage corrections	92
6.1	Ground effect on undersurface pressures	93
6.2	Effect of ground BLC on sectional lift coefficient, $2y/b = 0.643$	94
6.3	Floor tangential-blowing requirements derived via pressure investigations. (Adapted from NASA CR114496, Figure 42)	95
6.4	Typical moving and ground BLC test results	96
6.5	Blowing BLC requirements from lift considerations	97
6.6	Flow conditions at ground	98
6.7	Conditions for negative tail stall and wing wake penetration (moving ground)	99
6.8	Geometry of tailplane and flow measurements	100
6.9	Flow angles at the tail: Blown and moving ground	101
6.10	Limit lift in ground effect (basic configuration, moving ground)	102

Figure Number	Title	Page
7.1	Basic lift data in ground effect, $h/c = 1$, basic wing with slats (A1)	103
7.2	Basic lift data in ground effect, $h/c = 1$, with tips, fully slatted (B)	104
7.3	Basic lift data in ground effect, $h/c = 2$, basic wing with slats (A1)	105
7.4	Basic lift data in ground effect, $h/c = 2$, with tips, fully slatted (B)	106
7.5	Basic drag data in ground effect, $h/c = 1$, basic wing with slats (A1)	107
7.6	Basic drag data in ground effect, $h/c = 1$, with tips, fully slatted (B)	108
7.7	Basic drag data in ground effect, $h/c = 2$, basic wing with slats (A1)	109
7.8	Basic drag data in ground effect, $h/c = 2$, with tips, fully slatted (B)	110
7.9	Pitching moments in ground effect, $h/c = 1.0$, basic configurations (A1, A2)	111
7.10	Pitching moments in ground effect, $h/c = 1.0$, with tips, fully slatted (B, C)	112
7.11	Pitching moments in ground effect, $h/c = 2.0$, basic configurations (A1, A2)	113
7.12	Pitching moments in ground effect, $h/c = 2.0$, with tips, fully slatted (B, C)	114
7.13	Ground blowing pressures for flow attachment and possible associated lift results	115
7.14	Effect of Support Strut Fairings on Lift, $h/c = 1$	116
7.15	Effect of Support Strut Fairings on Drag, $h/c = 1$	117
7.16	Effect of Support Strut Fairings on Pitching Moment, $h/c = 1$	118
7.17	Effect of Support Strut Fairings on Lift, $h/c = 2$	119

Figure Number	Title	Page
7.18	Effect of Support Strut Fairings on Drag, $h/c = 2$	120
7.19	Effect of Support Strut Fairings on Pitching Moment, $h/c = 2$	121

LIST OF SYMBOLS

A_{noz}	Blown flap slot area
b	Base model wing span
BLC	Boundary layer control
c	Nominal wing chord
C_D	Drag coefficient, based on S
\bar{C}_D	Blown flap slot discharge coefficient
C_L	Lift coefficient, based on S
C_{L_T}	Circulation lift coefficient (lift minus vertical component of thrust)
C_{ℓ}	Lift coefficient, based on c
C_{ℓ_h}	Lift coefficient, based on h
C_m	Pitching moment coefficient, based on S , about wing $1/4 c$
C_N	Normal force coefficient, based on S
C_p	Static pressure coefficient $(p - p_0)/q$
C_T	Thrust coefficient, based on S
C_1	Tunnel working section area
C_μ	Momentum coefficient, based on S
FRL	Fuselage reference line
GP	Ground plane
H	Total pressure in model
H_c	Total pressure at tunnel contraction entrance
h	Model height above ground plane
i_H	Tailplane incidence, leading edge raised
KBF	Knee-blown flap
LE	Leading edge
M	Mach number

N	Floor blowing parameter - see Figures 6.1 through 6.3 and Reference 1
p	Local static pressure
p_c	Static pressure at working section entry (contraction piezometer ring, wall orifices only)
p_o	Static pressure at model station
q	Dynamic pressure
q_{uc}	Uncorrected dynamic pressure
S	Wing area
U_∞	Free-stream velocity
v	Lateral velocity component
w	Vertical velocity component
X	Distance measured axially downstream from model wing 1/4 chord
Y	Distance measured laterally from tunnel centerline
Y_l	Lower surface wing ordinate
Y_u	Upper surface wing ordinate
Z	Distance measured vertically from tunnel floor
α	Angle of attack
γ	Ratio of specific heats
ΔC_{p2}	Model induced change in the mean of the upstream and downstream working section mean static pressure
ΔP	Static pressure rise through the tunnel contraction section: ($H_c - p_c$)
δ	Incidence correction factor
ϵ_s	Solid blockage coefficient
ϵ_w	Wake blockage coefficient
ρ	Air density

SUMMARY

Ground effects experiments and large/small-tunnel interference studies were carried out on a model with a 20-inch (50.8 cm) span wing. The wing, which includes a highly deflected knee-blown flap can be fitted with unflapped tips and slats. A low-mounted tailplane can be fitted to the aft fuselage.

Three-component balance measurements, made with a fixed ground equipped with a single boundary-layer blowing slot, were compared with datum, moving-ground results. Good comparisons were obtained up to model blowing momentum coefficients of approximately two, after which the particular floor blowing settings used proved insufficient to prevent floor separation in the vicinity of the model. Skin friction measurements, taken routinely along the floor centerline, proved invaluable during the analysis of results and their use is recommended as input to determination of floor BLC setting. A careful investigation was made of pitching moments, including tail-on, close-to-ground cases, with favorable results. Somewhat surprisingly, drag proved the most sensitive to the change from a moving to the boundary-layer controlled ground

Matched sets of center-tunnel high-lift tests were made on the same model in the NASA/AAMRDL 7' x 10' Wind Tunnel and in the Lockheed-Georgia 30" x 42" Low-Speed Wind Tunnel. Wake blockage corrections, derived from working section entry and exit pressures, were applied in real time to provide "corrected q" in the working section of the small tunnel. The moving ground was run routinely in that tunnel. Tests extended to extremely high C_{μ} 's (up to 10) and three-dimensional circulation lift limits were noted. Detailed pitch/yaw probe measurements in the two tunnels showed that, for the attached flow configurations, the reduced vortex wake penetration into the smaller tunnel was consistent with the flow rotation correction applied during constraint corrections to angle of attack. Good comparisons were obtained between large-tunnel and corrected small-tunnel force and moment results provided the inner wing was unstalled. Once strong separation existed ahead of the powered flap, in the small tunnel, drastic reductions in drag were encountered, though with little modification to lift. A full explanation for this has not been found. However, it is noted that the blockage correction method used does not include allowance for stall-induced changes in solid blockage (stall bubble), and excessive on-line speed corrections may have been applied.

A copy of this document is retained in the Lockheed-Georgia Company Engineering Report files. The identifying report number is LG76ER0047.

ACKNOWLEDGEMENT

The authors are grateful to Georgene Laub and the operating staff of the U. S. Army Air Mobility Research Laboratory 7 x 10-Foot Wind Tunnel at Moffett Field, California, for their able assistance and dedication during the "large tunnel" experimental phase of this program.

1. INTRODUCTION

Large-scale tests on powered, STOL models can experience at least two major difficulties in establishing confidence in the results of wind tunnel tests. The first concerns the application of wind tunnel blockage corrections and the second arises during ground effects testing over a non-moving tunnel floor or ground board which frequently is the only option at large scale. Here, ground (or tunnel floor) separation can invalidate the results of high lift tests.

In studies sponsored by NASA-Ames (see refs. 1 to 3), the problem is addressed of simulating a moving ground without actually having one. This is most desirable because of the logistic and operational problems associated with the belt-type of moving ground at large scale. Figure 1.1 shows a knee-blowing, jet-flapped model used in the above studies mounted over a moving ground in the Lockheed-Georgia 30' by 42' (76.2 cm x 106.7 cm) Low Speed Wind Tunnel. These tests showed that, even with a moving ground present, a vortex could be trapped below the wing under high-lift, near-ground conditions in the manner shown in Figure 1.2. A scheme was devised and tested (ref. 2) which employs a fixed floor with tangential blowing to reproduce such flows. Check-out required extensive pressure plotting studies which included a configuration with a fuselage-mounted, round lifting jet. On the basis of techniques developed during these tests, a design study was carried out for application of floor-blowing technique in the NASA-Ames 40' by 80' Wind Tunnel (ref. 3). However, it was felt that a broader investigation including balance measurements over a range of configurations was desirable before the scheme should be implemented.

In 1973, an independent study was carried out by Lockheed in which a modified version of the above model was tested in the above Lockheed tunnel and then in the Lockheed 23 $\frac{1}{4}$ ' ft. by 16 $\frac{1}{4}$ ' ft. (7.08 m by 4.95 m) wind tunnel. This was an investigation of a newly devised method for estimating wake blockage from pressure measurements at the upstream and downstream ends of the test section (ref. 4). Modifications were made to the model at this time including replacement of the fuselage by a simple hollow sting which carried the air supply and a reduction in knee slot height from 0.114 cm (0.042") to approximately 0.041 cm (0.016") in order to reduce unwanted spanwise flows (ref. 2). Pressure plotting techniques were still employed, however. The new wake-blockage method successfully reproduced large-tunnel lift coefficients, in the small tunnel, up to the maximum C_L tested, fifteen. Since no corrections were attempted for solid/bubble blockage, this result testifies to the aerodynamic cleanliness of the model. [Hackett and Wilsden (ref. 5) have recently shown that blockage due to separated flows may also be estimated from wall pressures, but these are required along the entire test section length.]

The present test series represents a continuation of both ground blowing and tunnel blockage investigations along the lines suggested by previous studies (ref. 4). Removable tips were made which could increase the model span from 50.8 cm (20") to 76.2 cm (30"). A detachable tailplane was also fitted. A three-component balance and an air bridge were installed in the

model, covered by a minimum fairing as shown in Figure 1.3. This provided the important advantage of permitting varying incidence runs. With previous pressure plotting techniques, this was largely precluded because of the volume of data involved.

In the present tests the moving ground was again the obvious baseline for the blown-ground tests. For the interference-free "free air" datum needed for the tunnel corrections investigation, the AAMRDL 7' x 10' (3.04 x 2.13 m) tunnel was used (see Figure 1.4). A total of 418 runs were made in the smaller tunnel and 100 were made at the AAMRDL. Of these, about 80% were force tests, the balance being flow investigations of various kinds. Further details of the model, its variants, and its calibrations are given in Section 2. Section 3 describes test facilities, the associated calibrations, and test techniques.

To establish model properties out of ground effect, the wind tunnel blockage studies are described first in Sections 4 and 5. These concern fairly extensive flow investigations and "production" three-component balance runs, respectively. The overall objectives were to verify the previous blockage correction results via balance measurements and to extend the range of configurations tested. A very specific objective was to determine the conditions under which corrections for wake blockage (together with conventional image corrections) was adequate. This is important because the methods for evaluation of solid blockage (ref. 5) are more difficult to apply, on line. For this reason, the model was deliberately stalled by selective removal of slats in some tests.

The objectives of the ground effects experiments (Sections 6 and 7) again concerned broader verification across various model configurations. Of particular concern was the fact that the rather thick blown-boundary layer might interfere with pitching moments. Accordingly, a low-mounted tailplane was fitted to the model in order to provide a severe test of the method. In a subsidiary investigation, dummy support strut shrouds were mounted beneath the model at one chord and again at two chords altitude. Toe-in angle was varied in relation to the local, underwing flow angle and the effects on force balance were recorded. Ground blowing BLC was employed.

Overviews of results from the tunnel blockage and ground-blowing investigations may be found at the ends of Sections 5 and 7, respectively. Conclusions and recommendations are given in Section 8.

2. WIND TUNNEL MODELS AND THEIR CALIBRATION

2.1 The Basic Model

Figure 2.1 shows the model with tips fitted, supported by its air supply pipe. The low wing has a span of 76.2 cm (30") and tip chord of 12.78 cm (5.02") giving a reference area of 973.8 sq cm (1.048 sq ft.). However, for continuity with previous results (ref. 2), the basic tips-off reference dimensions are used in the majority of this report. These are: span, 50.8 cm (20"); chord, 10.16 cm (4"); and area 516.1 sq cm (0.556 sq ft.).

The inboard airfoil section (Figure 2.2) is derived from a supercritical design, thickened on the lower surface to approximately 16% total thickness and modified to accommodate an internal air duct and a fixed, highly deflected flap with knee blowing. The slot upper member is supported by posts at intervals along the span, giving a mean gap of .0415 cm (.0163 in.), which increases when pressurized. C_{μ} values up to 6.0 were employed at a tunnel 'q' of 5 psf (239.4 N/sq.m), requiring a pressure ratio of approximately 3.2 in the plenum. Higher C_{μ} 's were obtained at reduced tunnel speed.

The tip section was designed as a compromise fairing which fitted to the main wing with minimal spanwise discontinuities. Slats can be fitted separately to basic wing and to the tip extensions. A tailplane (Figure 1.3) of 25.4 cm (10") span and 6.35 cm (2.5") chord can be fitted at several setting angles. It has an inverted St Cyr 244 section. This section, which is defined in *Aviation Handbook* by Warner and Johnston (McGraw-Hill, 1931), was chosen for its high stall angle characteristics at low Reynolds number.

The rather deep fuselage fairing accommodates a strain gauged sting balance with a bellows-type air bridge mounted above it. Though this introduces fairly high axial loads, these oppose drag forces and can be calibrated accurately. Internal total tubes and static orifices were used for measurement and control of slot blowing rates.

The model sting was attached to an incidence quadrant mounted beneath the wind tunnel floor. Incidence was measured using an accelerometer attached to this quadrant. For ground effects testing, the quadrant, sting, and model were raised and lowered as a unit by means of a permanently installed hydraulically powered lift table. Generally similar arrangements were used in the NASA/AAMRDL tunnel. However, it was more convenient to test the model in the inverted position in this facility.

2.2 Slot Momentum and Thrust Calibrations

Considerable care was necessary in these calibrations because the model slot opened somewhat under pressure and because the air bridge bellows area was not sufficiently large that dynamic tares (momentum flux) could be neglected. This yielded the equation

$$\frac{A_{noz}}{S} = 0.0336 + 0.00061 \left(\frac{H}{P_0}\right) \quad (2.1)$$

where S is the without-tips reference area. This equation was used in conjunction with the conventional expression for momentum coefficient, namely

$$C_{\mu} = \gamma \tilde{C}_D M^2 \left(\frac{P_0}{q}\right) \left(\frac{A_{noz}}{S}\right) \quad (2.2)$$

where \tilde{C}_D is a slot discharge coefficient, taken as 0.98 and Mach number is derived from

$$M^2 = \left(\frac{2}{\gamma-1}\right) \left\{ \left(\frac{H}{P_0}\right)^{\frac{\gamma-1}{\gamma}} - 1 \right\} \quad (2.3)$$

Since the varying slot area affects the axial force tare on the air bridge and because of the impact on drag measurements, a special dynamic tare calibration rig was made (Figure 2.4). This replaced the model wing with a spanwise plenum with long carefully aligned holes drilled at each end. Directing the air spanwise at right angles to the balance axis and in opposite directions permitted full mass flows to be passed through the air bridge without any lift drag or pitching moment due to jet reaction. Bellows tares could then be directly measured by the balance at various exit areas depending upon the number of holes left open. The effect on the slope of the drag tare calibration may be seen in Figure 2.5. There is about a 6% change over the test range. Similar plots were produced for lift and pitching moment.

Figure 2.6 shows the result of a static test on the basic wing over the full pressure range to be used in the tunnel. Thrust coefficient is very closely proportional to $(H/P_0 - 1)$ and lies somewhat below the calculated momentum curve as is usually the case. Turning improves fairly rapidly up to a thrust coefficient of two and asymptotes to about 68 degrees thereafter. The upper surface angle of the flap is 76 degrees. Comparison with pressure and trailing edge traverse integrations quoted by Hackett and Lyman (ref. 10) showed close correspondence with C_T (Figure 2.6) up to a value of about three. Further details of flow distributions are quoted in the same reference.

3. TEST FACILITIES, INSTRUMENTATION, AND SCHEDULES

3.1 The Lockheed-Georgia 30" x 42" Low Speed Wind Tunnel

The tunnel is located at the Lockheed-Georgia Company Research Laboratory. The test section nominal dimensions give a height-to-width ratio of 0.7 and a cross-sectional area of 0.814 square meters. The tunnel, shown in Figure 3.1, utilizes a constant-speed motor running at 1200 rpm and rated at 400 horsepower. A 6-foot (1.82 m) diameter fan is manually controlled by an eddy current variable speed unit.

The model was sting mounted via an internal three-component strain gauge balance. The sting is attached to a motor-driven quadrant for attitude control. Three ganged 48-port type D3 scanivalves were used for model internal and supply pressures, boundary layer control box, Preston tubes and boundary layer rake pressures, and tunnel wall static pressures. An additional single scanivalve was used for acquiring the 35 pressures of the rake of seven five-holed probes. A 250 psi transducer was used for the internal and supply pressure and 2.5 psi transducers for all the others.

The tunnel speed was maintained manually utilizing a display of corrected dynamic pressure, which is described further in Section 3.5. The mass flow through the model was initially measured with an orifice in the auxiliary air supply line. This permitted estimation of the discharge coefficient at the blown flaps at which time the orifice was removed and all subsequent measurements made on the basis of model plenum pressure. The resulting momentum coefficient, and the internal balance pressure tares associated with it, were then obtained in the manner outlined in Section 2.

The data acquisition process was fully automatic and utilized a Lockheed Electronics MAC-16 digital computer. The acquisition and reduction of the data is further described in Section 3.5.

3.2 The NASA/AAMRDL 7 x 10-Foot Wind Tunnel

The NASA/AAMRDL 7 x 10-foot wind tunnel is located in the NASA-Ames Research Center complex at Moffett Field, California. This tunnel is a single-return type with the settling chamber vented to atmosphere. The contraction ratio of 14 and the test section design result in an undetectable difference between contraction pressure drop and measured dynamic pressure at the model location for the speed range employed in the subject test. The balance, air bridge, and air supply pipe used in the small-tunnel test were retained for the test in the AAMRDL tunnel. The air supply pipe was fastened to an articulated sting as shown in Figure 1.4. The sting drive mechanism provides infinitely variable pitch and yaw capability within an approximately 40-degree cone. High-pressure air for the knee-blown flap was piped through the sting to the model air supply pipe.

The model plenum pressure was controlled from the test section by exercising direct control over the dome pressure of a large pressure regulator located in the air supply line.

The seven-probe wake rake of five-holed probes was mounted on a remotely controlled traverse mechanism which can position the rake virtually anywhere in the test section, barring mechanical interference with the model or support system.

Model plenum and air supply pipe pressures were monitored using ± 50 psid Statham pressure transducers. Wake rake pressures were measured using six 48-port type D scanivalves fitted with Statham ± 2.5 psid pressure transducers.

Test section dynamic pressure was calibrated prior to model entry using a precision pitot tube and two ± 0.3 psid Statham pressure transducers supplied by Lockheed. These transducers were also used to monitor and record the tunnel contraction pressures during the test.

A twelve-channel data system was used to automatically record balance output, model internal pressures, tunnel conditions, and wake rake scanivalve information. Angle-of-attack and wake rake position data were input manually. All of the data were displayed continuously in the control room.

Preliminary, on-line reduced data were available throughout the test. The basic data were also recorded on IBM cards, providing a method for correcting and updating the data prior to final reduction.

3.3 Ground-Plane Configurations

Three ground-plane configurations are available in the test section: the normal solid floor, a moving-belt ground plane (Figure 3.2), and a tangentially-blown, boundary-layer-controlled floor (Figure 3.3). Dimensional details may be found in Figure 3.4. Configuration change is accomplished in about four hours.

The moving-ground (Figure 3.2) spans 76.2 cm (30 inches) of the 106.7 cm (42 inch) test section width and has an effective length of 96.5 cm (38 inches) between roller centers. The belt is powered by a hydraulic motor rated at approximately 20 H.P., which is adequate up to more than 30.5 m/sec (100 ft/sec). The belt speed, which is continuously variable, is monitored via the voltage output of a "Globe" DC motor, coupled to a driven roller and used as a tachogenerator. The belt speed was maintained at the free stream velocity of the test section for all moving ground tests. Calibration was made using a pulse counter and a digital voltmeter.

Tracking of the belt is currently monitored and adjusted manually. Tension adjustments are made at one end of the nondriven roller, the other end being permanently set. Principal adjustments are found to be necessary during start-up and shutdown, though some changes have to be made when model lift is increased under near-to-ground conditions. Significant increases in power are usually also required in these circumstances.

The boundary-layer-controlled ground plane (Figure 3.3) is provided with five 76.2 cm (30-inch) long blowing slots spaced at 10.16 (4-inch) intervals forward of the center of the test section. Spacers in the slots make available heights of .081, .129, and .170 cm (.032", .051", and .067"). The latter was used throughout the present tests. Each slot has a large, separate plenum, and a separate control valve. Each plenum has a static pressure tapping, which is used to measure and set slot pressure ratio. Slot velocities up to 140 m/sec (460 ft/sec) are available. There are also surface static pressure orifices and Preston tubes. Full details may be found in Reference 2.

3.4 Data Reduction in the 30" x 42" Tunnel

Data acquisition control and collection was accomplished using an 8K-storage Lockheed Electronics MAC-16 digital computer. The acquired data, in raw data counts, was temporarily stored on a Burroughs Disc, and partially displayed on the tunnel teletype. Final data reduction was accomplished on a second, 35K, MAC-16 computer that was equipped with a FORTRAN compiler and conventional library routines.

Data reduction was normally done daily although the MAC-16 Disc System would permit on-line reduction should the need arise. At the time of the reduction, the raw data was transferred to magnetic tape for permanent record.

The acquired data was obtained in three discrete routines. The first scan consisted of a sweep of all data channels which resulted in acquisition of internal balance data, pitch attitude, and auxiliary air supply temperature. The second scan was restricted to the channels of the three-ganged scanivalves, and the third scan restricted to the channel of the rake scanivalve. Tunnel conditions of total pressure, dynamic pressure, and total temperature were acquired during the initial scan, at each scanivalve porting during the second scan, and at each probe (fifth porting) during the third scan.

All acquired data was averaged over 15 samples taken at 25-millisecond intervals. All scanivalve data was acquired after an initial settling time of 500 milliseconds after each porting.

3.5 Test Section Flow Calibration and Control in the 30" x 42" Tunnel

Differing test-section speed-control procedures were followed for ground effects and for tunnel interference studies. Since no corrections were desired in the former case and comparisons were being made in the same tunnel, a conventional contraction pressure-drop type of calibration was employed, based upon a center-tunnel calibration using a 5/8-inch pitot static probe and a precision water manometer.

For center-tunnel testing, strong blockage effects were expected, and it was highly desirable to correct for these in real time, both to permit testing at "whole" C_{μ} 's and thereby avoid cross-plotting during data reduction and also because comparisons were to be made with another tunnel of larger size.

The method used is an automatic version of the wake blockage correction method devised by Hackett and Boles (ref. 4). A full explanation of the setup and calibration of the system may be found in the Appendix. Contraction upstream and downstream pressures are sensed using pressure transducers vented to atmosphere. This is equivalent to a downstream working section reference pressure since it is here that the tunnel is vented to atmosphere.

A voltage divider network (Figure 3.5) is arranged so that the mean of the model-induced static pressure change between the ends of the working section is "seen" by the system as the reference static pressure, which defines 'q'. Suitable differencing with the contraction upstream static pressure then permits a blockage-corrected 'q' to be displayed for use in tunnel control, which is manual.

3.6 Run Schedules and Procedures

The run schedule and test parameters for the wall constraints tests are shown in Figure 3.6. The configurations and conditions shown were the same for both the small and large-tunnel tests except that the tail incidence was 20 degrees in the large tunnel and zero degrees in the small tunnel.

Both test sections were calibrated prior to the respective tests using a precision pitot tube and pressure transducers supplied by Lockheed. Tunnel conditions and model plenum pressure were closely monitored during the tests. On-line data reduction in the large tunnel facilitated the monitoring operation by providing immediate print-out of computed momentum coefficient. The normal procedure was to repeat points in which dynamic pressure or momentum coefficient fell outside specified tolerances. On-line data reduction was not available during the small-tunnel test. Limited printout of the raw data was available, however; and frequent checks of model plenum pressure were made using a small hand-held calculator. The automatic C_{μ} system employed in the small tunnel provided real time monitoring of corrected dynamic pressure. Because of the extreme lift range of tests (C_L up to 19), a moving belt ground plane moving at free-stream velocity was used during the small tunnel tests to exclude the effects of floor separation on the results.

The basic procedure for the center tunnel tests was as follows:

1. Perform force tests of various model configurations in the small tunnel using the "corrected q" technique described in Section 3.5.

2. Carry out flow surveys in the small tunnel near the tail location to determine wing wake location and tail environment characteristics.
3. Perform flow visualization experiments in the small tunnel to aid in determining wing and tail stall conditions.
4. Duplicate 1, 2, and 3 above in the large tunnel making no corrections (assuming the data to be recorded under "free air" conditions).
5. Compare fully corrected small tunnel data with the uncorrected large-tunnel data. The results of this comparison are fully discussed in Sections 4 and 5.

Figure 3.7 gives the run schedule and test parameters for the ground effects tests. The ground effects tests were not run at corrected dynamic pressure. It was felt that this was not necessary because the tests were intended for a "one-on-one" comparison within the single facility. In addition, the 'q' correction method is new and, for the present, is unique to the Lockheed 30 x 42-Inch Wind Tunnel. Use of the correction method here would make comparison with other facilities, not so equipped, difficult.

The velocity of the moving ground was controlled by manually adjusting the flow of fluid to the hydraulic motor powering the downstream pulley. Speed was monitored by visual observation of the voltage output of a DC Globe motor attached to the shaft of the upstream pulley. The DC motor was previously calibrated in volts/RPM. Belt speed was then calculated using the DC motor output (RPM) and the measured diameter of the pulley.

The floor blowing rates were calibrated, set, and monitored using a 76 cm (30-inch) water manometer attached to the floor blowing plenum. The flow distribution from the floor blowing slot was surveyed using a hand-held total pressure tube. Flow distribution was determined to be constant except for small regions (approximately 0.635 cm ~ .25 inches wide) immediately downstream of the slot spacers.

During both ground effects testing and center tunnel testing in the small tunnel, the wake rake position was adjusted manually. The initial spanwise, streamwise, and height positions were set with the tunnel off. The rake was then adjusted in height by pulling the rake shaft through a hole in the top of the test section. Exact height change was determined by measuring the change in length of the exposed shaft. Correct alignment was established by virtue of machined flanges and holes in the tunnel roof fittings.

The general test procedure for the ground effects testing was as follows:

1. Determine model performance at 1 and 2 wing chord heights above the moving ground. These tests included balance data, tail environment tests and flow visualization for the various model configurations.

2. Using the boundary layer control floor, determine the blowing rates (as a function of model lift and height) that provide good agreement between moving ground lift and corresponding blown ground results for the baseline configurations.
3. Carry out routine tests using the floor blowing parameters determined in 2 above.
4. Compare routine moving belt results with routine blown floor results for various configurations. The results of these comparisons are discussed in Sections 6 and 7.

4. WIND TUNNEL INTERFERENCE STUDY: INTRODUCTION

4.1 The General Nature of the Flow

Fixed-ground, floor-tuft studies provided the tunnel flow breakdown boundary shown in Figure 4.1 with the basic model at center tunnel. The breakdown occurred earlier than indicated by South's (ref. 6) or by Turner's (ref. 7) criteria, probably because of the high jet injection angles. (It passed through the vertical at a little more than 20-degree incidence.) In order to provide better test conditions, the moving belt ground plane was run routinely at nominal tunnel speed for all except the lowest blowing momentum coefficients.

Figure 4.2 shows the basic moving- versus fixed-ground lift performance. It is clear that significant errors occur at the highest lift coefficients with the fixed ground. However, C_L 's up to ten are of greater practical interest and flow field measurements (see below) have been restricted accordingly. The ten-plus range of C_L is mainly of interest in conjunction with three-dimensionally-limited lift, but does provide a useful check on the extent of the applicability of the present tunnel correction methods.

Even if impingement problems are minimal, there is always the possibility that the near-wake structure may be modified by the strong interference present in small-tunnel high-lift tests. Though Hackett and Evans (ref. 8) have demonstrated the effect theoretically for unpowered cases, little can be found in the literature concerning tunnel-induced distortion of powered wakes like the present one. Accordingly, a careful study was made to try to detect this, in comparisons between "small" (30" x 42") and "large" (7' x 10') tunnel tests under closely controlled conditions using the same model and the same rake of five-hole probes.

Figure 4.3 is a "tuft grid" vector diagram of the flow velocities just aft of the tail position for the configuration with tips. Though the traverse plane is 3.88 chords aft of the wing quarter-chord, the tip vortex has moved inward and the flap vortex has moved downward by a considerable distance. It is also noted that the cross flow vector velocity exceeds the mainstream velocity in several places. This was even more pronounced with tips absent. With the flow at more than 40 degrees from the probe axis (which was horizontal), the calibration range is exceeded and reliable readings are not possible. "Holes" appear in the data surrounding the vortex centers, and cross-flow vectors cannot be used to find accurate vortex centers in the manner of Figure 4.3.

After a fairly exhaustive investigation, the technique illustrated in Figure 4.4 was found the best for finding vortex centers. This particular plot is used to find the spanwise position. The method relies upon the fact that there is no change in upwash angle along a vertical line passing through a vortex center. As successive plots are made moving outboard, first negative peaks (downwash) are found and then the profile "flips through" the positive,

upwash side. The vortex center is defined to be at the span position for "flip through." An estimated accuracy of $\pm 2\%$ of powered semispan was obtained.

It is evident that an estimate of the vortex center altitude may also be made from Figure 4.4, by locating the positions for peak upwash and downwash. However, such estimates usually depend upon data several inches from the vortex and have been found less reliable. Plots of sidewash angle against span position, for various altitudes, were made; and the vortex altitudes were found by detecting "flip through" in a very similar manner. A further advantage of the above method is that it permits the direction of the vortex axis to be estimated. In Figure 4.4, for example, it may be seen that the vortex axis is inclined downwards by about ten degrees. (This is the approximately constant downwash value at the 0.85 station.)

Figure 4.5 represents the output of some twenty upwash diagrams like Figure 4.4 and twenty sidewash diagrams. Figure 4.6 is the corresponding tabulated data. For the basic configuration (with or without tail), any differences between large and small tunnels are within the bounds of experimental error at C_{μ} 's of 0.4 and 1.0. However, at C_{μ} of 3 the vortex has penetrated 5% of powered span deeper into the larger tunnel, i.e. 10% of absolute distance. The possible implications of this will be discussed below. With wing tips fitted, both tip and flap-end vortices were consistently about 3% of powered semispan inboard for the smaller tunnel; the reason for this is not known. There is again a slight tendency for greater vertical penetration in the larger tunnel, but unfortunately the traverses in the small tunnel did not extend sufficiently far to pick up the flap-end vortex.

At the highest C_{μ} for which traverses were made ($C_{\mu} = 3$, $\alpha = 0$), the interference-induced vortex movement in the small tunnel was about 0.05 times the powered semispan. This subtends an angle of about 1.8 degrees at the wing quarter chord. Expressing this crudely, we may say that the wake has responded to an apparent upwash angle of 1.8° . In correcting the results via Maskell's method (see later), a tunnel-induced upwash angle of 2.3° is indicated at the wing quarter chord, a value which increases going aft. Evidently, the wake in the small tunnel has failed to respond completely to the tunnel-induced upwash. In the tunnel-corrected, rotated coordinate system, the wake penetration into the mainstream is therefore too great by a small amount. This is evidently due to the "stiffness" of the powered sheet failing to respond to tunnel-induced upwash. Fortunately, the changes involved are too small to affect the wing basic performance significantly. However, further analyses will be made concerning the tailplane.

4.2 Flow Near the Tailplane Position

Though the tailplane section was chosen for a high stalling angle at the test Reynolds number, it turned out in practice that a single setting angle was insufficient to provide unstalled operation throughout the range of test conditions. An inverted slat should have been fitted. Figure 4.7, which was prepared from tuft observations on the tail upper and lower surfaces, shows the

positive stall to negative-stall domains for tail setting angles of 0° and 20° nose up (inverted section). The latter is preferable for center-tunnel testing since the range "B" (Figure 4.7) is better placed than range "A." A review of total pressures at $x/c=3.88$ and mid-semispan showed that the altitude of the center of the wing wake was at $2z/b=-0.25$, -0.45 , and -0.65 at C_{μ} values of 0.4, 1.0, and 3.0, respectively. At zero incidence, the viscous wing wake did not interfere with the tailplane under these conditions. It was also noted that the total pressure profiles near the tail altitude at its mid-semispan ($2y/b=0.25$) were almost identical in large and small tunnels.

Figure 4.8 shows upwash distributions just aft of the tail position, at the tail altitude. Some scatter is present because adjacent points correspond to different probes. Concentrating first on tail-off conditions (nontagged points), we note fair agreement between large and small-tunnel results. No systematic upwash increase (by $\Delta\alpha$) is noted in the small tunnel. Due to an oversight, the small tunnel flow tests were made with a tail setting angle, i_H , of zero rather than intended 20° nose-up of the large tunnel test. In a tail-off flow field of -20° ($C_{\mu}=0.4$), the tail was probably very close to maximum lift, which occurs at a quoted sectional angle of 19° . The strong upwash effect (tagged open points) indicates that the tail was still performing well. This contrasts with the corresponding small-tunnel, $C_{\mu}=3.0$, case where the tail had obviously stalled and good data could not be obtained in its wake. The tagged filled symbols imply that there was less tail lift in the larger tunnel with the increased setting angle, but the tail remained unstalled at $C_{\mu}=3.0$.

Figure 4.9 shows spanwise distributions of upwash for the configuration with tips, tail off. In this case, systematic changes in upwash were present in the smaller tunnel, and there was also an inboard shift as noted in the discussion of vortex centers. A substantially increased upwash change was observed in the small tunnel, between $2y/b=1.0$ and the tip. Since the tip vortex is close to this altitude, it may be inferred that the tip vortex is somewhat stronger in the smaller tunnel. This is consistent with an increase in tip load due to wall proximity effects.

The calculated small-tunnel induced upwash at the wing position was 2.0° , 2.5° , and 3.5° for the increasing C_{μ} 's shown in Figure 4.9. Up to twice these values should be expected at the tail position. At the inboard positions the differences between the two tunnels fall approximately within the expected ranges. These differences diminished outboard due to the influence of the stronger tip vortex in the smaller tunnel.

The downwash at the tailplane position was changed very little by the addition of wing tips.

4.3 Wing Aerodynamics

At very high blowing levels, maximum lift is limited not only by viscous separation but also by the potential flow phenomenon of "limit lift" in three dimensions. At very high lift coefficients the trailing vortex sheet is swept downward sufficiently for it to induce a significant forward velocity at the wing, as well as the downwash usually considered. This reduces the apparent forward speed at the wing and consequently less lift can be generated from a given circulation. Maximum attainable lift coefficient is quoted by various authors at values ranging from 0.9 to 1.9 times aspect ratio, depending upon theoretical assumptions. Braden and Barnett (ref. 9) have analyzed some of the present data, using an advanced limit lift analysis for powered flows and quote the results shown in Figure 4.10. There is quite close correspondence between experimental lift maxima and the predicted limit lift envelope. The fact that the experimental performance improves in relation to predictions at higher blowing momentum coefficients is most likely due to augmentation caused by entrainment into the powered flow over the flap. This was demonstrated by Hackett and Lyman (ref. 10).

The significance in achieving limit lift lies in the fact that, if the tunnel corrections work under these conditions, no more severe test for them can be found.

Careful tuft studies were made in an attempt to detect any differences in the conditions for stall, or in its nature, in the large and small tunnels. Figure 4.11 sketches typical separation patterns for the basic and tipped configurations, with slats. The basic configuration is characterized by an aft root stall which propagates outwards. With tips, a forward stall starts just inboard of the flap end and propagates in both directions. In both cases a region just ahead of the flap knee stays strongly attached long after the remainder of the wing is fully separated. This is evidently due to entrainment into the knee-blowing jet and is particularly notable at very high C_{μ} 's.

Figure 4.12(a) shows conditions for the start of wing flow separation and for fully separated wing flow for the basic configuration in the two wind tunnels. At C_{μ} 's of 0.4 and above, the flap never separated in the sense that wool tufts were disturbed. However, it was noted that the mixing layer thickened considerably as the wing flow separated. This is probably related to the tendency for entrainment into the knee jet to suppress separation just ahead of it. At low C_{μ} , separation tended to start sooner in the smaller tunnel but between C_{μ} 's of 1 and 2 this trend reversed. Full separation generally occurred earlier in the smaller tunnel. Figure 4.12(b) shows large-tunnel separation loci for the configuration with tips.

5. WIND TUNNEL INTERFERENCE STUDIES: "PRODUCTION" RUNS

5.1 Wind Tunnel Correction Equations

Hackett and Boles (ref. 4) quote the following equations which include both image constraint and blockage effects.

$$\Delta\alpha = \frac{\delta}{1 + 2 C_{\mu}/\pi AR} \left(\frac{S}{C_1}\right) C_L \quad (5.1)$$

$$\Delta C_L = - C_L \frac{1}{2} \Delta C_{p_2} - C_D \Delta\alpha \quad (5.2)$$

$$\Delta C_D = - C_D \frac{1}{2} \Delta C_{p_2} + C_L \Delta\alpha \quad (5.3)$$

$$\Delta C_{\mu} = - C_{\mu} \frac{1}{2} \Delta C_{p_2} \quad (5.4)$$

where δ is the conventional incidence correction factor commonly applied without the denominator in Equation (5.1). S/C_1 is the ratio of model reference area to tunnel cross-sectional area. The denominator term in (5.1) is suggested by Williams and Butler (ref. 11) and provides correction for tunnel-induced increases in jet-sheet curvature. Though Reference 11 also suggests related corrections to C_{μ} , these make linear assumptions about angles which are violated in the present experiments and unreasonable corrections are obtained.

The $C_D \Delta\alpha$ term in Equation (5.2) is frequently discarded. However, both C_D and $\Delta\alpha$ can be large in the present experiments and their product cannot be ignored.

ΔC_{p_2} is the model-induced change in the difference between static pressures far upstream and far downstream of the model. Since the present experiments were run at "corrected q " (see Section 3), the ΔC_{p_2} terms are already incorporated in the test results as run. Equations (5.2) to (5.4) then reduce to

$$\Delta C_L = - C_D \Delta\alpha \quad (5.5)$$

$$\Delta C_D = + C_L \Delta\alpha \quad (5.6)$$

$$\text{and } \Delta C_{\mu} = 0 \quad (5.7)$$

A conventional streamline curvature correction [see Pope (ref. 12)] was applied to pitching moments in tail-on cases.

In order to assess the relative importance of the wind tunnel blockage and the image constraint corrections and also perform a definitive check on the "automatic q" system, several runs were made with the system off and Equations (5.2) to (5.4) were applied. Figure 5.1 shows both the corrections and a comparison with other results taken with the automatic system in operation. In producing the former curve (diamonds) it was necessary to cross plot to obtain "whole" C_{μ} values. This is what makes on-line correction so valuable. There is good agreement between the two methods (circles versus squares), though the stall appears somewhat earlier on one run with the automatic system working.

The breakdown of corrections shows very large C_L reductions when the blockage correction is applied (triangles versus diamonds). Image corrections, also, are by no means negligible. The results shown also indicate that the repeatability between runs is quite good in the small wind tunnel.

5.2 General Comments

To place between-tunnel comparisons in proper perspective, some brief comments will be made about overall model performance in various configurations, based on large-tunnel results. Throughout, it should be borne in mind that the C_L range up to ten is of greater practical interest than beyond ten.

Lift curve slopes for the basic and the tips-off configuration have the expected values for the respective aspect ratios at the lower blowing rates, but decline significantly at high C_{μ} : a limit-lift effect. At low angles of attack removal of inboard slats has little effect on lift, but drops the angle for $C_{L_{max}}$ from about 25° ($C_{\mu} \geq 1$) to 10° . However, the subsequent decline is less precipitous at C_{μ} 's greater than two. In the large tunnel, drag is little affected by slat removal.

Though the addition of tips adds only about two to C_L at zero angle of attack (same reference area), there is a marked improvement in lift curve slope, and there are significant gains in $C_{L_{max}}$ in the ten- C_L range. There is a tendency for somewhat earlier stall than for the basic configuration here. Though total drag levels are high, a line for L/D of five passes through the middle of the polar data in most tipped cases.

5.3 Test Results for Basic Configurations (A1 and F)

Figure 5.2(a) shows excellent agreement in lift measurements between large and small wind tunnels over almost all of the test range. There are slight differences at $C_{\mu} = 0.2$, where flap BLC may be marginal, and a significant change at $C_{\mu} = 1.0$, where the stall is much earlier in the smaller tunnel. This phenomenon, which also occurs to a lessening degree at C_{μ} 's of 8 and 6, will be discussed further in Section 5.6. Though impingement was noted in the small tunnel (Figure 4.1) in the two-to-three C_{μ} range, this is not reflected in the lift data. Small-tunnel drag data, Figure 5.2(b), agrees

well with the large tunnel, the exceptions reflect the C_L deviations already noted. Pitching moment data [Figure 5.2(c)] shows a general pitch-down tendency in the smaller tunnel at high C_{μ} 's. A likely explanation is reduced downwash over the aft fuselage in the small tunnel. There is also a stronger pitch-up associated with the earlier stall in the smaller tunnel.

Overall, there is remarkable agreement between tunnels for configuration A1, particularly in the C_L range up to 10.

Configuration F corresponds to the basic A1 configuration with the slat removed. Figure 5.3(a) again shows excellent lift agreement up to a C_{μ} of 4 ($C_L = 10$), but systematic "humpiness" in the $C_L - \alpha$ curves thereafter. A glance at the drag data [Figure 5.3(b)] shows that striking changes have occurred with the model in the small tunnel. The drag curves have been moved bodily to the left (more thrust) by about $0.6 C_{\mu}$ in the higher ranges. Though direct evidence is sparse, it is believed that small tunnel effects, with the slat absent and a wing leading edge separation, cause severe thickening of the powered flow over the flap, though without fully separating it in the conventional sense. This could explain the fact that there was no lift loss since, at the higher angle of attack the direct thrust resultant would swing from slightly forward of the vertical to aft of it. A vector change of up to 30 degrees to the rear is implied by the increase in forward thrust. Once again, pitching moments agree reasonably well between the two tunnels, [Figure 5.3(c)] up to a C_L of about 10. Beyond this, pitch down in the small tunnel coincides with the above drag effects.

The reasons for the dramatic drag changes, clearly associated with leading edge separation, which affect small tunnel but not large tunnel performance, can only be speculated upon. More rapid jet turning in the small tunnel necessitates a lower pressure above the jet just aft of the wing and it is possible that this affects the flap separation either directly or via modification to the wing separation bubble. It is also possible that unsteadiness, either model or moving-ground induced, may have altered the structure of the separation bubble. Calculations show that steady, blockage-induced changes in bubble pressure are unlikely to have been a significant factor. Again, there is a chance that differing test techniques in the two tunnels may have played a part, but this is thought unlikely. Since lift is maintained, it appears unlikely that the differences are related to 'q' changes due to blockage or the associated corrections. Further tests in the small tunnel appear desirable to trace possible reasons for the strong sensitivity to flow separation.

Except for the worsening drag correlation beyond $C_L = 4$, there is good agreement between tunnels for configuration F up to $C_L = 10$.

5.4 Configurations with Tips (B, G, and E)

In order to facilitate comparisons with the basic configurations, the same reference area is used in this section as in the previous ones. Since the basic reference dimensions are 50.8 x 10.16 cm (20" x 4") and the

appropriate tipped configuration dimensions are 76.2 x 12.7 cm (30" x 5"), the lift, drag, and C_{μ} values should be multiplied by 8/15 to convert them to the full reference area. We shall use the latter in the summary descriptions (Section 5.6) to provide better overall perspective.

For all slat combinations there is again very good lift correlation between tunnels at zero and low C_{μ} values [see Figures 5.4(a), 5.5(a), 5.6(a)] with a tendency for a later stall in the smaller tunnel. With full-span slats [Figure 5.4(a)] and higher C_{μ} 's lift tends to be 5% low in the smaller tunnel. Examination of the drag polar, in the mid-range C_L region (around 14) indicates a possibility of over-correction for blockage, since comparable points lie close to common radial lines. This could be caused by the too-short working section not permitting the asymptotic pressure to be reached prior to the breather, for the present large model. This would cause the automatic sensing system to over-correct the tunnel 'q' (see Section 5.7). Up to the mid-range of C_L 's, there is good agreement in stall incidence [Figure 5.4(a)]. Beyond this, stall occurs increasingly early in the small tunnel as C_{μ} increases to its maximum. The drag characteristics for C_{μ} 's of 8 and 10 [Figure 5.4(b)] display almost the same radical changes due to separated wing flow in the small tunnel as were noted for basic slats-off configuration. Once again, these are accompanied by a deterioration in the pitching moment correlation [Figure 5.4(c)]. The removal of the outboard slat (configuration C) does not change the lift comparison between tunnels very significantly [see Figure 5.4(a) and 5.5(a)] so far as the stall is concerned. There is a definite improvement in two-tunnel agreement at the highest C_{μ} 's; however, inspection of the drag polar [Figure 5.5(b)] suggests this is fortuitous since separation effects appear to have caused some direct thrust vectoring once again. The familiar pitch-down at high C_{μ} , separated flow conditions is again evident [Figure 5.5(c)]. Nevertheless the correlation of all components is fairly good for all except the highest C_{μ} 's.

Finally, we turn to configuration E, which has outboard slats replaced, and inboard slats removed. After reasonable low C_{μ} comparisons, the expected separation effects again dominate, lift is somewhat low and exhibits some scatter [Figure 5.6(a)] while still correlating tolerably well. However, large drag shifts [Figure 5.6(b)] again suggest thrust revectoring when flow ahead of the flap knee is separated. Pitch down again occurs after good correlations up to $C_L = 12$ [Figure 5.6(c)].

5.5 Tailplane Effects

Tail-on force runs were made in both tunnels. However, the small-tunnel runs were inadvertently made at zero-degrees tail setting angle, rather than the recommended 20 degrees used at AAMRDL. Since this makes two-tunnel comparisons difficult, only the fully slatted configurations (A1, A2, B and C) will be discussed.

In the pitching moment plots of Figure 5.7, it is evident that there is generally good agreement between wind tunnels for the basic model tail-off, with some pitch-down deviations at high C_{μ} . Figure 4.8 suggest some reduction

of downwash in the smaller tunnel at $C_{\mu} = 3$, and it is plausible that this re-shaping of the flow becomes increasingly noticeable at high C_{μ} . However, in the medium C_L range of interest tail-off pitching moments agree well.

A review of flow angle data (Figure 4.8) shows that the tail set at 20 degrees is probably fairly well aligned with the local flow at low C_{μ} in the large tunnel and is driven towards negative stall with increasing angle of attack. This is confirmed by the results of tuft studies (Figure 4.7). At low angle of attack and low C_{μ} the tail should be unstalled in both tunnels and differences should then reflect a 20-degree difference in incidence. Since the tail volume ratio is unity and the sectional $C_{L_{max}}$ is quoted as 1.6 at 20-degree angle of attack, a pitching moment increment somewhat less than this should be expected, and this is the case.

As C_{μ} is increased, tail-on pitching moment differences continue to reflect tail-off trends. However, at $C_{\mu} = 2$, the tail is evidently fairly well within its working range in both tunnels, and very good agreement in the trends is evident when allowance is made for the differing setting angles. As C_{μ} is increased further, tail stall occurs in the smaller tunnel (i.e. lower surface separated) and comparisons are no longer meaningful.

When the tailplane was unstalled, the present results show a general consistency between tunnels for the basic configuration, and a good reproduction of large-tunnel trends is obtained in the small tunnel.

Figure 5.8, for the configuration with tips, shows most of the features discussed above. Two others are also apparent. Firstly, the generally lower force trends, seen at higher C_{μ} 's, appear again in the pitching moment data. Secondly, the effects of premature small tunnel wing stall also become evident at high C_{μ} .

Subject to the above comments, we see that trends are reproduced quite well in the smaller tunnel for the tipped configuration. The overall force and moment reduction in the small tunnel is the main shortcoming. This will be discussed in Section 5.7.

5.6 Review of Force and Moment Results in Two Tunnels

We see from the previous results, summarized in Figures 5.9 and 5.10 that, for both basic and tipped configurations with or without slats, there are no serious differences between the corrected small tunnel results and large tunnel results unpowered or with power applied in approximately BLC quantities.

The above remains true in the normally accepted STOL C_L range with two qualifications. Firstly, there is a tendency for forces and moments to be too low in the small tunnel under mildly stalled conditions (basic model) and under most conditions for the model with tips fitted. This appears to be a q-correction problem. The second effect is more serious. At C_L 's greater than 5 (on gross tipped area) or 9 (for the basic wing), there is evidently a radical change in the basic flow when the wing stalls, either at high angle of

attack or due to the absence of slats. This is thought to involve a rapid thickening of the powered flap flow, and a consequent aft revectoring of the jet sheet. As a result, the drag drops by about 60% of C_{μ} and lift data exhibit increased scatter, though without any overall reduction. Possible reasons for the q -reduction and for the stall-induced revectoring phenomena will be discussed below.

Though the very high C_L -range is of little practical interest, it confirms the above trends by virtue of their amplification as power and C_L levels increase. The same general comments apply to lift and moment while drag correlation remains reasonable except under stalled conditions. However, when stall is present, the small tunnel flow is evidently changed so radically that the small tunnel results should be considered worthless.

5.7 Discussion of Wind Tunnel Blockage Corrections

The above results show that the boundaries for using wake blockage corrections while ignoring solid/bubble blockage have been defined rather sharply in the present tests, thus achieving a major objective. It remains to discuss the flow mechanisms which lead to over-correcting ' q ' and to the stall-induced revectoring phenomenon.

Figure 5.11(a) sketches a static pressure distribution along a wind tunnel wall which might be induced by a model exhibiting wholly viscous drag. Due to the positive wake thickness the flow speeds up on passing the model and the static pressure drops. Eventually an asymptotic value is reached far downstream. This is the value desired for blockage estimation. In practice, the working section is truncated at upstream and downstream ends and a lower value of ΔC_{p_2} will be returned by the data system, leading to an under-correction for blockage. The monotonic pressure signature [5.11(a)] is approximated by a clean, unstalled model which has low structural volume, such as the present one prior to stall.

Figure 5.11(b) shows a wall pressure signature more typical of a separated flow, possibly a normal flat plate (ref. 5) or a stalled wing. A bell-shaped symmetrical curve is added to the previous one, centered at a position opposite to the maximum bubble diameter, i.e. just aft of the model. It is clear from the figure that the measured value of ΔC_{p_2} greatly exceeds the true value and the wake blockage correction will be correspondingly high.

It appears possible that the addition of wing tips to the present model introduced a solid and wake blockage effect close to the wall in a way somewhat like that described above. Because of the short working section, the wake may not have ovalized sufficiently prior to the breather. Another possibility is that wall static pressures in the vicinity of the breathers, which comprised rather restricted vertical slots, were reduced by the close proximity of the vortex system. Since the force estimates in the smaller tunnel are a consistent percentage low, it is clear that overcorrection has not resulted in serious flow changes, though the actual C_{μ} values will be slightly higher than those quoted.

So far, we have discussed blockage aerodynamics as if after-the-event corrections were being made. The same arguments apply for the "automatic q " system used in the present test provided that total blockage is not overestimated. Some overcorrection is permissible to make up the difference between wake and total blockage. However, if solid/bubble blockage is sufficiently high, the possibility arises of "positive feedback" and consequent divergence of the system towards zero forward speed. Whether this occurs depends upon the response of the model aerodynamics to decrease in forward speed.

The possibility of the above overcorrection suggests firstly that considerable caution should be exercised in interpreting beyond-stall results and secondly that, once stall occurs, on-line ' q ' correction should be abandoned. Eventually, it is hoped that it will be possible to analyze signatures like that of Figure 5.11(b) and obtain total blockage estimates from wall pressures. This will avoid the above problems. The first steps towards this goal are being taken in a Lockheed-Georgia in-house program. The first step in this program is to lengthen the test section.

6. GROUND EFFECTS EXPERIMENTS: INTRODUCTION

6.1 Determination of Ground-Blowing Requirements

To put the present tests into perspective, we shall review briefly the pilot tests described in Reference 2. These involved wing and flap surface static pressures measured at three spanwise stations for various ground boundary layer control blowing ratios and with a moving ground. Figure 6.1(a) shows undersurface distributions for a model height, h/c , of 0.75. These reflect the presence of the strong vortex, trapped between the wing and the ground, shown in Figure 1.2. It is evident that the vortex is much larger for the fixed ground (crosses) than for the moving ground (circles). At a particular rate of ground blowing, a very good match to the moving ground result is obtained. The height and C_{μ} combination chosen for Figure 6.1(a) is one of the most extreme.

Figure 6.1(b) shows results of other, less extreme conditions and includes an illustration of the effect of slot size. The standard larger size used for the majority of previous tests was retained in the present work.

In the previous work (ref. 2), upper and lower surface pressure distributions, for the three stations shown in Figure 6.1(a), were integrated to give local lift coefficient values. Typical sectional lift curves are shown in Figure 6.2 for various levels of ground blowing defined by a parameter 'N'. This parameter, derived theoretically by Hackett *et al* (ref. 1) relates the wall jet velocity at its origin to the counter flow at the floor induced by the bound vortex and its image. Corresponding values of slot blowing momentum coefficient are shown in Figure 6.3, which represents the state-of-the-art recommendations at the outset of the present work.

To accommodate a model altitude of two chords, not tested previously, the slot position was changed from 2 to $2\frac{1}{2}$ chords ahead of the model and revised blowing curves were needed, both for this reason and because the present model had greatly reduced slot height compared with the previous tests. The use of a force balance in the present tests considerably simplified the process of finding floor blowing requirements. Figure 6.4 is an example of numerous varying BLC force measurements, used to redefine the blowing requirements curve. In this particular case, good results are possible over a fairly broad blowing range. However, in other cases, the lift overshoot more substantially before turning down. Under extreme model C_{μ} and incidence conditions, there was no lift maximum within the ground blowing range tested.

Figure 6.5 shows the previous slot blowing requirement for one chord altitude (lower curve) together with a revised curve, for the further forward slot, derived from force tests. These curves are not strictly comparable on a C_{Lh} basis, because of differences between pressure-derived and measured lift definitions. The latter are generally about 0.5 in C_L lower than the previous estimate, which would move the NASA CR curve into closer agreement with the "present results" curve at the upper end.

Since the philosophy behind the original definition of required blowing quantity (Figure 6.3) was founded upon sectional considerations at the most critical span station (usually the center), the selection of blowing quantities for the tipped configuration was not straightforward. For example, it was felt that power effects would continue to dominate the center of the wing, and these would be little affected by the addition of wing tips particularly at the most-critical, high C_{μ} conditions. Straightforward application of measured lift coefficients to the requirements curve (Figure 6.5) would therefore result in excessive ground blowing. To avoid this, it was decided to compromise and apply the same ground blowing rates, at any particular C_{μ} and α combination, as were used with no tips fitted. The use of ground plane instrumentation made it possible to check the validity of this approach.

At two chords altitude, the same general principles were applied. Since C_{Lh} typically had half its previous value, the slot was blown at unit pressure ratio at the lower model C_{μ} 's. The floor C_{μ} was below 0.2 over the entire test range.

A retrospective analysis showed that, tips off, the actual floor blowing quantities followed the "present results" curve (Figure 6.5) up to a model C_{μ} of 1.0, but then tended to drop off and follow the "NASA CR" line. At higher model C_{μ} 's, the actual floor blowing quantities fall below both of the recommended values by up to 20%.

6.2 Skin Friction at the Ground

Figure 6.6(a) shows results typical of numerous skin friction measurements recently analyzed. Since the purpose of the Preston tube/static pressure measurements is only to identify separation, the full skin friction calibration was not applied. Instead, indicated Preston tube and static pressures are plotted. On the upper plot, the total (Preston) reading always remains substantially above the static value, indicating the absence of separation. In the middle plot, the two tend towards the same value: separation is imminent. Finally, in the lowest plot the two curves cross and the separation point may be estimated.

In a deeper review of the data used to generate blowing requirements from lift considerations (e.g. Figure 6.4), the technique of Figure 6.6(a) was used to estimate test conditions under which ground separation was present with the blowing settings used in production runs. Figure 6.6(b) is the result. This shows that ground separation occurred at high incidence and high model C_{μ} conditions at both test altitudes, with or without tips fitted. The fact that the with-tips curves are close to the respective basic configuration curves confirms that the same ground blowing C_{μ} is required for both.

It is seen above that less-than-recommended floor BLC was applied at $C_{\mu} = 2$ and 3, and the lower part of the separation boundary probably could be improved by rectifying this.

6.3 Tailplane Setting Angle

In the present tests the tail is intended as a flow sensing and integrating device, and there is no emphasis on trim. The prime requirement is therefore to maintain attached flow so that if flow angle changes occur between moving and BLC ground tests, these are sensed by the tail and recorded as pitching moment changes. Care was therefore taken to maintain attached flow on the tailplane over as much as possible of the test range.

Since no slat was fitted to the tailplane, it was recognized that a compromise setting angle would be needed which would not necessarily correspond, in ground effect, to the angle selected for center tunnel tests. The very extreme flow angles found near the tail position in the latter case (e.g. Figure 4.8) clearly cannot persist as the tail approaches the ground closely. To establish the best setting angle, the tail was tufted and moving ground runs were carried out over the test ranges of model height, blowing, and incidence. Because of ground proximity, it was possible to observe only the upper surface of the tail, permitting only negative sectional stall to be detected. Tail setting angle of 0° , 10° , and 20° (nose up) were reviewed.

Figure 6.7(a) shows that the zero degrees setting angle was preferable at one chord altitude. This restricted the negative stall to the last few degrees of the model angle of attack range. Figure 6.7(b) shows this remained true at two chords altitude at low model C_μ . The above selection of tail setting angle was later confirmed by flow measurements (see below).

6.4 Flow Measurements Near the Tail Position

Because of emphasis in the present tests on pitching moment, it was decided to supplement the tail-on/tail-off experiments by three-component flow measurements, just aft of the model, with the tail removed. These were carried out with the probe mounted in a position extending from the tail-tip position inboard (see Figure 6.8) and at an altitude corresponding to the tail quarter-chord position at the model angle of attack concerned. This "tail-following" technique was carried out with the probe rake horizontal. Boundary layer rake data were also collected in a similar position (Figure 6.8) but were not found very useful.

Figure 6.9 shows downwash angles and dynamic pressures plotted as contour maps with span positions as ordinates and model angles of attack as abscissae. This form permits comparisons with pitching moment plots in the main results. As would be expected at low altitudes (upper plots), the flow angle tends to zero with angle of attack increase and angle 'seen' by the tail section is consequently beyond the negative stall. Zero tail angle of attack (moving ground) is achieved at a model angle of attack of about 8° for $C_\mu = 0.4$ and 1.0 and 5° at $C_\mu = 3$. (These angles combine angle of attack, tail incidence setting, and downwash angle.) There appears to be very little chance of positive sectional stall at one chord altitude: On the other hand, tail loads are not large.

In comparing moving and boundary layer controlled ground results, we note first a tendency for more upflow near the fuselage side (situated at the 0.088 station) in the latter case. This tendency reduces at the higher C_{μ} values. As might be anticipated, there is some correlation between tail flow angles with a blown ground and the occurrence of ground separation, denoted by crosses in Figure 6.9. This is particularly clear at $C_{\mu} = 3.0$, where there is a much more rapid decrease in downwash for the BLC ground which starts a few degrees beyond the angle of attack for floor separation (see filled circles). This would be beyond the test range at $C_{\mu} = 1.0$, but the reason for the rapid changes at $C_{\mu} = 0.4$ has not been determined.

In view of the reduced downwash above these high gradient bands, a more nose-down pitching moment should be expected for the BLC ground cases at high angles of attack.

The downwash distributions for the two-chord-altitude cases are characterized by strong spanwise increases in downwash as well as the previously mentioned fuselage effects. The former are sufficient to precipitate tip stall in the higher C_{μ} range. There is better general agreement between BLC and moving ground at two-chords altitude and the rapid gradient changes noted above were not observed.

Because of calibration difficulties, the relative dynamic pressure results are regarded as less reliable in an absolute sense. However, the comparisons between fixed and moving ground indicate quite good agreement except above the previously mentioned strong gradient areas, where dynamic pressure effects appear to be consistent with the observed downwash values.

6.5 Limit Lift in Ground Effect

We saw in Section 4.3 that circulation lift may be bounded by three-dimensional effects associated with the downsweep of the trailing vortex system. In ground effect, an analogous effect can occur, but in this case the counterflow at the wing bound vortex is induced by its image in the plane of the ground. This phenomenon is examined theoretically in some detail in Reference 1, where it is shown that $C_{\ell} c/h$ cannot exceed 2π in two dimensions or 4π for a semi-infinite vortex (which may approximate the tip region). Very significantly, this lift must be accompanied by a trapped under-wing bubble which extends forward and aft at the ground by a distance h . As lift reduces to 1.5π ($=4.71$), the two stagnation points merge and further reduction permits main-stream flow beneath the wing once again. Though the theoretical model employs a point vortex, it provides a useful insight into the inevitability of ground separation as wing lift is increased near to the ground. A moving ground should guarantee that the trapped bubble has the same dimensions as in flight, which is also the aspiration of the boundary layer controlled ground.

Figure 6.10 provides a preview of moving ground results obtained in "production" tests. The free-air result shows decreasing returns in circulation lift as C_{μ} is increased to the highest values. However, the effect is

not noticeable up to a C_{μ} of six. At $h/c = 2$, on the other hand, there are definite signs of bunching at a C_{μ} of three while at one-chord height, all three upper curves have reached a plateau in circulation lift. Limit circulation lift appears to occur at a lift coefficient of about four.

Examination of wing undersurface pressure distributions at the 0.643 station (Ref. 2, Figures 23 and 24) reveals that a mild undersurface suction starts at a model C_{μ} of 1.0 (moving ground, $h/c = 1.0$) leading to an extensive forward stagnation and an apparent vortex bubble stretching from 40% chord back to the flap at a C_{μ} of 3.0.

It is apparent from the above that, once again, limit conditions are being approached at the upper end of the test range. Under these conditions, it is the purpose of ground BLC not only to prevent separation (in the sense that the moving ground does) but also make the size of the vortex bubble trapped below the wing the same as with the moving ground. It is the purpose of the experiments described below to determine the extent to which this difficult task can be accomplished.

7. GROUND EFFECTS EXPERIMENTS: "PRODUCTION" RUNS

7.1 General Comments

In all of the near-ground experiments, the angle-of-attack range was physically reduced, compared to center-tunnel tests, and a reduced C_{μ} range was employed compatible with previous experiments (ref. 2). The range used, to $C_{\mu} = 3$, was sufficient to ensure that ground-limited circulation lift was encountered (Figure 6.10). These factors all reduced the total loads while, at the same time, buffet-induced unsteadiness reduced the accuracy of the data. The latter is liable to degrade drag accuracy, in particular, since a 0.1-degree angle-of-attack error translates to a drag coefficient error of 0.14 under typical ground testing conditions. The reduced drag range near the ground also exposes the basic balance inaccuracies: One percent of the axial force range represents approximately 0.14 in drag coefficient and the drag component of 1 percent of the normal force range equals about half this at 10-degree angle of attack. Though airbride tares are high, high-accuracy pressure measurements restrict errors in their estimation to about 0.02 in C_L . One percent of full balance range lift and pitching moment coefficients each convert to about 0.4 on the scales used for the basic model. It is evident from the center-tunnel experiments that achieved repeatability was probably noticeably better than the 1% full-scale values just quoted. However, this probably will no longer be true under buffet conditions in ground effect.

Since the prime objective of the present tests was to compare moving and BLC ground results, neither wind tunnel constraint nor blockage corrections have been applied.

7.2 Lift and Drag in Ground Effect

Figure 7.1 shows lift curves for BLC (filled points) and moving ground (open points) for the basic configuration at one chord altitude. Agreement is generally within balance accuracy limits with certain exceptions which occur after the floor Preston tubes sensed separation [Figure 6.6(b)]. At $C_{\mu} = 2$, the deviations slightly precede the quoted separation conditions.

With tips fitted to the model, Figure 7.2 shows very similar lift results to those just described. It is evident, once again, that floor separation has seriously degraded the higher C_{μ} results.

On raising the model to two-chords altitude, the proportion of the separated-floor points is less, and overall lift agreement is significantly improved for both configurations A1 (Figure 7.3) and B (Figure 7.4). At two-chords altitude, the limit-lift effect (Figure 6.10) is lessened and $dC_L/d\alpha$ increases markedly, particularly with tips fitted (Figure 7.4).

Provided post-floor separation points are ignored, there is good lift agreement between moving and blown ground results. There is no regular trend for either to yield higher lift.

As indicated in Section 7.1, experimental accuracy in drag is not particularly good. It may be seen from Figure 7.5 that, up to conditions corresponding to floor separation, the BLC ground reproduces the moving ground trends correctly for configuration A1 at $h/c=1$, but at somewhat higher drag level. Under separated floor conditions, which encompass most of the α -range for C_{μ} 's of 2 and 3, poor correlation is obtained.

As may be expected from the increased aspect ratio (and particularly in ground effect) adding tips reduces the drag quite noticeably (Figure 7.6). The discrepancies under separated-floor conditions appear once again and the general increase in drag with the blown ground is similar to before.

At two-chords altitude, incidence-dependent drag appears clearly associated with the increased lift curve slope. At the two lowest C_{μ} values, drag agreement for configuration A1 remains acceptable (Figure 7.7) but is disappointing at higher settings. The poor correlation of post-floor separation results is expected but; prior to this, there appears to be an incidence-related crossover between the moving and blown ground curves at about 12-degrees angle of attack. A similar, but less noticeable, tendency is also noted at unit chord altitude (Figure 7.5). Since it is at this angle of attack that the flap upper surface approaches the vertical, it seems possible that the changes in trend are provoked by jet air moving forward at ground level, after impingement.

The tips-on drag comparison of Figure 7.8 shows quite poor agreement between the two methods of ground treatment. This is quite surprising and not understood, since the task of controlling the floor for the two-chords altitude case should be easier than for one chord. Several comments may be made. It is evident, in both Figures 7.7 and 7.8, that there is more scatter in the moving ground results. Secondly, a comparison between the blown-ground drag results of Figures 7.7 and 7.8 and corresponding moving-ground center-tunnel results shows excellent agreement in the trends with angle of attack and slightly lower absolute values. It is not known whether the theoretical drag of this configuration is starting to asymptote the free air value at two chords altitude. The only conclusions that can be reached are that the effect is significant and takes the form of a lift-dependent drag error which tends to be independent of C_{μ} in the range from 0.7 to 2.0. This suggests a change in spanload shape, which occurs with no change in lift.

7.3 Pitching Moments Tail-off and Tail-on

We see from Figure 7.9 (basic configuration) and 7.10 (tipped configuration) that, with one exception, there is excellent pitching moment agreement between blown and moving belt results up to, and sometimes including separated ground cases. The exception concerns the curves at $C_{\mu}=0.4$ (upper left,

Figures 7.9 and 7.10). Pitch up "bumps" appear at 8° with fixed ground and with BLC for the basic configuration, yet also (at 6°) with a moving ground and the tipped configuration. There is also a smooth curve in each case — one with the ground moving, the other boundary-layer controlled. The reason for this apparently anomalous behavior is related to temporary wing separation, which in some cases was followed by a recovery and in other cases did not occur until a higher angle of attack. It is noted that the "bumps" occur near the wing $C_{L_{max}}$. At the high C_μ levels all serious differences between the two ground treatments are associated with under-blowing the BLC, and the consequent floor separation. In a number of cases, particularly for configuration A1, agreement remained fairly acceptable even including $C_\mu = 3$.

At two-chords altitude (Figures 7.11 and 7.12), almost identical comments apply, and agreement is particularly good in the with-tips cases.

7.4 Discussion

For the present series of experiments, ground blowing quantities were determined by a continuation of previous philosophy (ref. 2) but employing directly measured lift rather than undersurface pressures as a criterion. With the exception of a high angle-of-attack/high C_μ corner, these techniques were successful and the use of $C_L h/c$ as a determinant for blowing was validated.

Retrospective analysis of floor skin friction measurements showed that the region just mentioned could have been avoided by feeding-back skin friction measurements in real time. One reason this was not done lay in the recognition that, under some circumstances, floor separation may be a correct state (see Figure 1.2). However, it is now recognized that the hazards of overblowing and destroying the underwing vortex in a few cases are much less than underblowing over a much broader spectrum of cases — which appears to be the real alternative. For example, Figure 6.1(b) shows very little evidence of a trapped vortex at one-chord altitude used in the present tests. It is therefore suggested that the possibility be considered of feeding back skin friction data so as to control separation directly.

Figure 7.13 was developed by reanalyzing the varying-BLC data (e.g. Figure 6.4) as if skin friction feedback had been employed. At lower model C_μ 's, floor blowing pressures tend to be reduced, beyond floor separation they are substantially increased. Analysis of the resulting lift coefficients (lower table) is not very conclusive because much of the data available was close to wing stall, and there were no examples of BLC blowing high enough to prevent floor separation at the highest model blowing momentum coefficient.

7.5 Tests with Simulated Strut Shrouds

The earlier tests (ref. 2) included wing undersurface pressure measurements with a simulated underwing support strut shroud which cleared the wing by 0.5 cm (0.2 inches). This was set at zero degrees and then at 45 degrees to the mainstream, as indicated by floor tuft observations. Having a balance made tests on a range of strut yaw angles feasible and tests were carried out, with suitable simulated struts, with the wing at one- and two-chords altitude. Configuration C was chosen for these tests because it has tips and tailplane present and being fully slatted, it is the most representative of whole-aircraft tests.

Figures 7.14, 7.15, and 7.16 show lift, drag, and pitching moment, respectively, for $h/c=1$. Careful comparisons of all these components with the base, struts-out, runs are somewhat inconclusive regarding optimum strut yaw at low C_{μ} but clearly indicate that the 45-degree setting is best at $C_{\mu}=1$ and above. Because of the floor separation at $C_{\mu}=3$ previously mentioned, there were some difficulties in analyzing these data. In cases of doubt, particularly concerning pitching moment, a cross-check was made against moving ground data.

At two chords altitude (Figures 7.17, 7.18, and 7.19), the low and the high C_{μ} data were again somewhat inconclusive for similar reasons to before, but overall checks indicated that toe-in settings of 15° , 30° , 45° , and 45° were appropriate for low C_{μ} 's, 1, 2, and 3, respectively. In this higher altitude case, the selection rested much more upon pitching moment (the tail was on) than upon the other two components. Lift was scarcely affected by toe-in.

7.6 Summary

Using the ground blowing techniques described in Section 6 and excluding cases where floor blowing was insufficient to prevent separation (Figure 6.6), good agreement was obtained with lift and pitching moments measured with a moving ground for both tipped and basic configurations, tail-on and tail-off at one- and two-chords altitude.

Though drag measurements were subject to greater errors than lift and pitch, a definite tendency was noted for higher drags to be recorded with the blown ground. The reason for this is not known, but it is noted that the errors are lift-dependent. It appears desirable to employ improved drag instrumentation which would preferably measure true drag rather than axial force.

There is also a possibility noted from the drag measurements, that forward spillage of jet air after impingement on the ground affects blown and moving ground boundary layers differently. Under such circumstances, blown-ground drag measurements should be regarded with caution.

As was seen in Section 6, floor separation at the higher C_{μ} 's was largely attributable to under-blowing the BLC. It is anticipated that significant expansion of the useful $C_{\mu} \sim \alpha$ envelope would be possible via an appropriate revision to blowing techniques with the inclusion of feedback from floor skin friction measurements. Such feedback would enhance very considerably the generality of blown-ground application.

8. CONCLUSIONS

Large and small tunnel interference studies and ground effects experiments have been carried out on a basic wing, with a full-span, highly deflected knee-blown flap, spanning 48% of the small tunnel. Configuration variations included the addition of unflapped tips, the use of a low-mounted tailplane, and selective removal of the leading edge slats.

A moving ground, used as a datum for small tunnel ground effects studies, was also run routinely in high lift, center tunnel experiments.

8.1 Wind Tunnel Interference Studies

Matched sets of high lift tests on the above model were carried out in the Lockheed-Georgia 30' x 42' Low-Speed Wind Tunnel and in the NASA/AAMRDL 7' x 10' tunnel. Both flow and force investigations were carried out. Wake blockage corrections, based upon working section exit and entry pressures (ref. 4) were applied in real time to provide "corrected q " in the working section. Tunnel induced angle-of-attack corrections were calculated using the method given by Williams and Butler (ref. 11). The following conclusions were reached:

STOL- C_L Range (Up to 8 or 10)

1. The structure of the vortex wake is almost identical in the two tunnels at a plane near the tail position. There is slightly less downward penetration into the smaller tunnel, but the difference is consistent with the flow rotation applied when correcting for tunnel image effects. The present corrections to incidence therefore automatically accommodate the effects of the observed small changes in wake penetration.
2. For the basic configuration, there was good correlation between tunnels in corrected lift, drag and pitching moments up to $C_L = 10$ (see Figures 5.2 and 5.9).
3. With slatted tips added (see Figures 5.4 and 5.10), the large-tunnel characteristics were faithfully reproduced in the small tunnel, up to $C_L = 8$ (based on gross area). However, the forces and moments were about 5% low in the upper part of this range. This is attributed to overcorrection for blockage, caused by an insufficient settling length between the model and the working section exit.
4. With the slats removed ahead of the forward flap (Figures 5.3 and 5.6), correlations were good only up to $C_L = 5$ (either configuration). Thereafter, a violent flow change appears to have occurred in the small tunnel accompanied by gross reductions in drag, but with no significant lift changes.

It is surmised that flow thickening over the powered flap resulted in an effective vectoring of up to 30 degrees aft, even though the flow was not visibly separated (tufts).

Extra-High C_L (8 to 10, plus)

5. At low angles of attack, slats-on, the agreement between tunnels was similar to that described above. However, stall occurred increasingly early in the small tunnel at C_{μ} 's of 6, 8, and 10, resulting in the same precipitous drag changes as were observed slats-off. This was accompanied by pitch down.

6. With the slats off in the small tunnel, aft vectoring was immediate in the extra-high lift range; and there was no correlation with the large-tunnel results. Pitch-down again occurred and though there was some agreement between lift values in the two tunnels, this is regarded as superficial.

7. There are reasons to suspect that the use of the "blockage-corrected q " feedback amplified the post-stall effects via overcorrection. It is therefore recommended that ' q ' should not be corrected on-line, via the present system, when extensive separation is present ahead of a highly powered flap.

8. Some of the problems mentioned above may be attributable to the fact that solid/bubble blockage is ignored in the present wake corrections. Extensions to the present method have been demonstrated (ref. 5) which evaluate solid/bubble blockage successfully. These may offer the opportunity to extend automatic ' q ' generation into the post-stall range.

8.2 Ground Effects Experiments

The proper ground BLC slot size, position, and blowing rate had been derived in previous experiments (ref. 2) on the basis of measured airfoil undersurface pressure distributions, which were matched to datum moving ground values. Because of changes to model configuration and slot position in the present tests, a new floor blowing requirements curve was developed (Figure 6.5) based on a lift-matching procedure (Figure 6.4). The resulting curve was consistent with the previous one. It is noted that floor C_{μ} 's are fairly modest compared to those applied at the model in any particular situation. No tunnel corrections were applied.

A retrospective review of centerline ground skin friction measurements taken during "production" tests showed that, at the highest C_{μ} value tested (three) and at high incidence at $C_{\mu} = 2$, the floor flow was separated. [See Figure 6.6(b).]

Because of the obvious opportunity for ground-blowing to influence the flow near the floor behind the model, comprehensive flow surveys were made using a "tail-following" technique. Flow downwash histories (with model angle of attack) were found to be generally similar for the two types of ground

except after the BLC floor had separated. The latter caused rapid downwash reductions near the tail.

To provide a critical test, the tailplane was low-mounted. However, because it was unslatted and because of high downwash gradients (even with the floor unseparated), it proved difficult to use effectively as a flow sensor.

With the above investigations as background, the following conclusions were drawn from the "production" ground-effects tests over a model C_{μ} range of zero to 3.0:

1. In the absence of floor separation [Figure 6.6(b)], good lift correlations were obtained between BLC and moving grounds for both basic and tipped configurations at one- and two-chords altitude.

2. Drag appeared generally higher for the BLC ground. It too became uncorrelated under floor-separation conditions.

3. One-chord altitude drag measurements correlated better than for two chords. However, the moving ground data showed unexpected trends with height in the latter case.

4. At two-chords altitude and about twelve-degrees angle of attack, the blown-ground drag crossed below the moving ground data. It seems possible that a differing interaction with impinging jet air is responsible.

5. With separated-floor cases once again excepted, pitching moments correlated very well for both configurations and at both altitudes. This includes faithful reproduction, by the blown ground, of some heavily kinked pitching moment curves.

6. From the above, it is apparent that drag, rather than lift or pitching moment is more susceptible to differences in ground treatment. A more accurate drag measurement technique is required than the present axial and normal force balance.

7. The high- C_{μ} , high- α "corner" for which separation occurs can undoubtedly be reduced or eliminated by revised blowing techniques. Recent analyses of ground skin friction measurements suggest that these should be monitored routinely and used as input for the selection of ground blowing rate.

8.3 Test with Simulated Support-Strut Shrouds

The availability of a sting supported model over a boundary layer controlled ground provided an excellent opportunity to investigate strut-shroud-induced interference forces at high lift. The use of toe-in to align the strut with the local flow was of particular interest. The full tips-on, slats-on, tail-on model configuration was chosen as being most representative. Tests with typical strut shrouds (see Table I) yielded the following conclusions:

1. For model $C_{\mu} \geq 1$ the best compromise toe-in angle at unit chord altitude was 45 degrees. Below unit C_{μ} , there was no particularly good compromise.

2. Results at two-chords altitude were generally similar, but toe-in angles for minimal shroud effects were 15°, 30°, 45°, and 45° for low C_{μ} , and $C_{\mu} = 1, 2,$ and 3, respectively.

8.4 Recommendations

On the basis of the preceding work, certain questions have been raised and problem areas identified which lead to the following suggestions for investigations or improvements to test techniques:

Wind Tunnel Interference

1. A longer test section is required which will permit the separation-bubble-induced suction peak at the tunnel wall to damp out prior to the tunnel breather and diffuser entry. This will improve the accuracy of wake blockage estimation, particularly for large, bluff and stalled models.

2. The reasons for the "thrust revectoring" phenomenon, encountered in the small tunnel when there is separation ahead of the knee-blown flap, need to be investigated further. Comparisons should be made between results from "automatic q" and conventional tests under these conditions.

3. Work should be carried out to augment the current wake blockage techniques by introducing a solid blockage term (ref. 5), determined from additional wall pressure measurements.

Ground Effects

1. Follow-up tests should be carried out using the same model, but with increased ground blowing at the higher model C_{μ} 's. These should include feedback of ground skin friction information to determine blowing rate at the ground.

2. The two-chords altitude, moving-ground datum data should be checked.

3. Means for improving the accuracy of drag measurements should be investigated. Ground effects investigations will benefit.

4. The use of a pitch-yaw rake fixed in the tail position should be considered instead of the present techniques.

9. REFERENCES

1. Hackett, J. E.; and Praytor, E. B.: Ground Effect for V/STOL Aircraft Configurations and Its Simulation in the Wind Tunnel, Part I - Introduction and Theoretical Studies. NASA CR 114,495, November 1972.
2. Hackett, J. E.; Boles, R. A.; and Praytor, E. B.: Ground Effect for V/STOL Aircraft Configurations and Its Simulation in the Wind Tunnel, Part II - Experimental Studies. NASA CR 114,496, November 1972.
3. Hackett, J. E.; Praytor, E. B.; and Caldwell, E. O.: Ground Effect for V/STOL Aircraft Configurations and Its Simulation in the Wind Tunnel, Part III - Application to the NASA-Ames 40- by 80-foot Wind Tunnel. NASA CR 114,497, November 1972.
4. Hackett, J. E.; and Boles, R. A.: High Lift Testing in Closed Wind Tunnels. AIAA Paper No. 74-641, July 1974.
5. Hackett, J. E.; and Wilsden, D. J.: Determination of Low Speed Wake Blockage Corrections via Tunnel Wall Static Pressure Measurements. Presented to the AGARD Wind Tunnel Design and Testing Techniques Symposium, AGARD CPP174, October 1975.
6. South, P.: Measurements of Flow Breakdown in Rectangular Section Wind Tunnel Working Sections. National Aeronautical Establishment LR-153, 1968.
7. Turner, T. R.: A Moving Belt Ground Plane and Results for Two Jet-Flap Configurations. NASA TN D-4228, 1967.
8. Hackett, J. E.; and Evans, M. R.: Vortex Wakes Behind High Lift Wings. *Journal of Aircraft*, May 1971.
9. Braden, J. A.; Barnett, L.; Holmes, A. E.; and Carlton, M. E.: Advanced High Lift Design through Analytical/Experimental Techniques. AIAA Paper No. 75-992, August 1975.
10. Hackett, J. E.; and Lyman, V.: The Jet Flap in Three Dimensions: Theory and Experiment. AIAA Paper No. 73-653, July 1973.
11. Williams, J.; and Butler, S. F.: Experimental Methods for Testing High Lift BLC and Circulation Control Models. In *Boundary Layer and Flow Control* by Lachman (ed), Vol. I, Pergamon Press, 1961, p. 395.
12. Pope, A.: *Wind Tunnel Testing*. Wiley, 1954.

TABLE I
MODEL DIMENSIONS

Model is located at center tunnel, waterline	38.10 cm	(15.00")
Fuselage:		
length	31.55 cm	(12.42")
maximum width	4.46 cm	(1.76")
maximum height	7.76 cm	(3.06")
maximum cross section	30.30 cm ²	(4.70") ²
equivalent diameter	6.21 cm	(2.44")
fineness ratio	5.08	
balance centerline location		
water line	40.64 cm	(16.00")
butt line	0	
Wing:		
area	517.00 cm ²	(0.556 ft ²)
aspect ratio (on nominal chord)	5.00	
span	50.80 cm	(20.00")
nominal chord (constant)	10.16 cm	(4.00")
quarter chord water line	38.10 cm	(15.00")
twist, sweep	0	
Wing and Tips:		
area	968.00 cm ²	(1.042 ft ²)
aspect ratio (on nominal chord)	6.00	
span	76.20 cm	(30.00")
nominal chord	12.70 cm	(5.00")
Leading Edge Slat		
area (projected onto maximum chord)		
wing only	103.00 cm ²	(0.111 ft ²)
wing and tips	155.00 cm ²	(0.167 ft ²)
span		
wing only	50.80 cm	(20.00")
wing and tips	76.20 cm	(30.00")
chord (maximum)	2.03 cm	(0.80")
slot width	0.127 cm	(0.050")
deflection	80.00 degrees	

Trailing Edge Flap:

area (projected onto maximum chord)	234.00 cm ²	(0.252 ft ²)
span	50.80 cm	(20.00")
chord (maximum)	4.60 cm	(1.81")
slot width	0.041 cm	(0.016")
deflection (wing chord to flap upper surface)	76.00 degrees	

Tail:

area	161.00 cm ²	(0.174 ft ²)
aspect ratio	4.00	
span	25.40 cm	(10.00")
nominal chord (constant)	6.35 cm	(2.50")
quarter chord location		
station	33.34 cm	(13.13")
water line	38.10 cm	(15.00")
twist, sweep	0	

Struts (NACA 00 series):

tip chord	6.03 cm	(2.375")
tip t/c	0.189	
root chord		
short strut	7.29 cm	(2.870")
long strut	9.39 cm	(3.697")
root t/c		
short strut	0.169	
long strut	0.135	
span		
short strut	6.10 cm	(2.40")
long strut	16.26 cm	(6.40")
area		
short strut	41.00 cm ²	(0.175 ft ²)
long strut	125.00 cm ²	(0.135 ft ²)
nominal clearance beneath wing	3.18 cm	(1.25")

Quarter-Chord Location

streamwise	wing quarter chord
spanwise	75% wing semi-span

Reference Point:

axial station	wing quarter chord
water line	tunnel floor
butt line	axis of symmetry

APPENDIX

IMPLEMENTATION AND CALIBRATION OF "BLOCKAGE CORRECTED q " SCHEME

The accepted correction to the dynamic pressure due to model blockage is:

$$q_c = q_{uc} + 2\epsilon_s q_{uc} + 2\epsilon_w q_{uc} \quad (A1)$$

where q_c = corrected dynamic pressure at model station
 q_{uc} = uncorrected dynamic pressure at model station
 ϵ_s = solid blockage coefficient
 ϵ_w = wake blockage coefficient.

Reference 4 gives the blockage due to the wake in the form

$$\frac{\Delta q}{q_{uc}} = 2\epsilon_w = \frac{1}{2} \left(\frac{p_{cm} - p_{co}}{q_{uc}} \right) \quad (A2)$$

where p_{cm} = static pressure at end of contraction section with model present
 p_{co} = static pressure at end of contraction section with tunnel empty.

The tunnel conditions are obtained from static pressure tapping at the start of the contraction section (assumed to be approximately total pressure) and a static pressure tapping at the end of the contraction section (p_c). The total pressure line, as can be seen in Figure 3.5, is connected to two differential pressure transducers, one open to atmosphere to give H_c , and the other connected to the static pressure line to give ΔP .

The static pressure at the end of the contraction section will then be

$$p_c = H_c - \Delta P \quad (A3)$$

Thus,

$$\begin{aligned} q_c &= q_{uc} \left\{ 1 + 2\epsilon_s + \frac{1}{2} \frac{(H_c - \Delta P - p_{co})}{q_{uc}} \right\} \\ &= \frac{1}{2} \left\{ H_c + [2 + 4\epsilon_s - \left(\frac{p_{co}}{q_{uc}} \right)] q_{uc} - \Delta P \right\} \end{aligned}$$

$$= \frac{1}{2} \{ H_c + [(2 + 4\epsilon_s - (\frac{p_{co}}{q_{uc}})) (\frac{q_{uc}}{\Delta P}) - 1] \Delta P \}$$

$$\therefore q_c = \frac{1}{2} (H_c + K\Delta P) \quad (A4)$$

where

$$K = [2 + 4\epsilon_s - (\frac{p_{co}}{q_{uc}})] (\frac{q_{uc}}{\Delta P}) - 1 . \quad (A5)$$

(p_{co}/q_{uc}) and $(q_{uc}/\Delta P)$ are empty tunnel calibration slopes and ϵ_s is the conventional solid blockage correction.

During on-line display of q_c , the values H_c and ΔP and hence q_c are voltages; thus Equation (A4) is more conveniently considered in the form

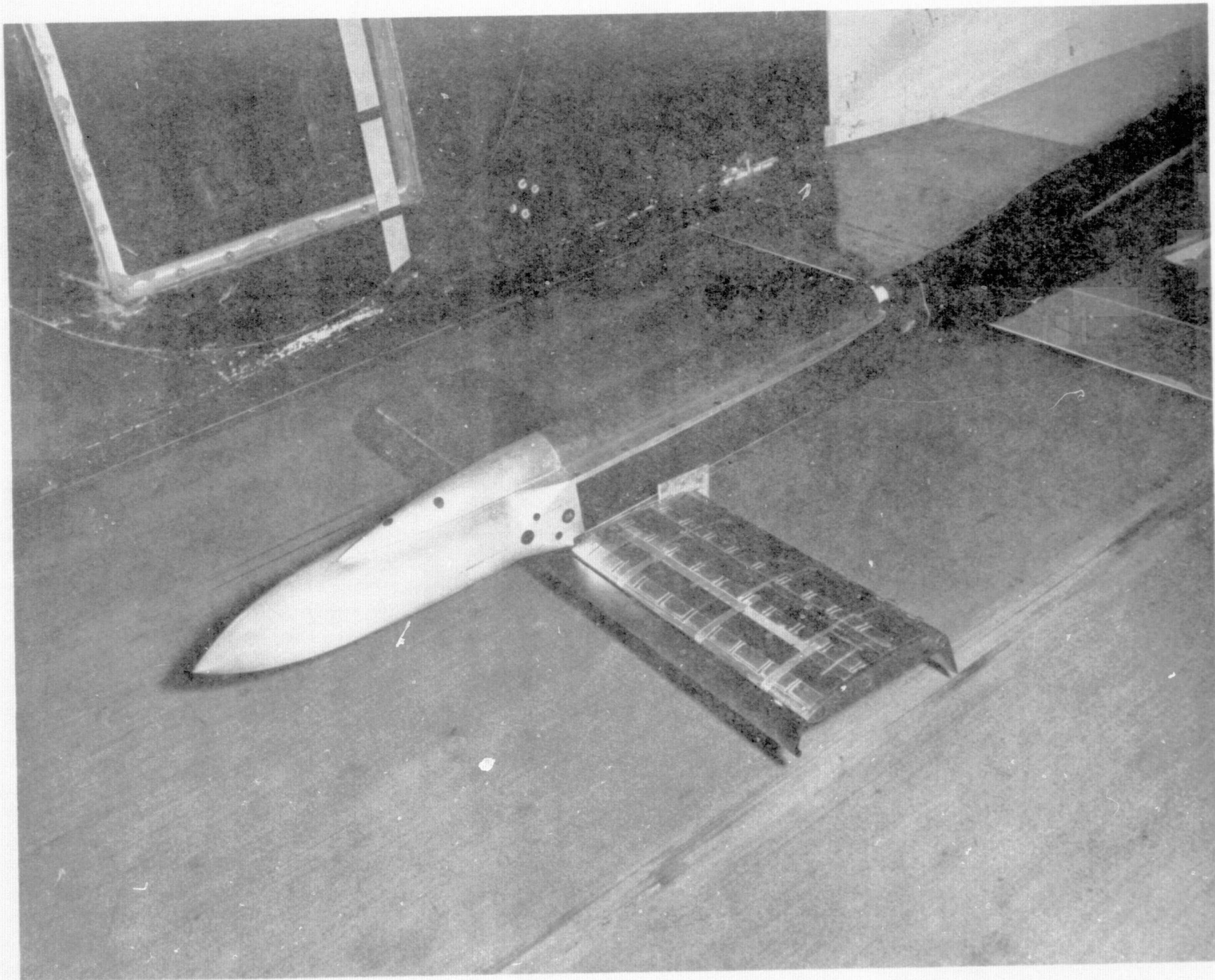
$$q_c = K_1 (\frac{1}{2} H_c + K_2 \Delta P) \quad (A6)$$

where K_1 permits the digital voltmeter (DVM) output to be corrected to "engineering" units.

The corrected 'q' potentiometers were set up by opening the static pressure line to atmosphere and applying a known pressure to the total line (hence, $H_c = \Delta P =$ applied pressure).

Initially, the ΔP circuit was disconnected (making $\Delta P = 0$) and the potentiometer, K_1 , adjusted to display half the applied pressure on the DVM. The ΔP circuit was then reconnected and the potentiometer, K_2 , adjusted to display on the DVM the value obtained by solving Equation (A4).

ORIGINAL PAGE IS
OF POOR QUALITY



41

FIGURE 1.1 MODEL TESTED UNDER CONTRACT NO. NAS2-6690

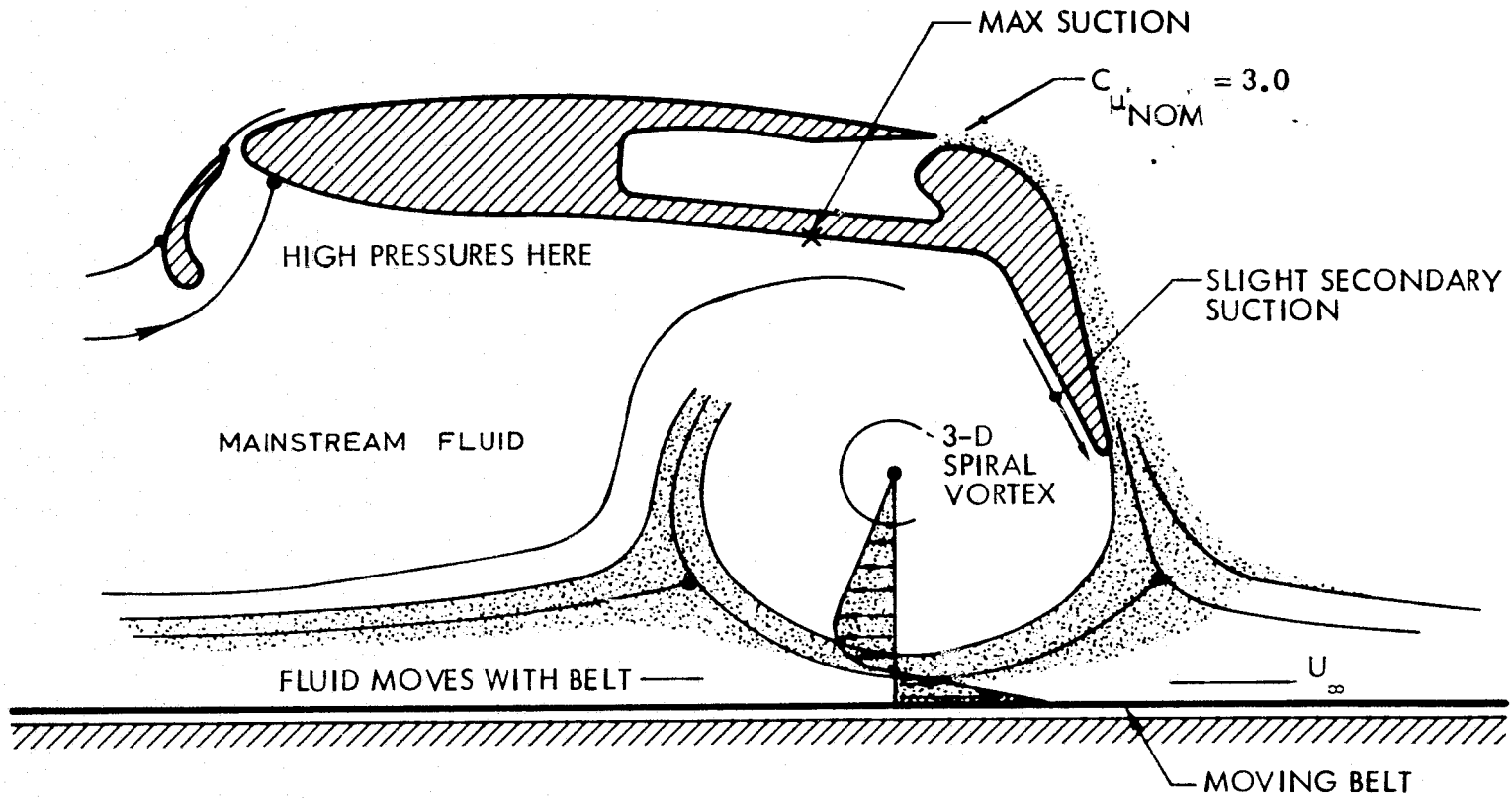
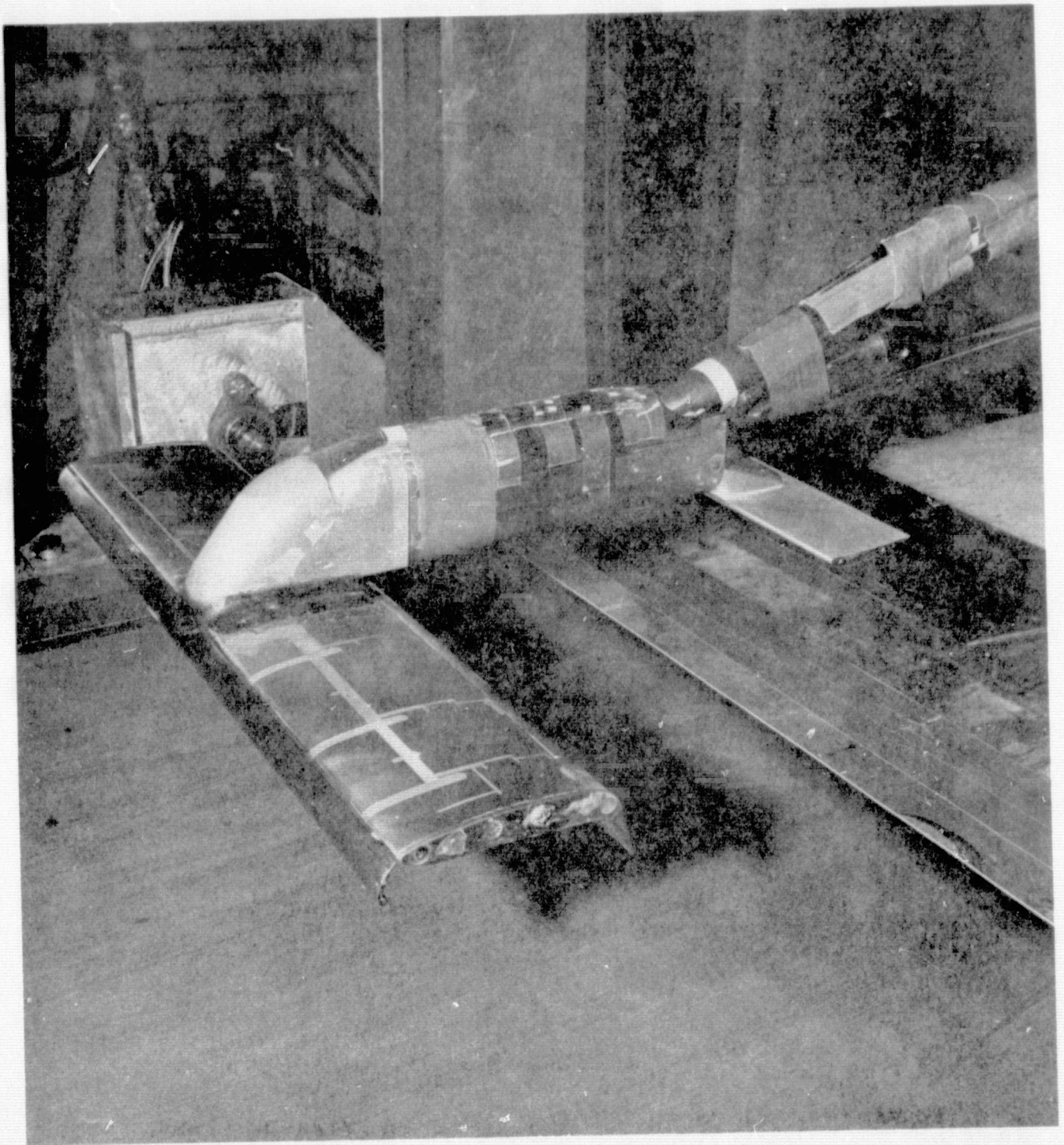


FIGURE 1.2 FORMATION OF TRAPPED, UNDERWING VORTEX AT LOW ALTITUDE AND HIGH JET MOMENTUM



ORIGINAL PAGE IS
OF POOR QUALITY

FIGURE 1.3 THE PRESENT KBF MODEL (CONFIGURATION A-2) IN THE LOCKHEED
30 x 42-INCH WIND TUNNEL (MOVING GROUND PRESENT)

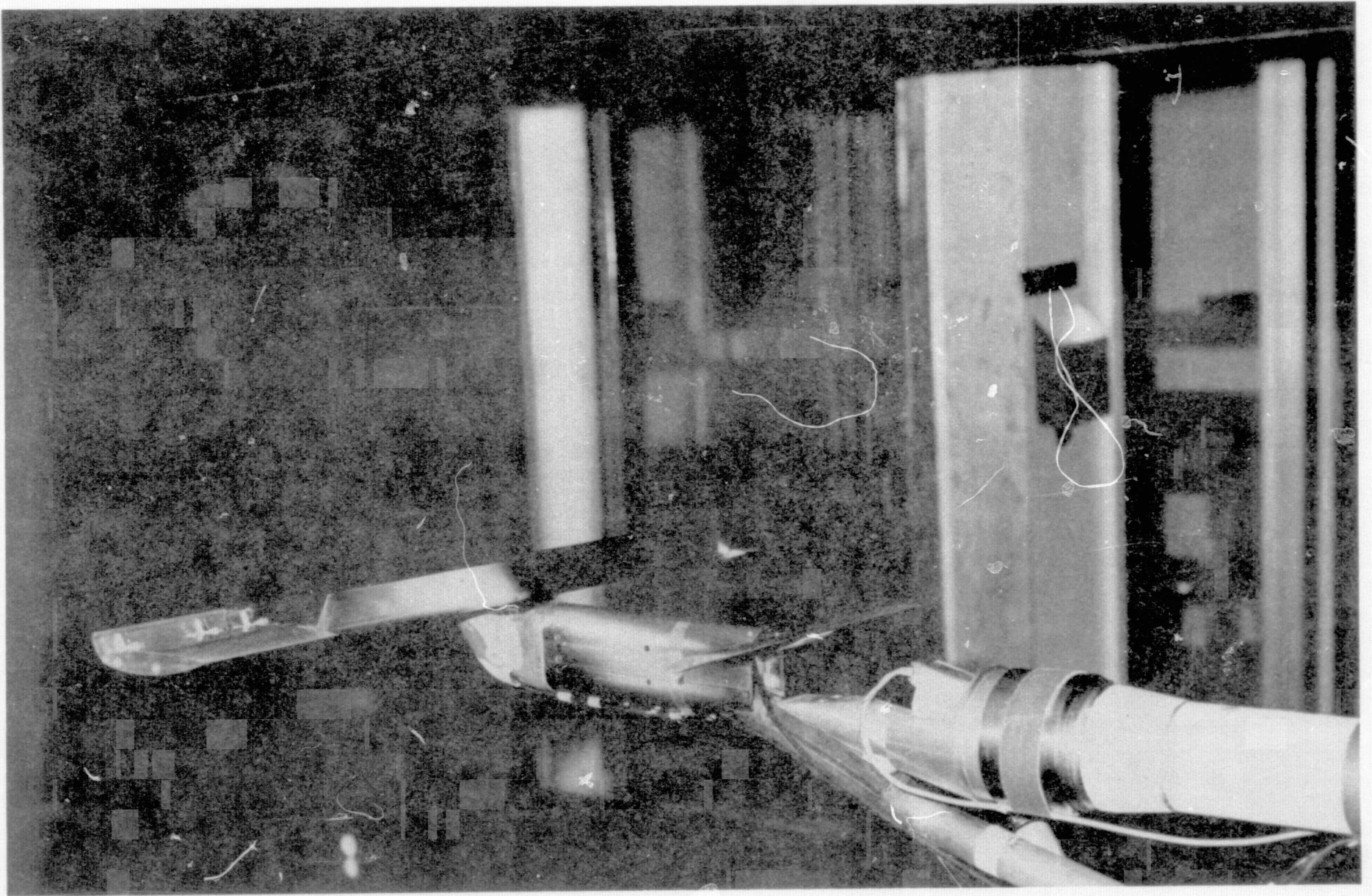


FIGURE 1.4 CONFIGURATION H IN NASA/AAMRDL 7x10 FOOT WIND TUNNEL

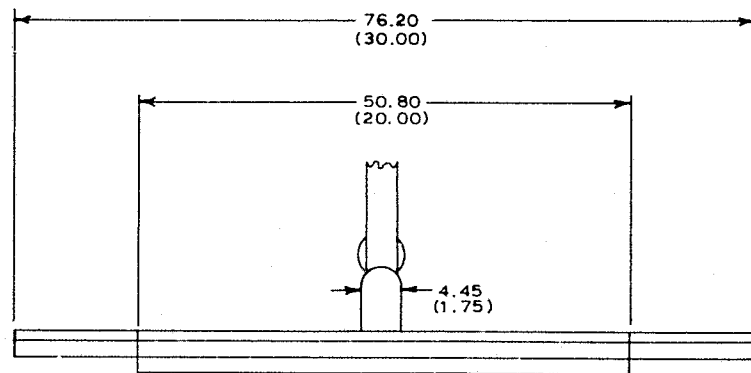
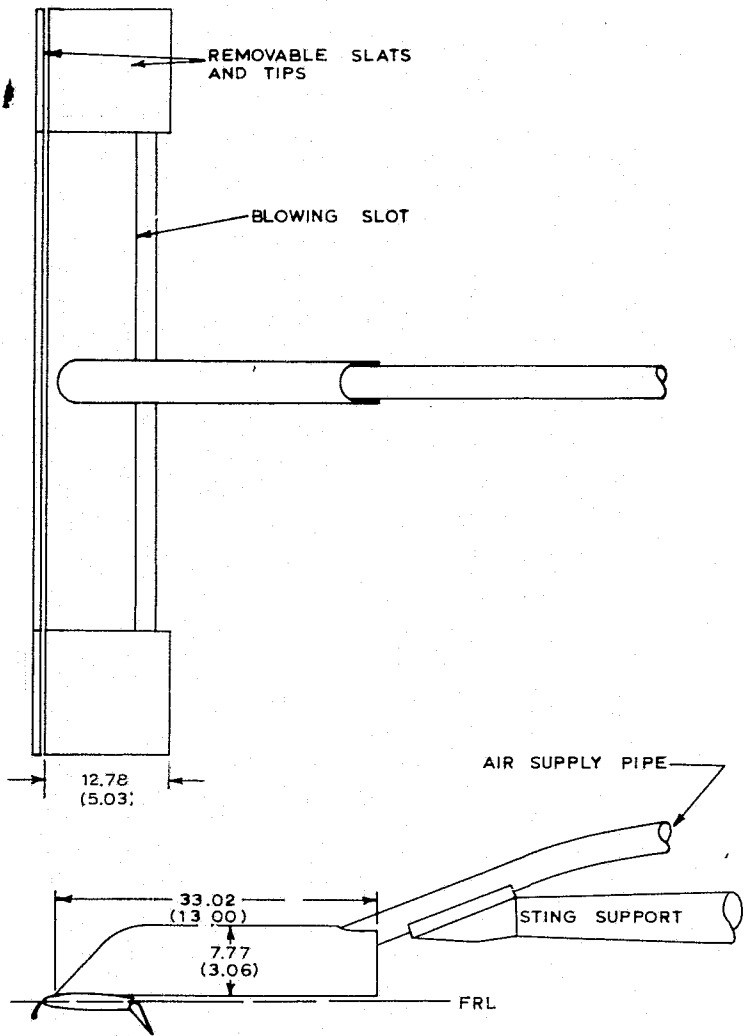
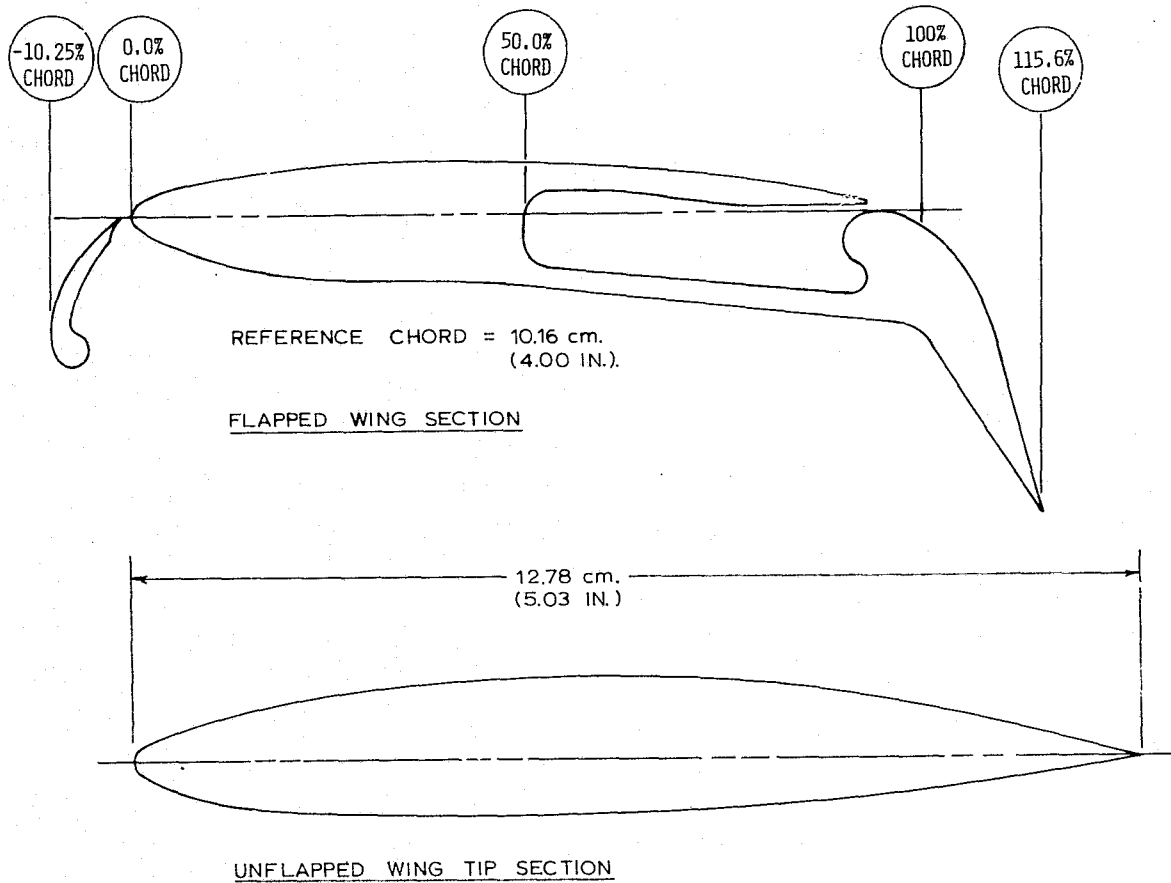


FIGURE 2.1 MODEL GENERAL ARRANGEMENT



ORDINATES OF FLAPPED WING SECTION

X/C	YU/C	YL/C
0	.000	.000
.017	-.019	-.019
.030	-.028	
.067	-.036	-.044
.103	-.045	
.147	-.053	
.250	-.062	-.076
.414	-.069	-.081
.585	-.063	-.096
.750	-.047	-.114
.913	-.020	
.930	-.011	
.965		-.138
.906	-.003	
.990	-.010	
1.015	-.021	
1.037	-.037	
1.074	-.060	
1.082		-.275
1.088	0.120	
1.111	-.211	
1.134	-.302	

ORDINATES OF UNFLAPPED WING TIP SECTION

X/C	YU/C	YL/C
0	0	0
.010	.015	-.015
.020	.020	-.020
.049	.032	-.033
.099	.045	-.045
.148	.056	-.050
.198	.064	-.053
.247	.071	-.055
.296	.077	-.056
.395	.082	-.056
.494	.083	-.053
.593	.079	-.049
.692	.069	-.042
.791	.051	-.032
.889	.028	-.019
.988	.002	-.003
1.000	0	0

FIGURE 2.2 MODEL WING SECTION ORDINATES

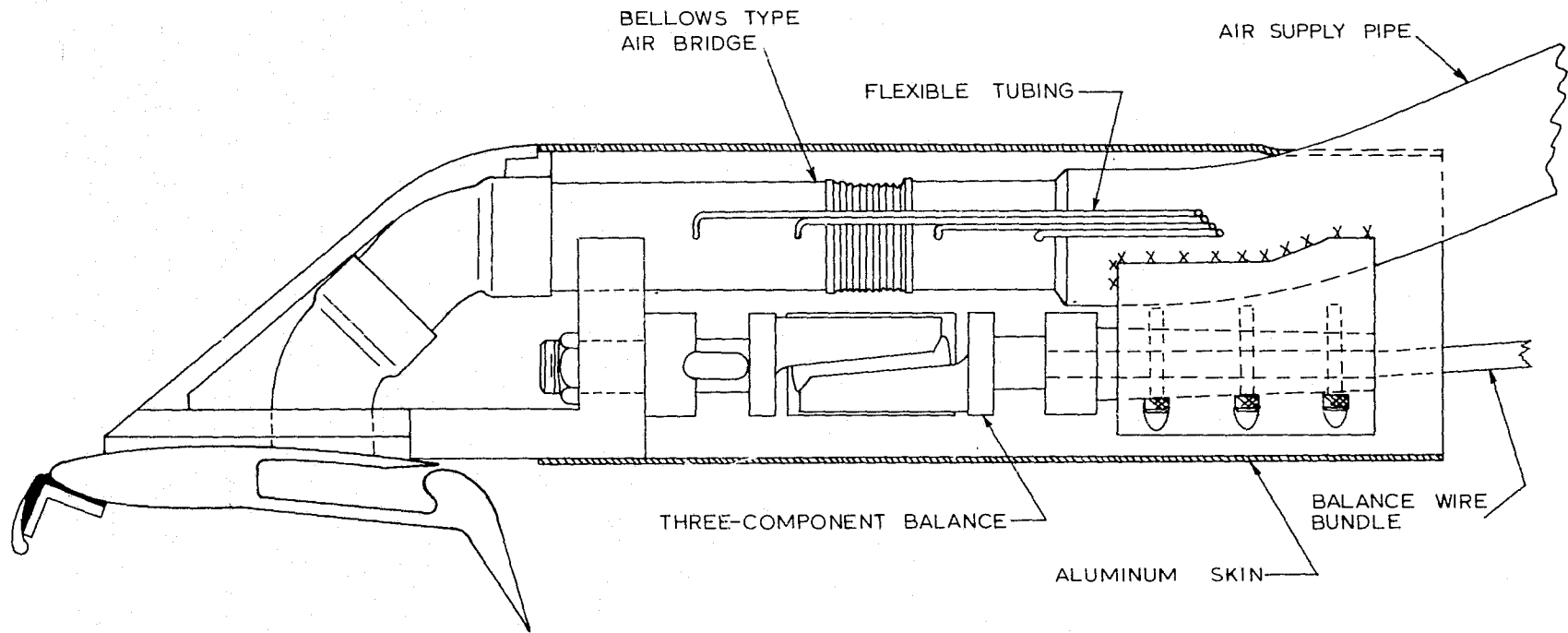


FIGURE 2.3 BALANCE AND AIR BRIDGE DETAILS

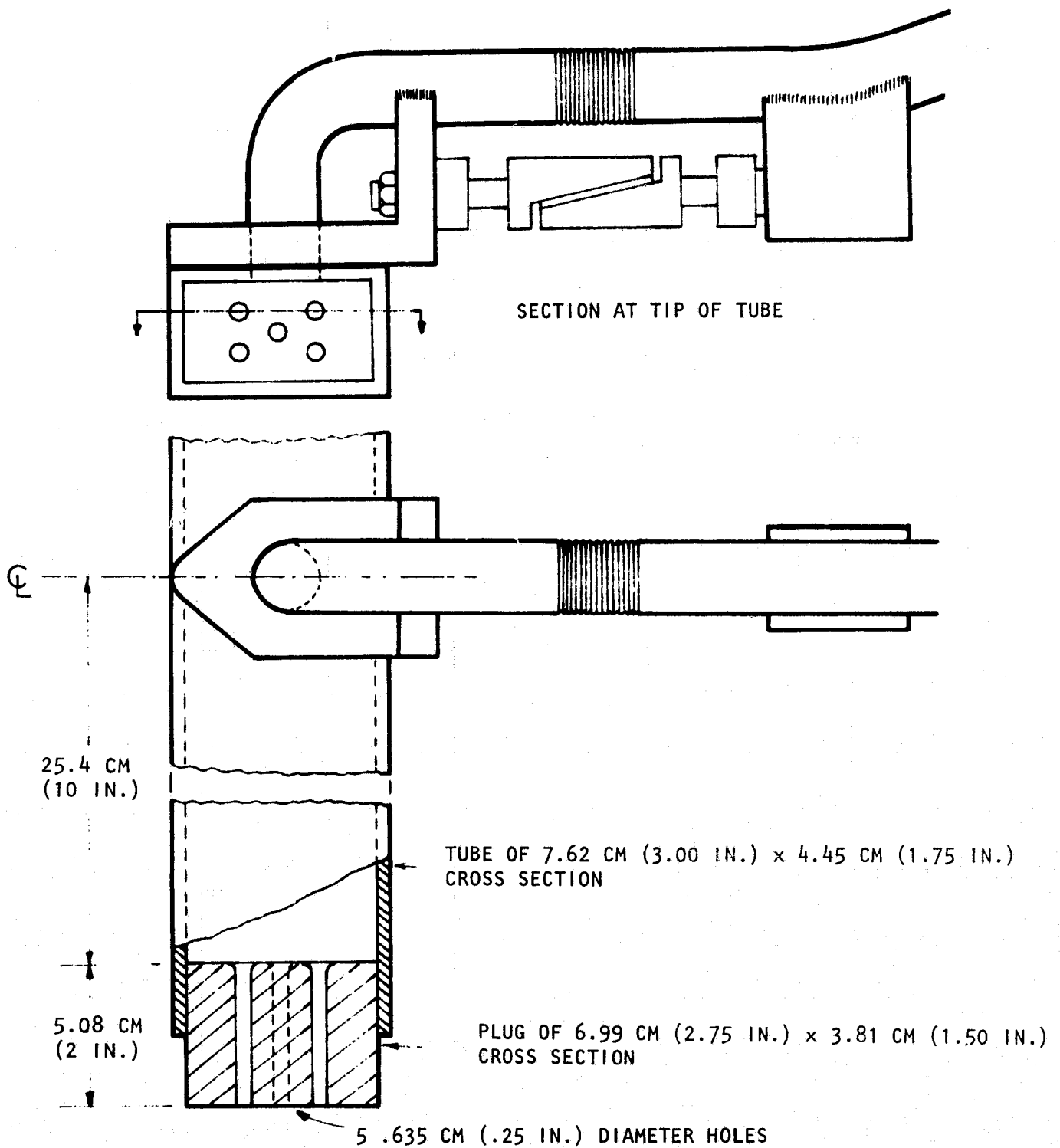


FIGURE 2.4 DYNAMIC PRESSURE TARE CALIBRATION RIG

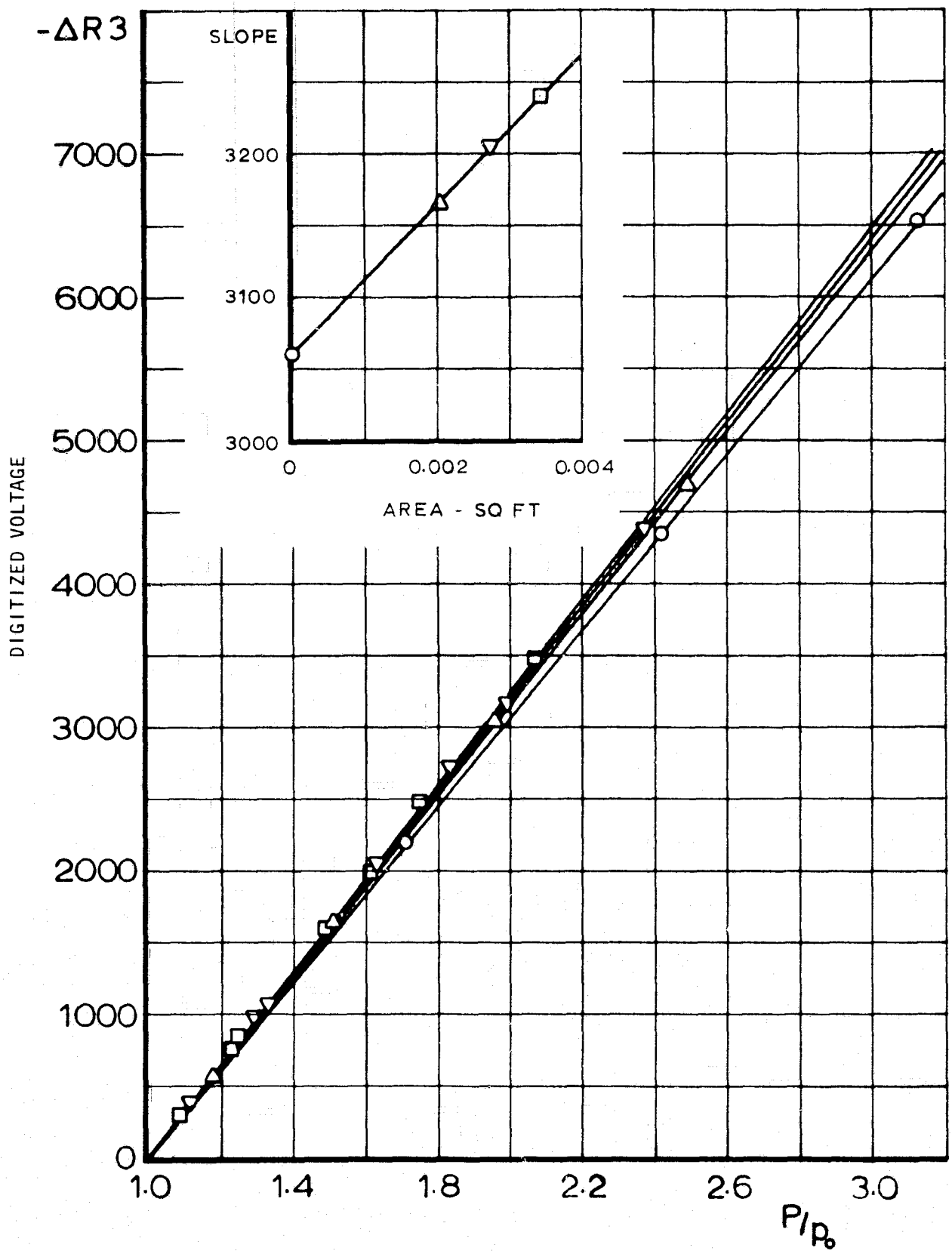


FIGURE 2.5 AXIAL FORCE PRESSURE TARE

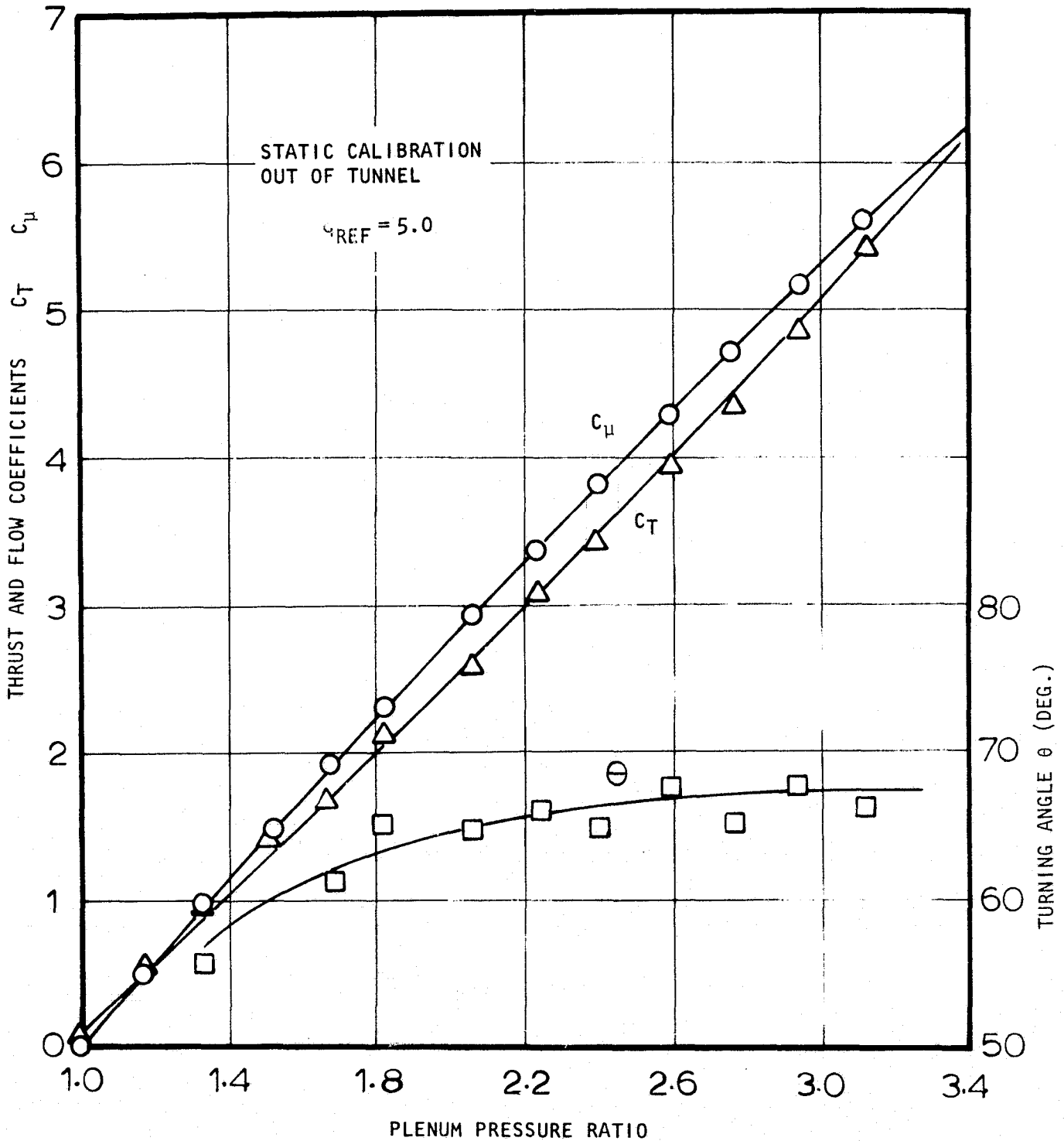


FIGURE 2.6 RESULT OF STATIC THRUST CALIBRATION, $q = 5$ PSF

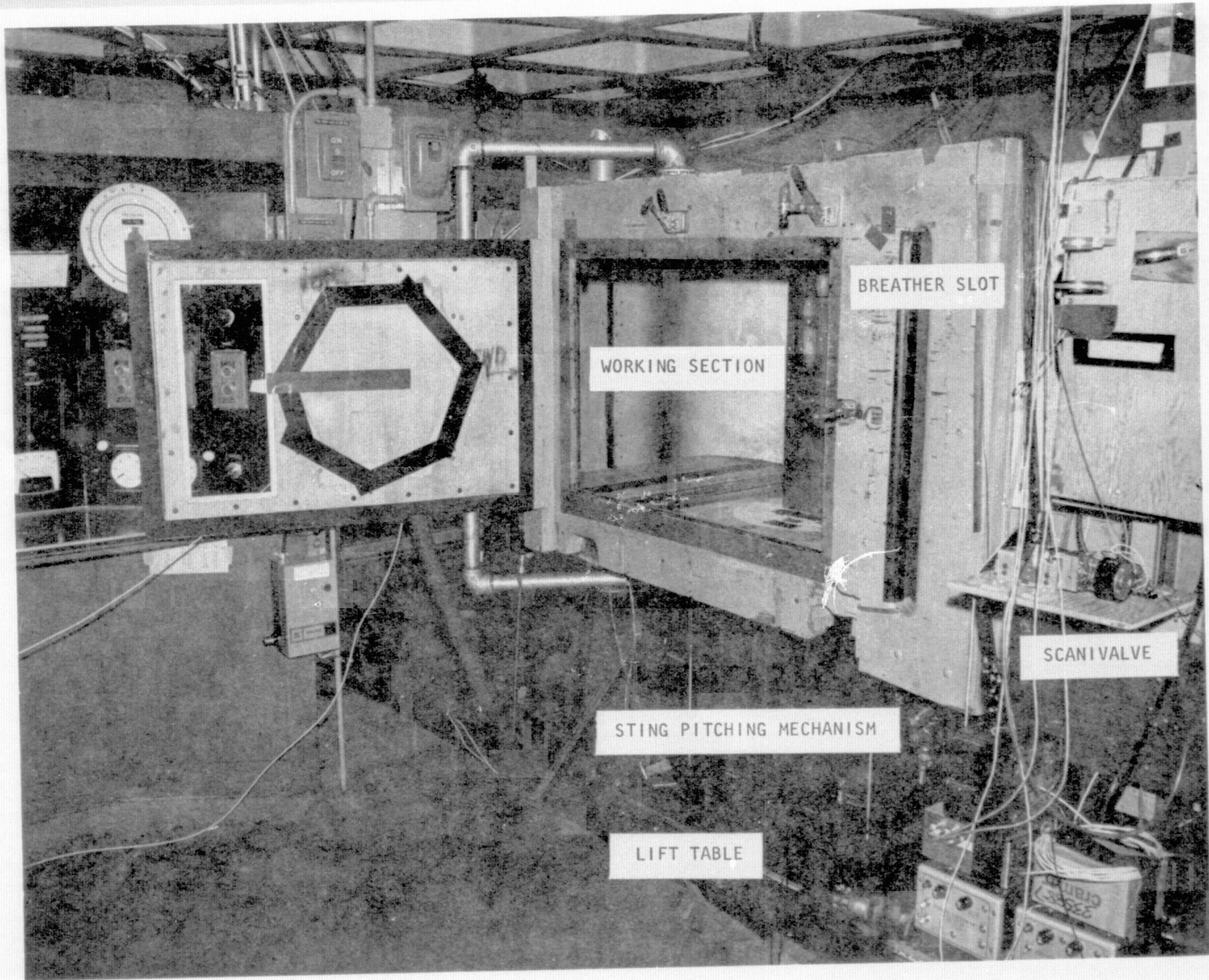
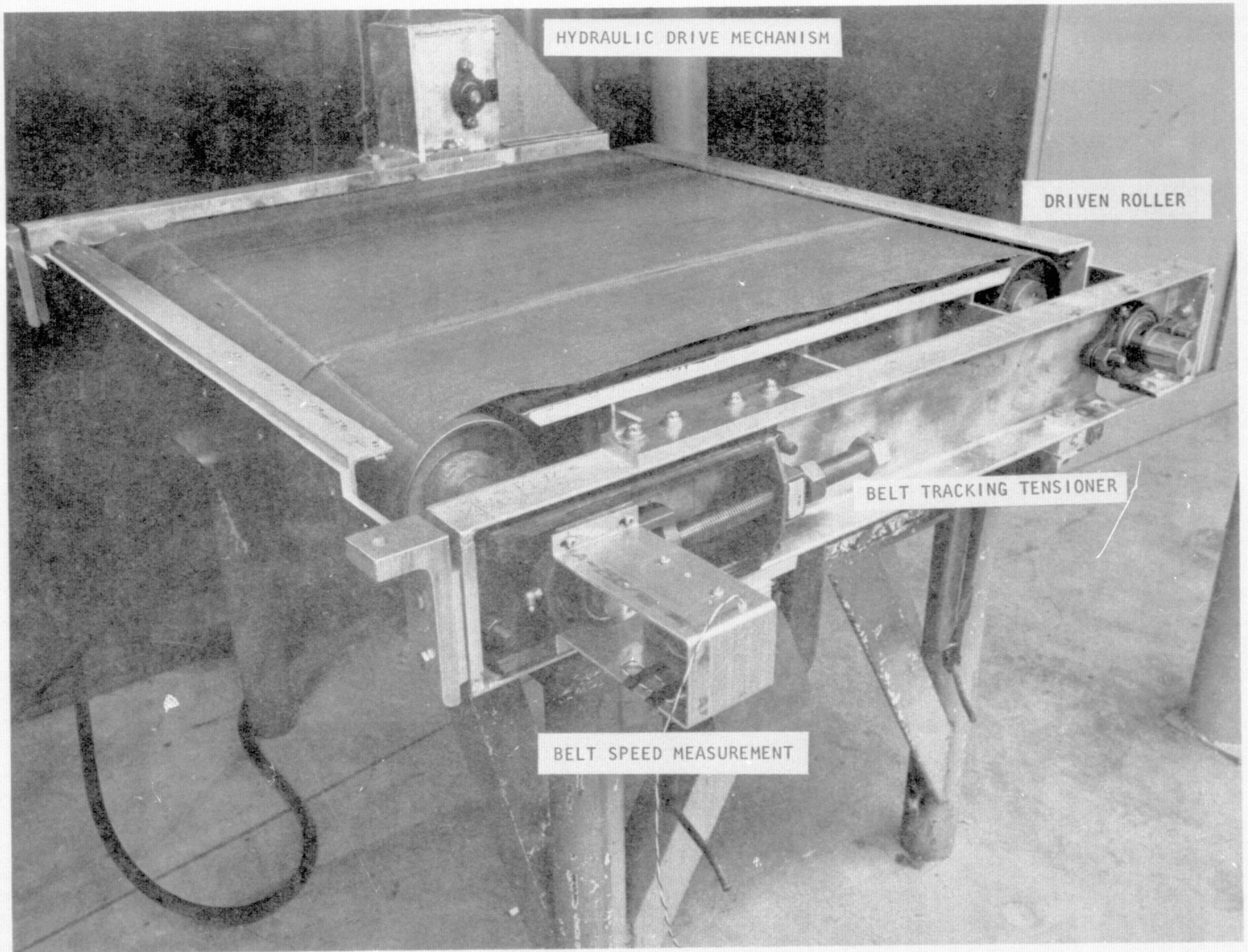


FIGURE 3.1 THE 30 x 42 INCH LOW SPEED WIND TUNNEL



HYDRAULIC DRIVE MECHANISM

DRIVEN ROLLER

BELT TRACKING TENSIONER

BELT SPEED MEASUREMENT

FIGURE 3.2 THE MOVING BELT GROUND PLANE

ORIGINAL PAGE IS
OF POOR QUALITY

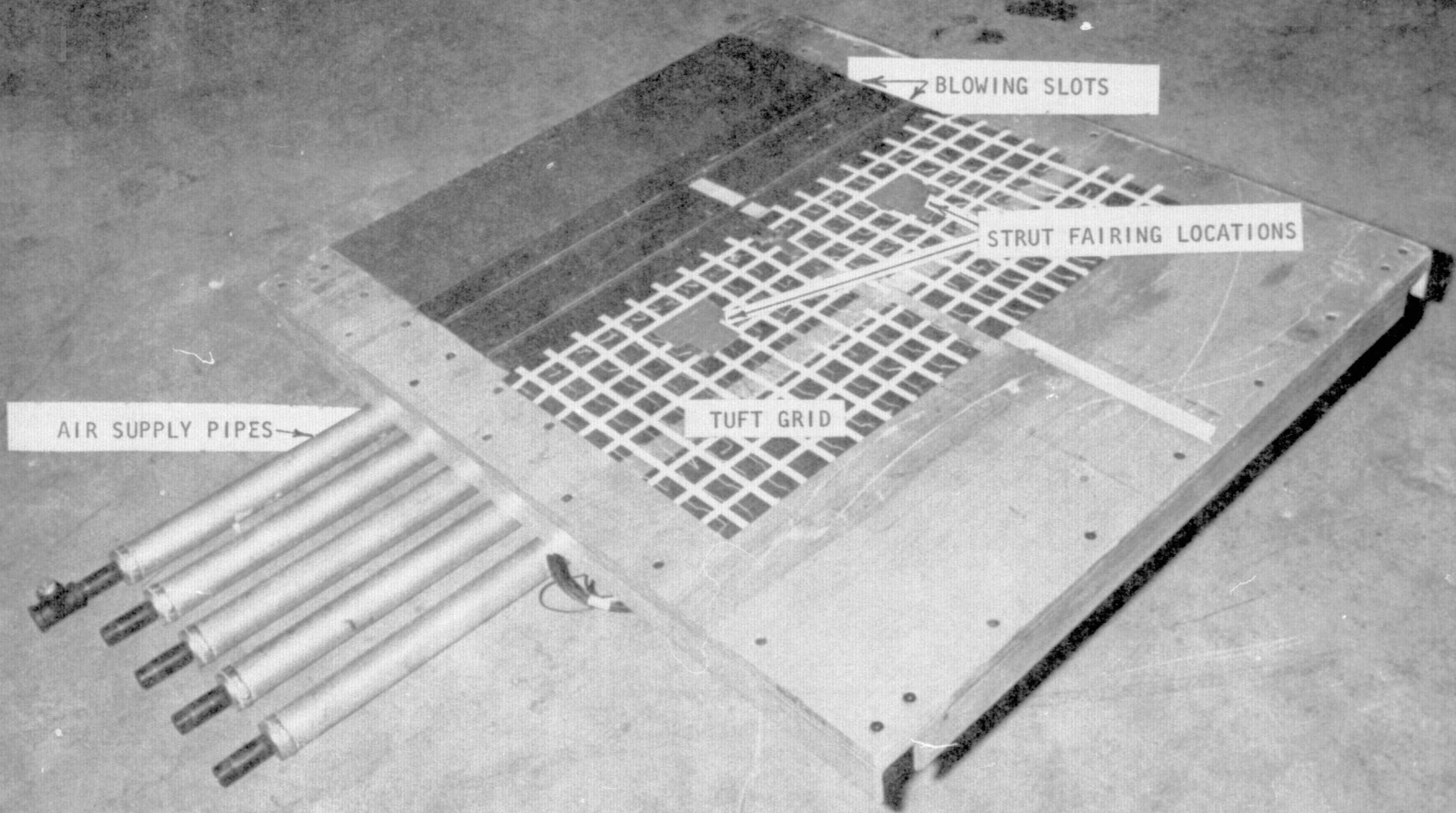
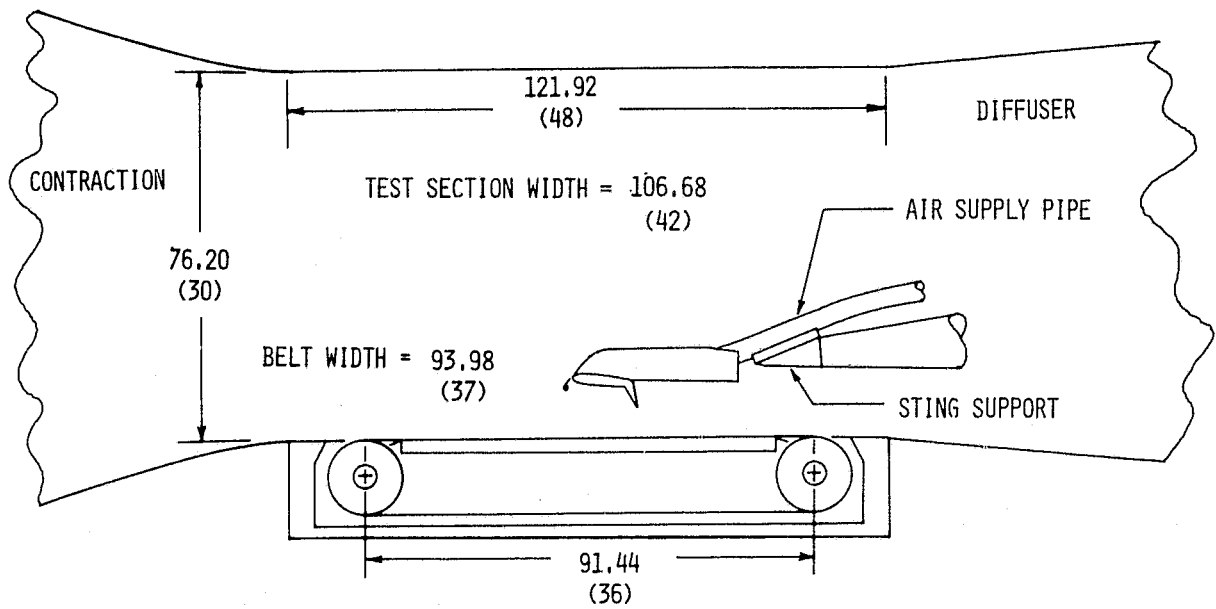
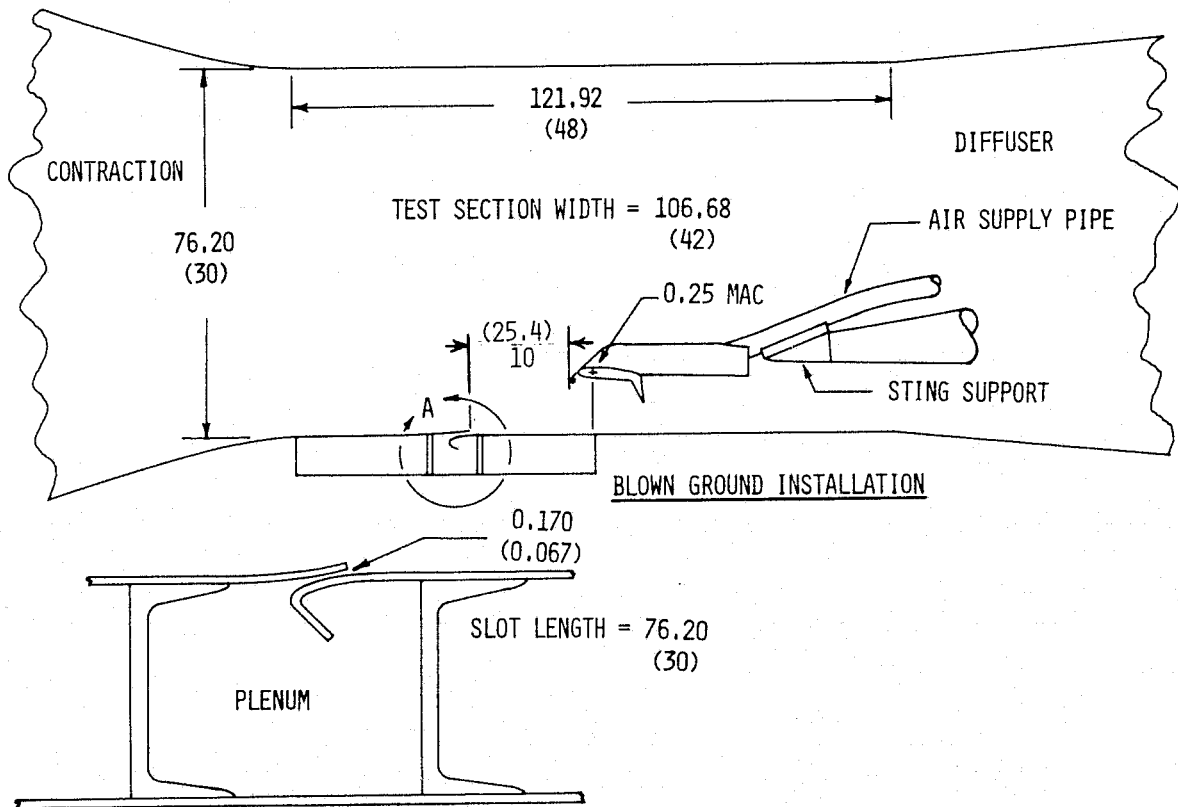


FIGURE 3.3 THE BOUNDARY LAYER CONTROL GROUND PLANE



MOVING BELT GROUND PLANE INSTALLATION



A : SLOT DETAILS

FIGURE 3.4 DIMENSIONS OF THE MOVING BELT AND THE BLOWN GROUND PLANES

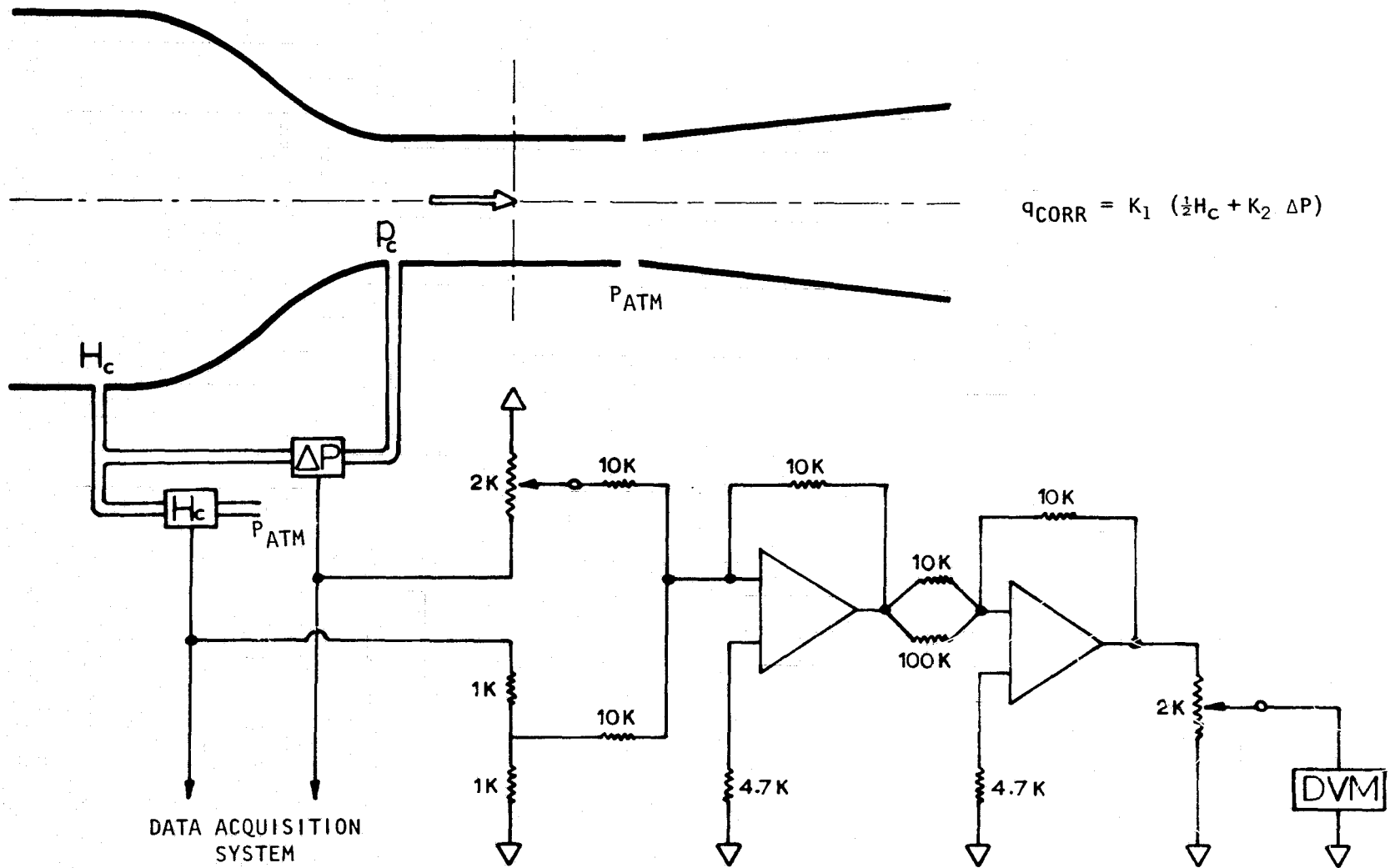


FIGURE 3.5 ON-LINE GENERATION OF CORRECTED 'q'

CONFIGURATION							DATA							RUNS PER CONFIG.		
Symbol	Fuse.	Wing	In'bd. Slats	Tips	Out'bd. Slats	Tail I _H	BALANCE		WAKE RAKE				FLOW VIZ.			
							C _μ	RUNS	C _μ	2Y/b	Z	α	RUNS		TUFTS	RUNS
A-1	X	X	X				B	9						X	9	18
	X	X	X						C	-.35	C	0	3			3
	X	X	X						C	-.70	C	0	3			3
	X	X	X						C	-1.05	C	0	3			3
A-2	X	X	X			20	B	9								9
	X	X	X			20			D	-.35	C	0	2			2
	X	X	X			20			D	-.70	A	0	2			2
	X	X	X			20			D	-1.05	A	0	2			2
B	X	X	X	X	X		B	9						X	9	18
	X	X	X	X	X				C	-.35	C	0	3			3
	X	X	X	X	X				C	-.70	B	0	3			3
	X	X	X	X	X				C	-1.05	B	0	3			3
	X	X	X	X	X				C	-1.40	B	0	3			3
C	X	X	X	X	X	20	B	9								9
D	X	X		X	X	20	B	9								9
E	X	X		X	X		B	9						X	9	18
F	X	X					B	9						X	9	18
G	X	X	X	X			B	9						X	9	18
H	X	X	X	X		20	B	9								9

Total Including Unnumbered Flow Visualization Runs = 153

FIGURE 3.6(a) RUN SCHEDULE FOR CENTER TUNNEL PRODUCTION RUNS

The α schedule is determined by the value of C_{μ} as shown below.

C_{μ} VALUES	α VALUES ~ DEGREES
0.0 to 0.7	0, 2, 4, 6, 8, 10, 15
1.0 to 10.0	0, 5, 10, 15, 20, 25, 30, 35

C_{μ} SCHEDULE	C_{μ} VALUES
A	0.4, 0.7, 1.0, 2.0, 3.0
B	0.0, 0.2, 0.4, 1.0, 2.0, 4.0, 6.0, 8.0, 10.0
C	0.4, 1.0, 3.0
D	0.4, 3.0

RAKE HEIGHT SCHEDULE, Z	RAKE HEIGHT RELATIVE TO WING REFERENCE PLANE	$2Z/b$
A	-1.0 to 0	$\Delta = .05$
B	-.9 to .3	$\Delta = .05$
C	-.8 to .2	$\Delta = .05$

FIGURE 3.6(b) ANGLE OF ATTACK, MOMENTUM COEFFICIENT, AND WAKE RAKE HEIGHT SCHEDULES FOR CENTER TUNNEL TESTING

CONFIGURATION										DATA AT INDICATED C_{μ} SCHEDULES											
Symbol	Fuse.	Wing	In 'bd. Slats	Tips	Out 'bd. Slats	Tail H	Short Struts	Long Struts	GROUND TREATMENT	MODEL HEIGHT H/C	BALANCE		WALL STATICS		WAKE RAKE		WAKE RAKE TAIL FOLLOWING		B L RAKE		RUNS PER CONFIGURATION
											C_{μ}	RUNS	C_{μ}	RUNS	C_{μ}	RUNS	C_{μ}	RUNS	C_{μ}	RUNS	
A-1	X	X	X						MB	2	A	5	C	3	C	3	E	4			12
	X	X	X						MB	1	A	5	C	3	C	3	E	4			12
A-2	X	X	X			0			MB	2	A	5			C	3					8
	X	X	X			0			MB	1	A	5			C	3					8
B	X	X	X	X	X				MB	2	A	5	C	3	C	3					8
	X	X	X	X	X				MB	1	A	5	C	3	C	3					8
C	X	X	X	X	X	0			MB	2	A	5									5
	X	X	X	X	X	0			MB	1	A	5									5
A-1	X	X	X						BLC	2	A	5			C	3	E	4	A	5	12
	X	X	X						BLC	1	A	5			C	3	E	4	A	5	12
A-2	X	X	X			0			BLC	2	A	5			C	3			A	5	8
	X	X	X			0			BLC	1	A	5			C	3			A	5	8
B	X	X	X	X	X				BLC	2	A	5			C	3			A	5	8
	X	X	X	X	X				BLC	1	A	5			C	3			A	5	8
C	X	X	X	X	X	0			BLC	2	A	5							A	5	5
	X	X	X	X	X	0			BLC	1	A	5							A	5	5
C ¹	X	X	X	X	X	0		X	BLC	2	A	5									5
C ¹	X	X	X	X	X	0	X		BLC	1	A	5									5

TOTAL RUNS 142

FIGURE 3.7(a) RUN SCHEDULE FOR GROUND EFFECTS PRODUCTION RUNS

C_{μ} Schedule	C_{μ} Values
A	0.4, 0.7, 1.0, 2.0, 3.0
B	0.0, 0.2, 0.4, 1.0, 2.0, 4.0, 6.0, 8.0, 10.0
C	0.4, 1.0, 3.0
D	0.4, 3.0
E	0.4, 1.0, 3.0, 4.0

The α schedule is determined by the value of C_{μ} and model height for each run as shown below.

Model Height, H/C	C_{μ} Values	α Values ~ Degrees
2	0.0 to 0.7	0, 2, 4, 6, 8, 10, 15
2	1.0 to 10.0	0, 2, 5, 10, 15, 20
1	0.0 to 0.7	0, 2, 4, 6, 8, 10, 15
1	1.0 to 10.0	0, 2, 4, 6, 8, 10, 15

FIGURE 3.7(b) ANGLE OF ATTACK AND MOMENTUM COEFFICIENT SCHEDULES FOR GROUND EFFECTS TESTS

$$H/C = 3.75$$

FLOOR TUFT OBSERVATION

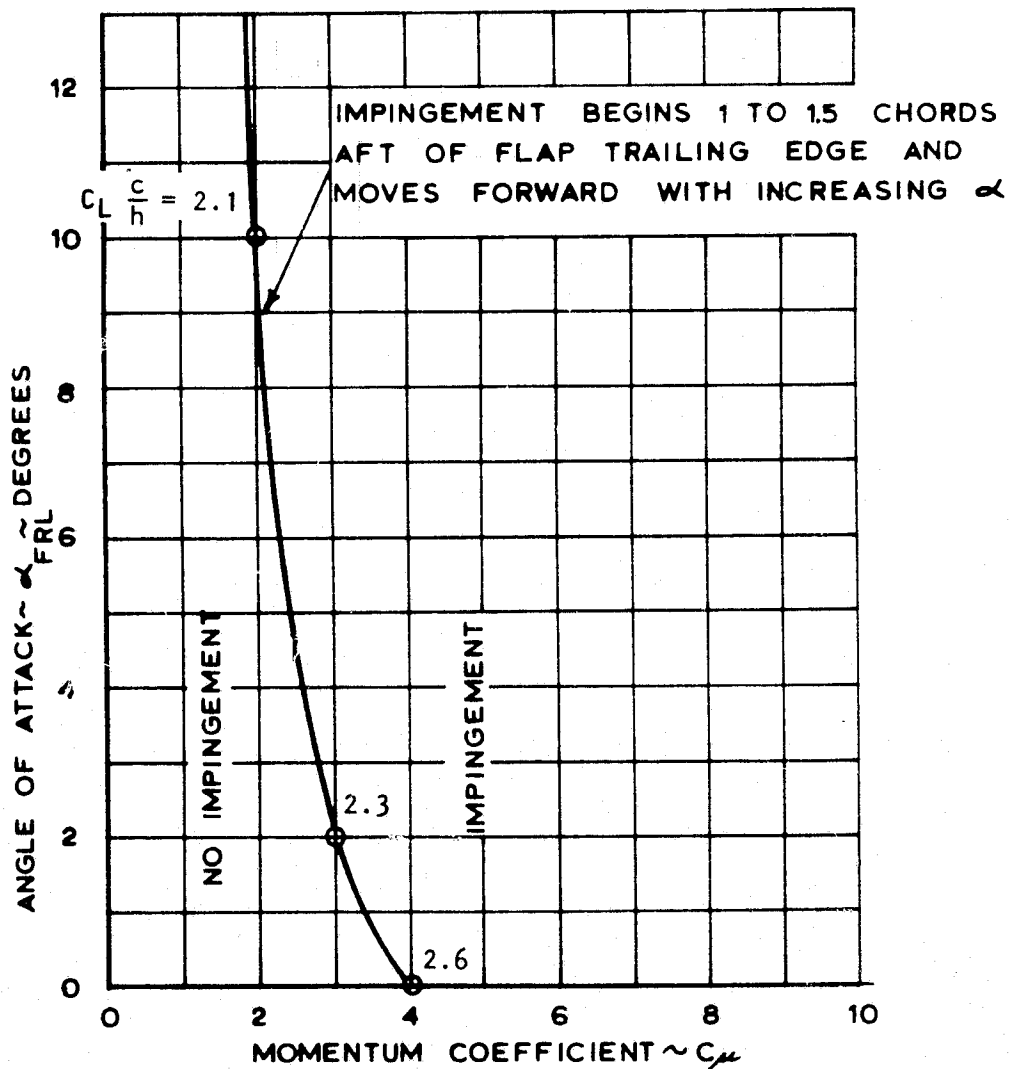


FIGURE 4.1 CONDITIONS FOR FLOOR IMPINGEMENT:
BASIC CONFIGURATION (A-1)

(No incidence correction)

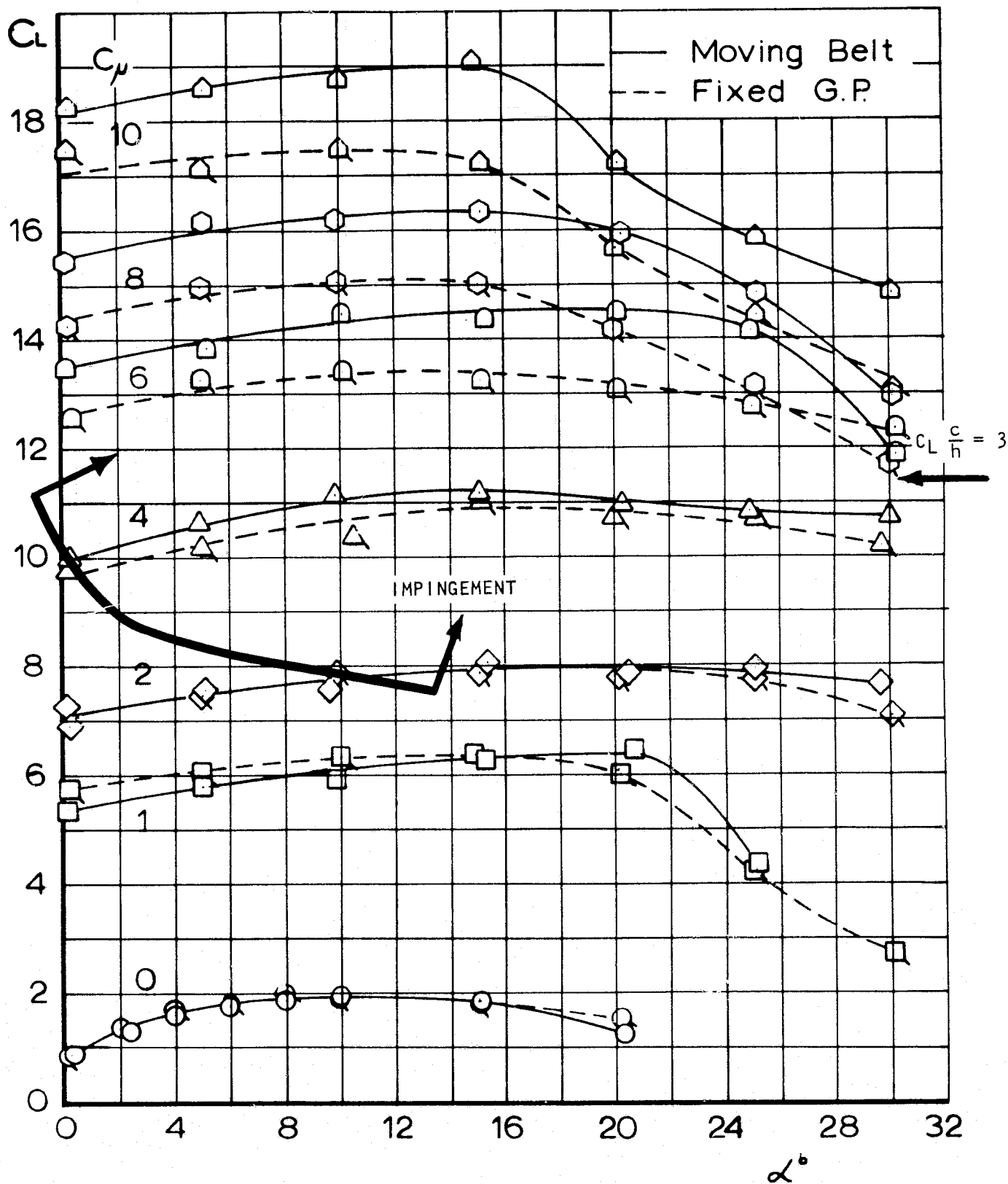


FIGURE 4.2 LIFT AT CENTER TUNNEL: FIXED VERSUS MOVING GROUND

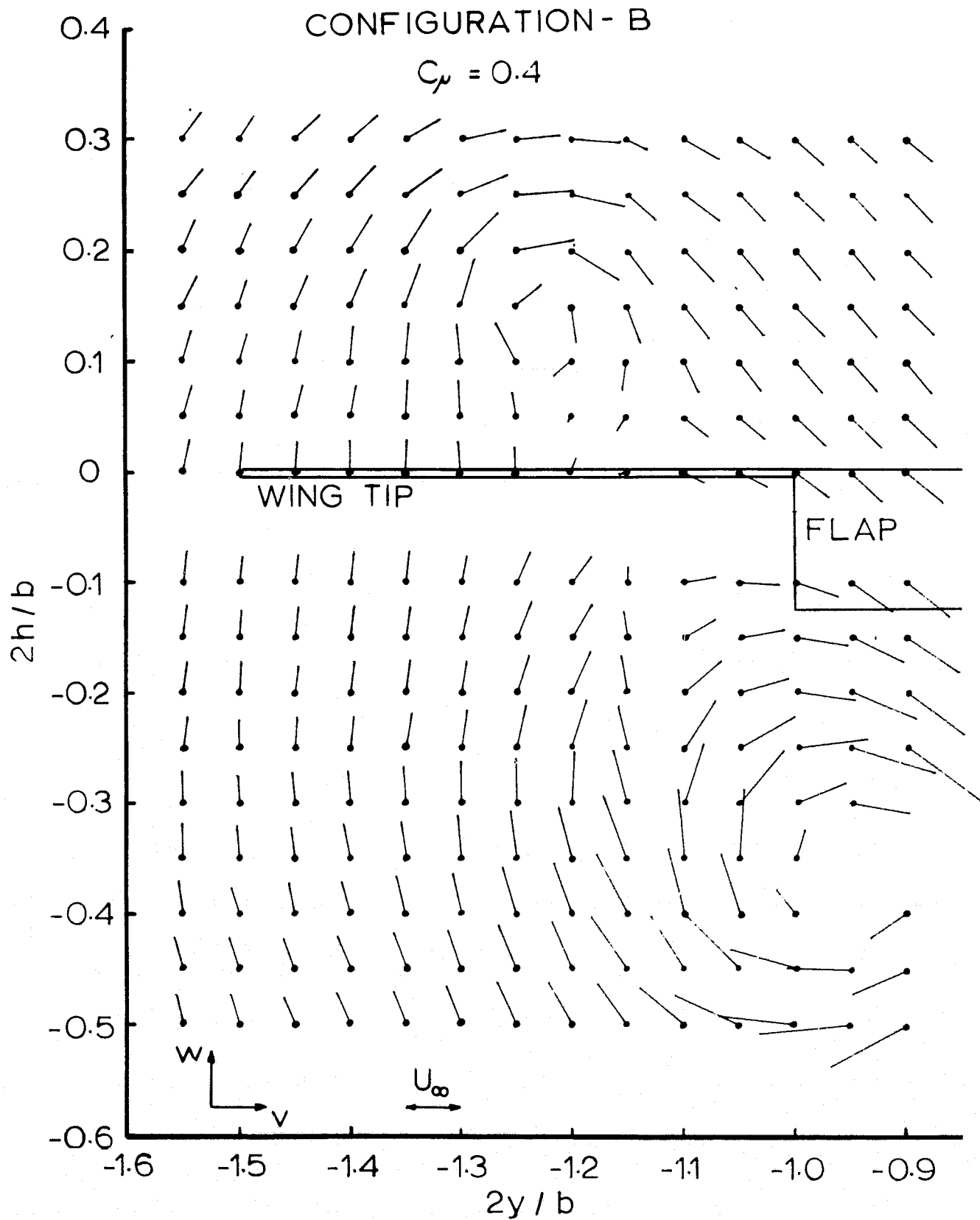


FIGURE 4.3 CROSS-FLOW VECTORS JUST AFT OF TAILPLANE POSITION ($x/c = 3.88$)

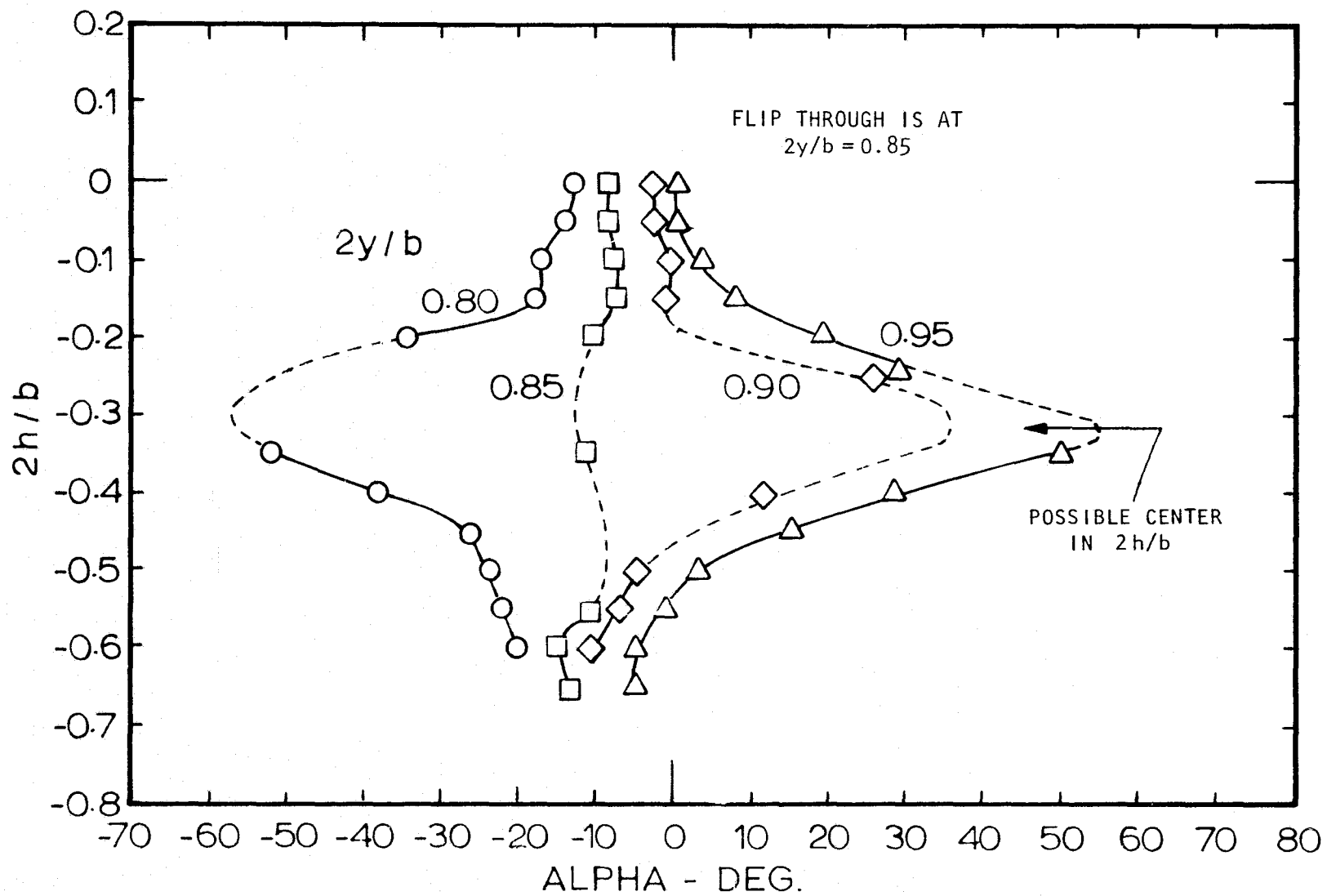


FIGURE 4.4 UPWASH ANGLES IN THE VICINITY OF A FLAP-END VORTEX

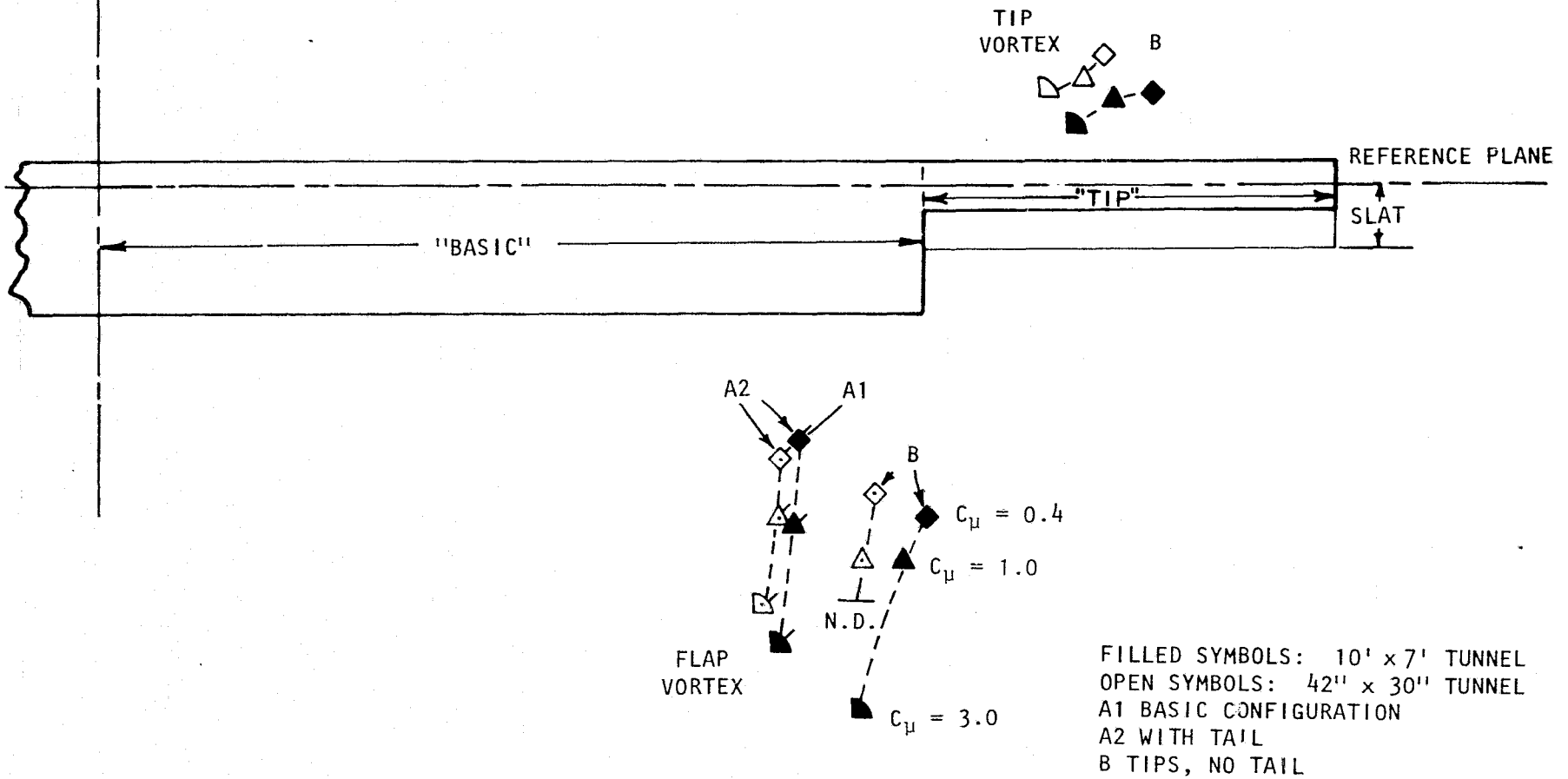


FIGURE 4.5 MEASURED VORTEX POSITIONS IN LARGE AND SMALL WIND TUNNELS
 $x/c = 3.88$

BASIC CONFIGURATION 'A1' (A2)					
C_{μ}		0.4	1.0	3.0	FLAP-END VORTEX
42" x 30" TUNNEL	2y/b	(0.83)	(0.83)	(0.80)	
	2h/b	(-0.32)	(-0.40)	(-0.50)	
10' x 7' TUNNEL	2y/b	0.85 (0.85)	0.84 (N.D.)	0.82 (0.83)	
	2h/b	-0.32 (-0.30)	-0.41 (N.D.)	-0.54 (-0.55)	

WITH TIPS ADDED 'B'					
C_{μ}		0.4	1.0	3.0	FLAP-END VORTEX
42" x 30" TUNNEL	2y/b	0.94	0.93	N.D.	
	2h/b	-0.37	-0.45	N.D.	
10' x 7' TUNNEL	2y/b	1.02	0.97	0.93	
	2h/b	-0.40	-0.45	-0.63	
42" x 30" TUNNEL	2y/b	1.22	1.20	1.15	
	2h/b	0.15	0.14	0.13	
10' x 7' TUNNEL	2y/b	1.28	1.23	1.18	
	2h/b	0.10	0.10	0.07	

FIGURE 4.6 MEASURED TRAILING VORTEX POSITIONS IN LARGE AND SMALL WIND TUNNELS (TABULATION), $x/c = 3.88$

BASIC WING WITH SLATS, TAIL ON (A-2)
CENTER TUNNEL

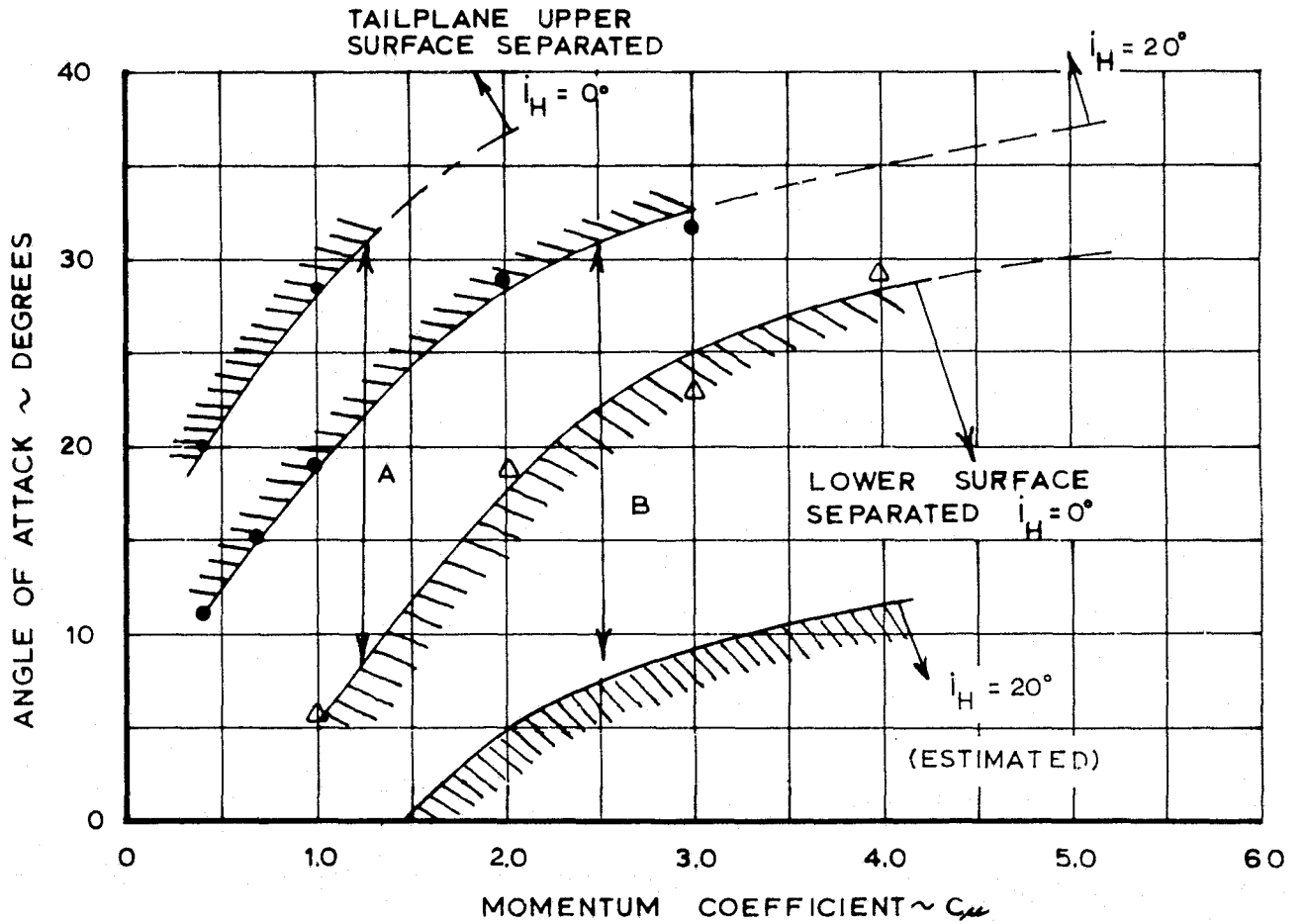


FIGURE 4.7 CONDITIONS FOR POSITIVE AND NEGATIVE TAIL-STALL

FILLED SYMBOLS: 7x10' TUNNEL
 OPEN SYMBOLS: 30x42 TUNNEL
 TAGGED SYMBOLS: TAIL ON $\sim i_H = 20^\circ$

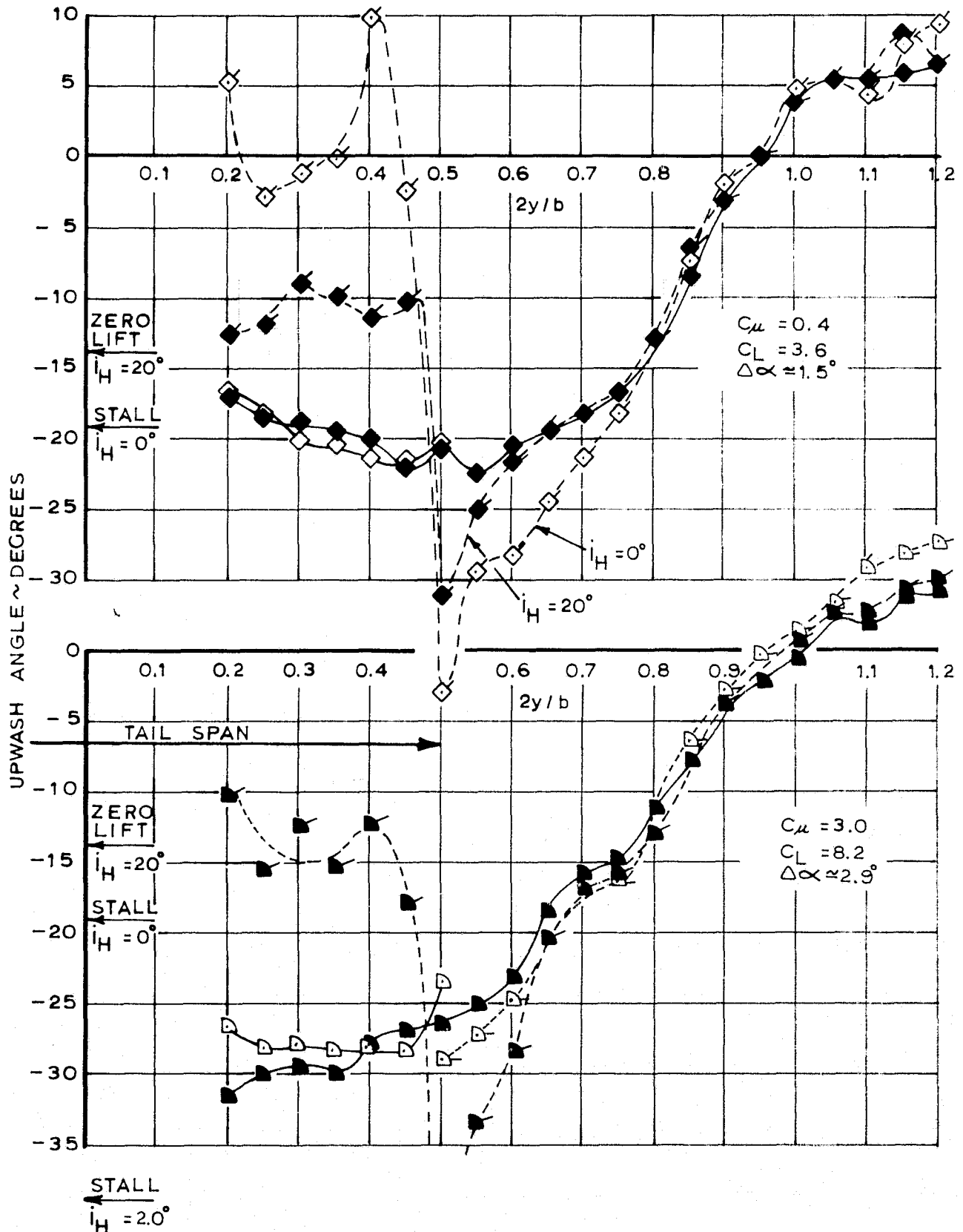


FIGURE 4.8 UPWASH AFT OF TAILPLANE LOCATION IN LARGE AND SMALL TUNNELS. BASIC CONFIGURATION (A) WITH AND WITHOUT TAILPLANE. $\alpha = 0^\circ$

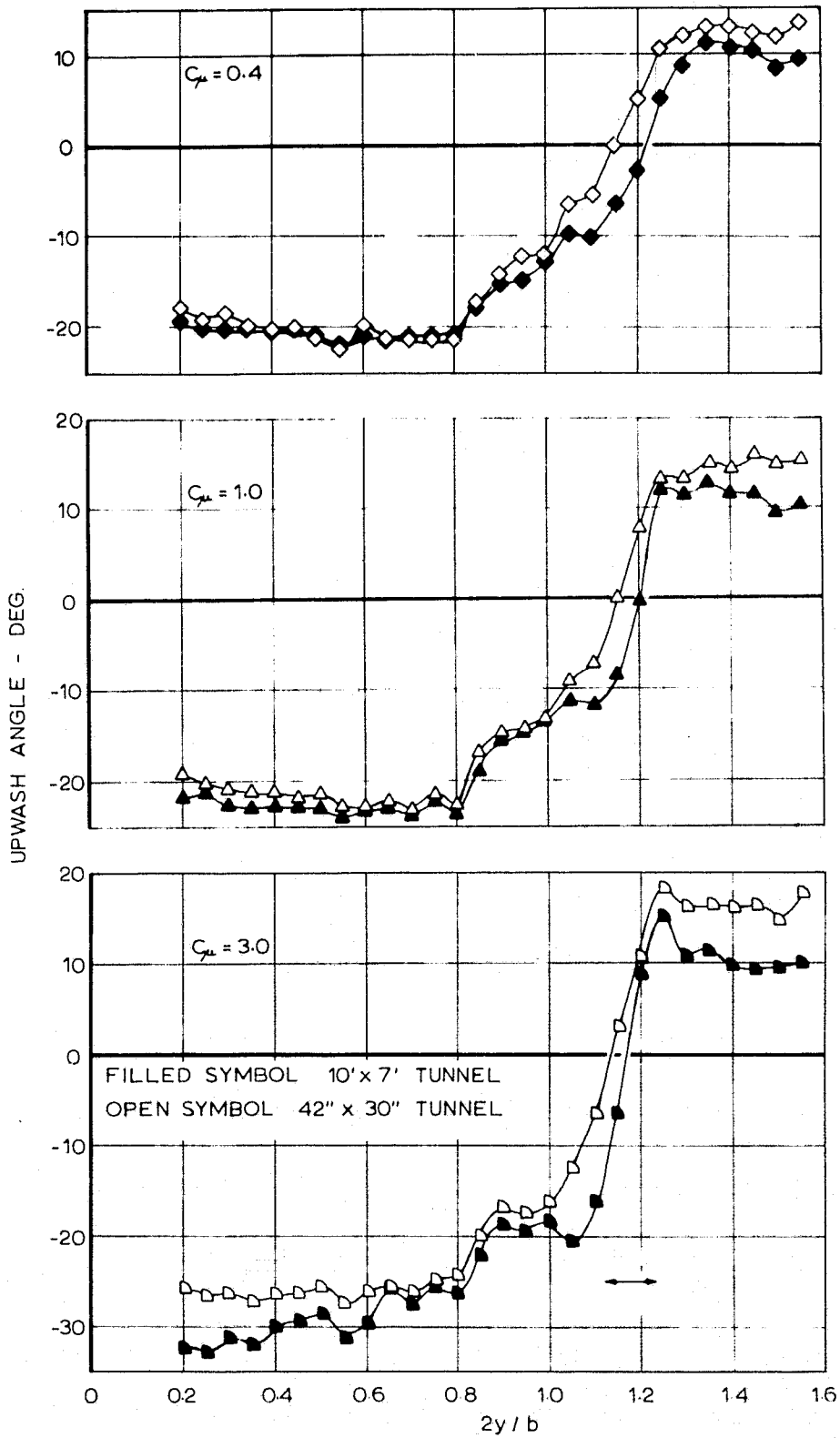


FIGURE 4.9 UPWASH AFT OF TAILPLANE LOCATION IN LARGE AND SMALL TUNNELS. CONFIGURATION WITH TIPS (B) AT $\alpha = 0^\circ$.

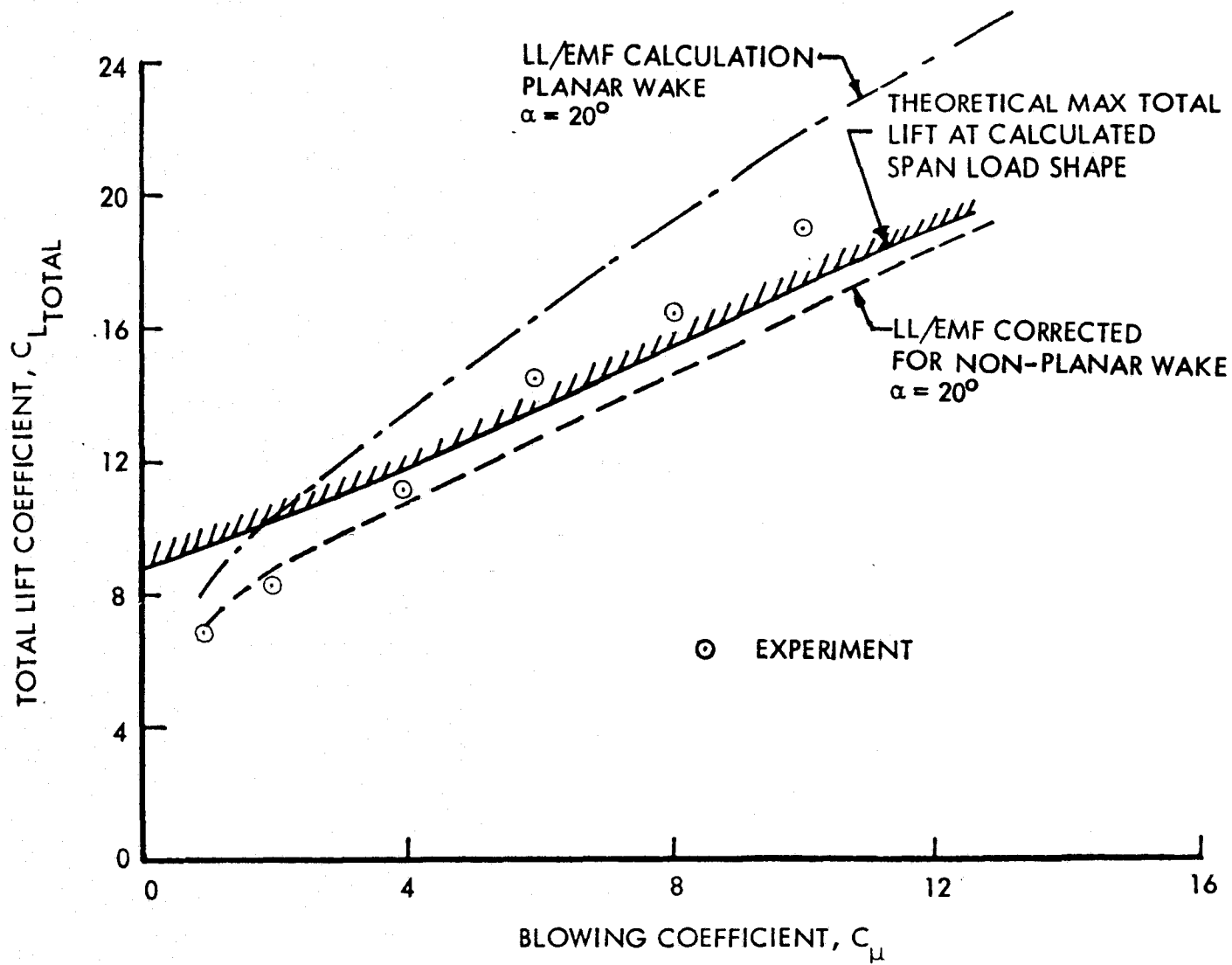
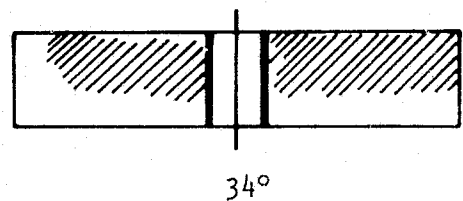
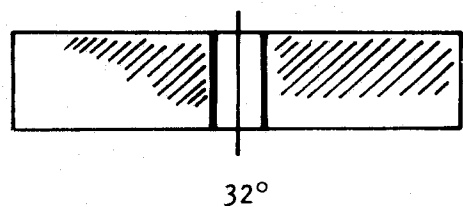
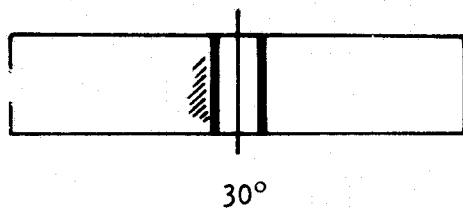


FIGURE 4.10 LIFT PERFORMANCE IN RELATION TO "LIMIT LIFT"

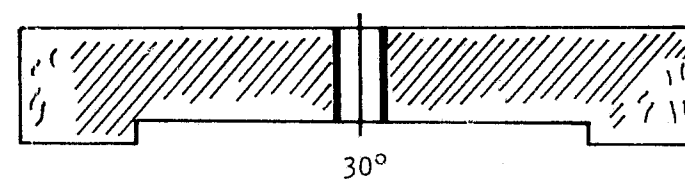
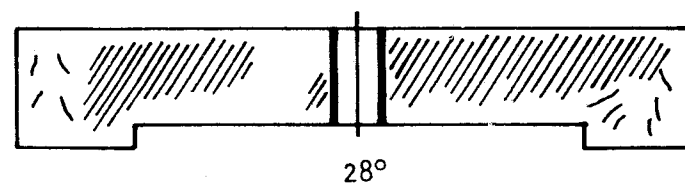
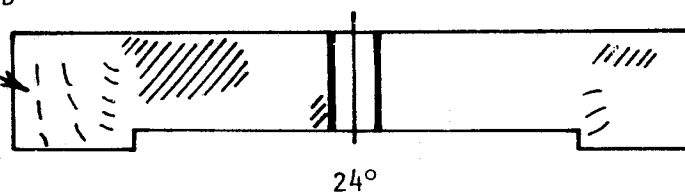
(a) BASIC CONFIGURATION (A)



STALL STARTS NEAR WING ROOT

(b) CONFIGURATION WITH TIPS (B)

STRONG INFLOW
TOWARD FLAP END



STALL STARTS OUTBOARD

FIGURE 4.11 TYPICAL STALL PATTERNS, FROM TUFT OBSERVATIONS, $C_{L\alpha} = 2.0$

ANGLE OF ATTACK - DEGREES

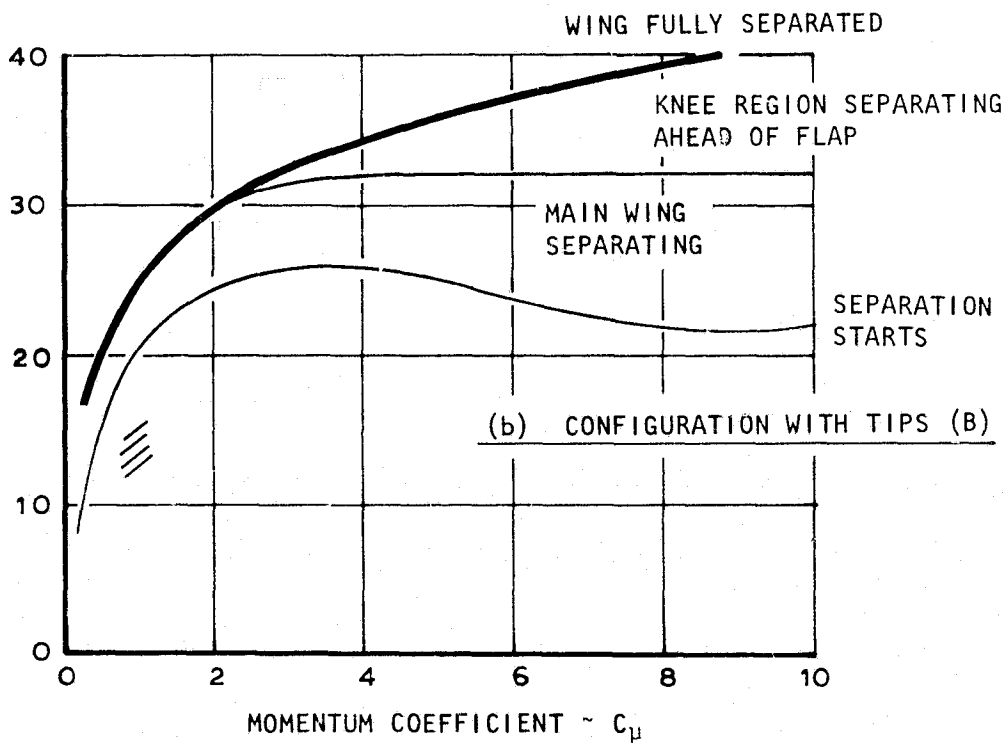
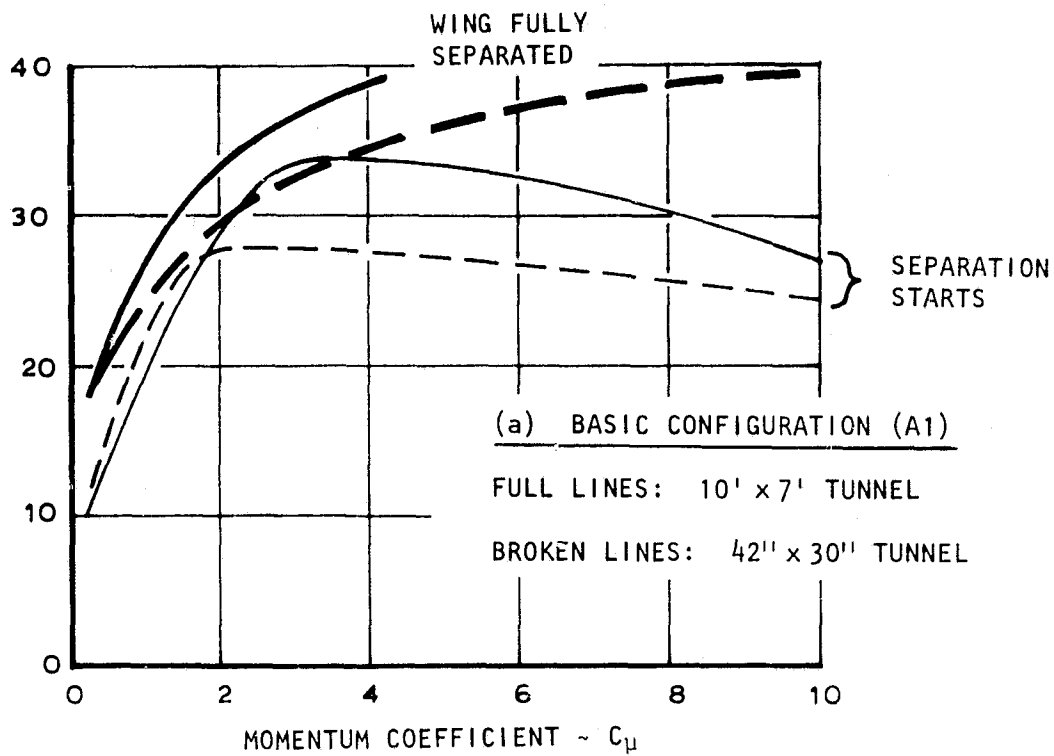


FIGURE 4.12 CONDITIONS FOR WING STALL

SYM	CORRECTIONS APPLIED	DYNAMIC PRESSURE CORRECTION
◇	NONE	———— (CONSTANT ΔP)
△	BLOCKAGE	CALCULATED (CONSTANT ΔP)
□	BLOCKAGE AND WALL	CALCULATED (CONSTANT ΔP)
○	BLOCKAGE AND WALL	AUTOMATIC ~ ON LINE

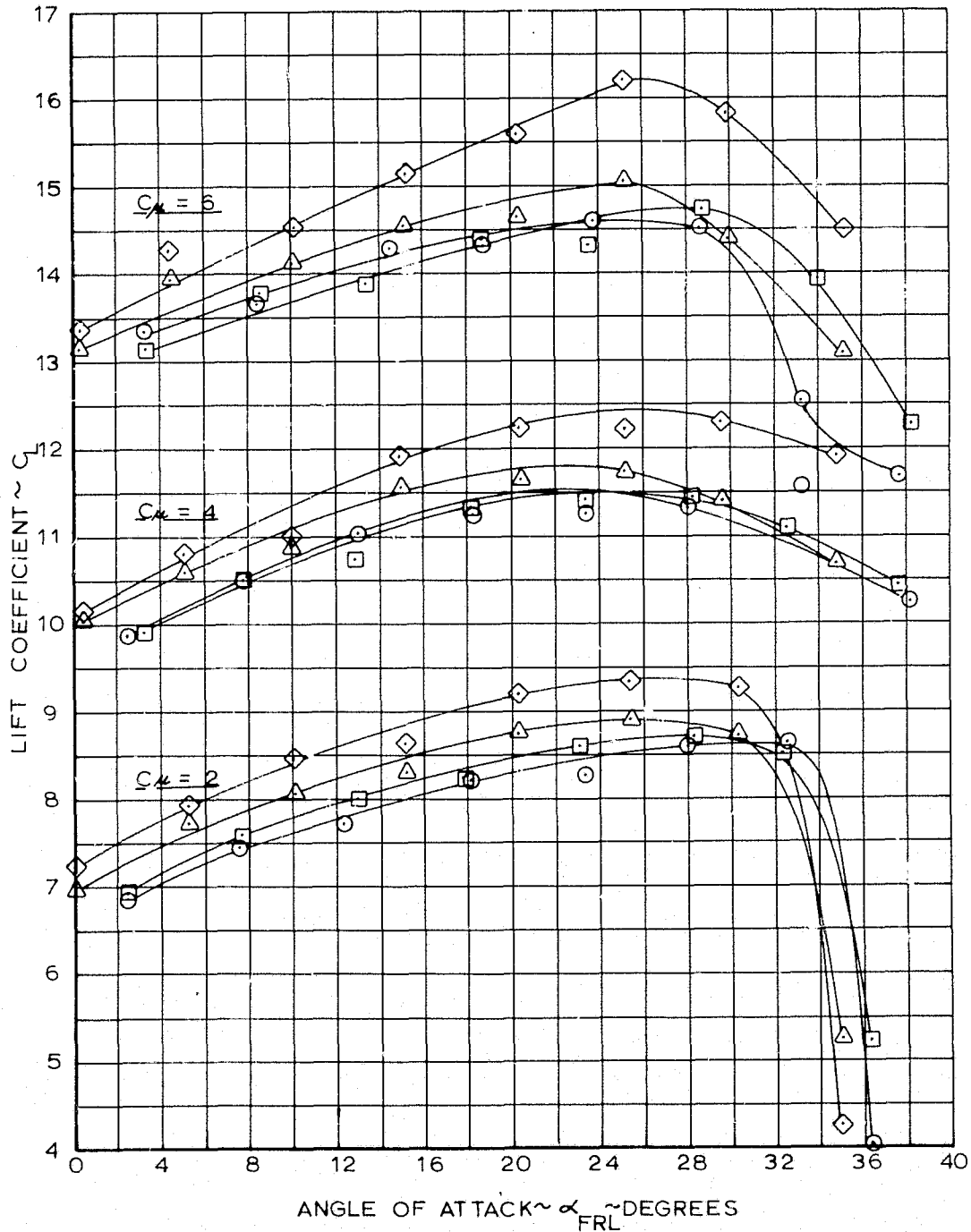


FIGURE 5.1 APPLICATION OF CORRECTIONS TO SMALL TUNNEL RESULTS

CONFIGURATION: BASIC WING WITH SLATS (A-1)
 MODEL ON TUNNEL CENTERLINE

- NASA/AAMRDL 7x10 FOOT WIND TUNNEL ~ NO CORRECTIONS
- LOCKHEED 30x42 INCH WIND TUNNEL ~ CORRECTED FOR BLOCKAGE AND WALL EFFECTS

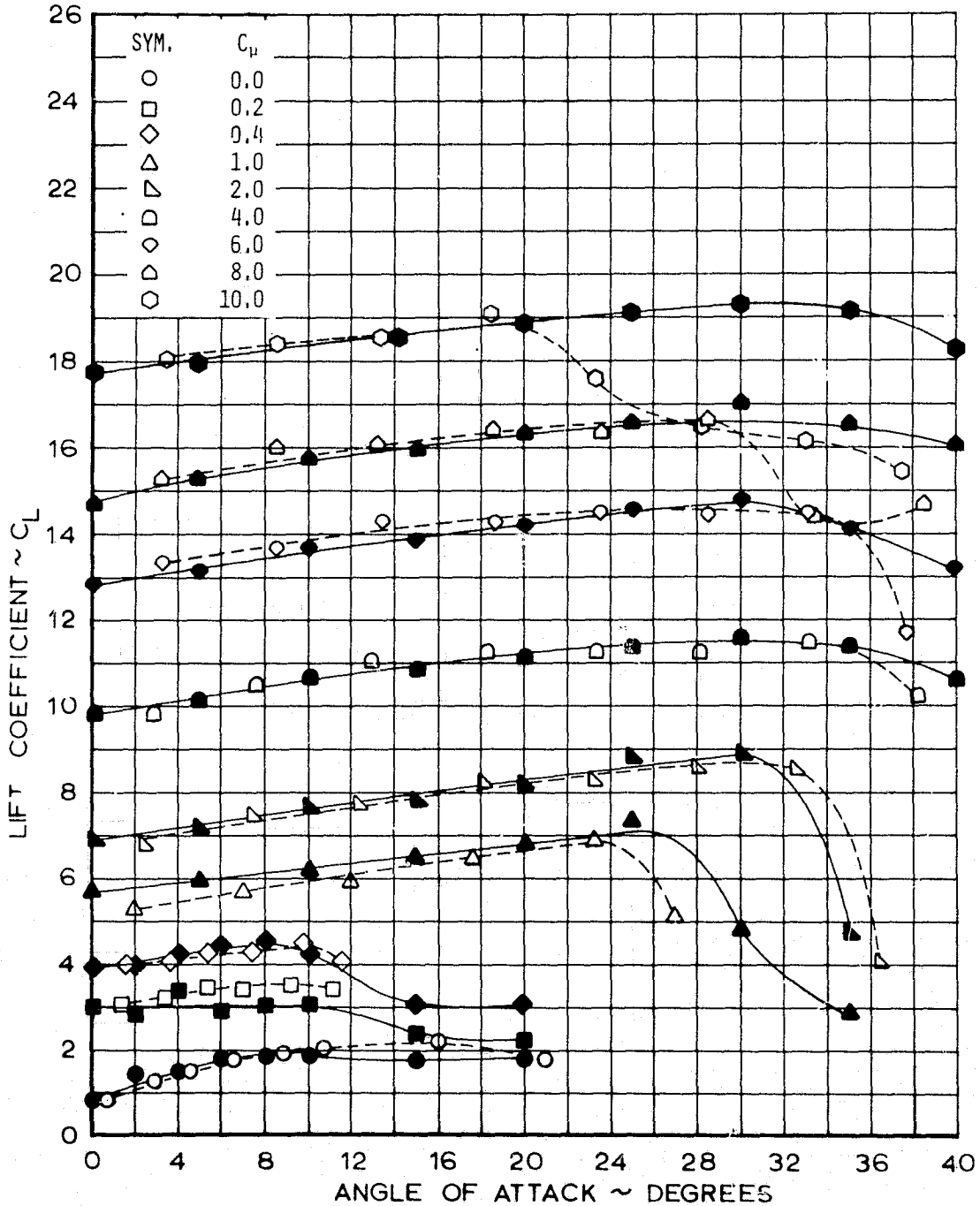


FIGURE 5-2(a) BASIC LIFT DATA

CONFIGURATION: BASIC WING WITH SLATS (A-1)
 MODEL ON TUNNEL CENTERLINE

- NASA/AAMRDL 7x10 FOOT WIND TUNNEL ~ NO CORRECTIONS
- LOCKHEED 30x42 INCH WIND TUNNEL ~ CORRECTED FOR BLOCKAGE AND WALL EFFECTS

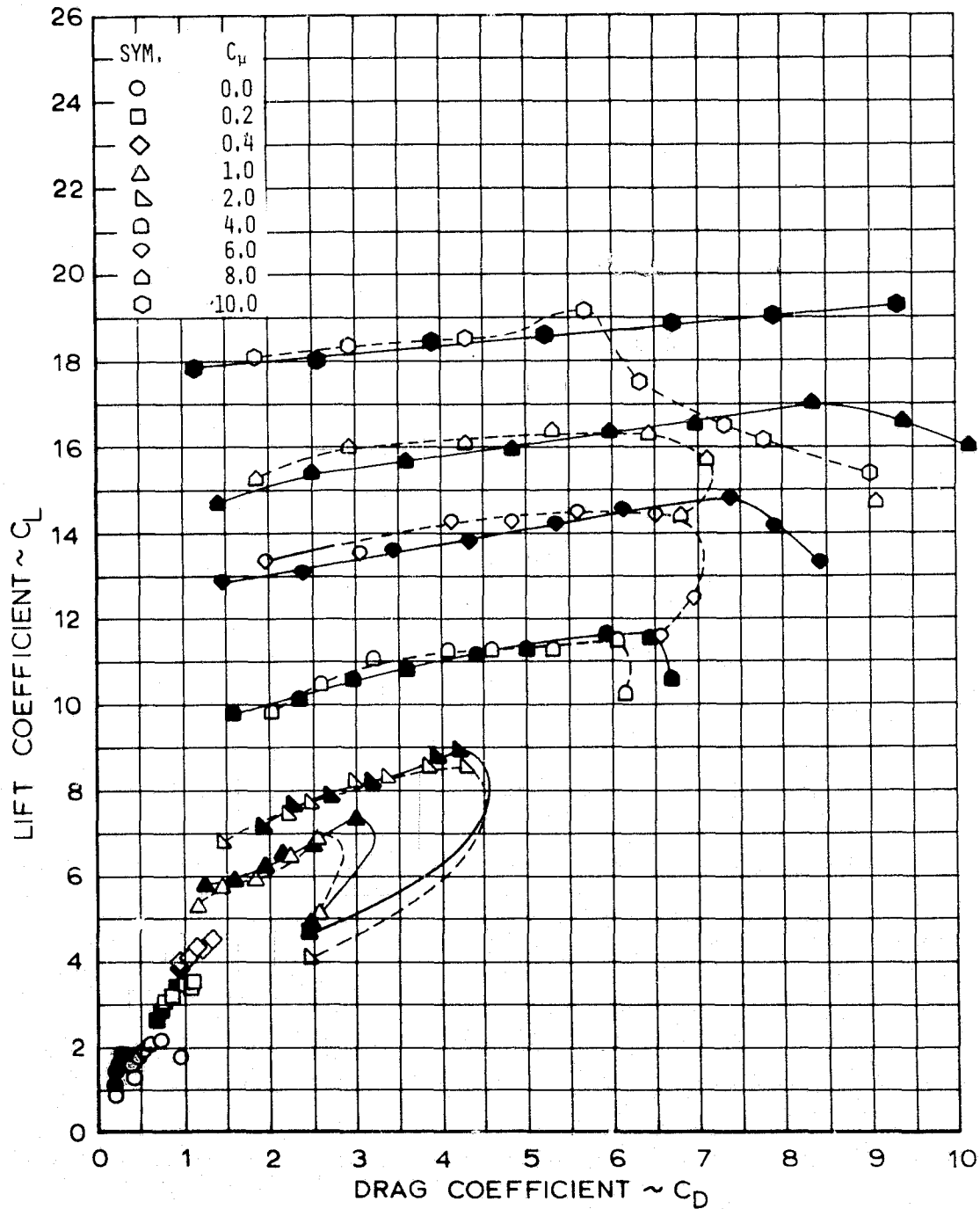


FIGURE 5-2(b) BASIC DRAG DATA.

CONFIGURATION: BASIC WING WITH SLATS (A-1)
 MODEL ON TUNNEL CENTERLINE

- NASA/AAMRDL 7x10 FOOT WIND TUNNEL ~ NO CORRECTIONS
- LOCKHEED 30x42 INCH WIND TUNNEL ~ CORRECTED FOR BLOCKAGE AND WALL EFFECTS

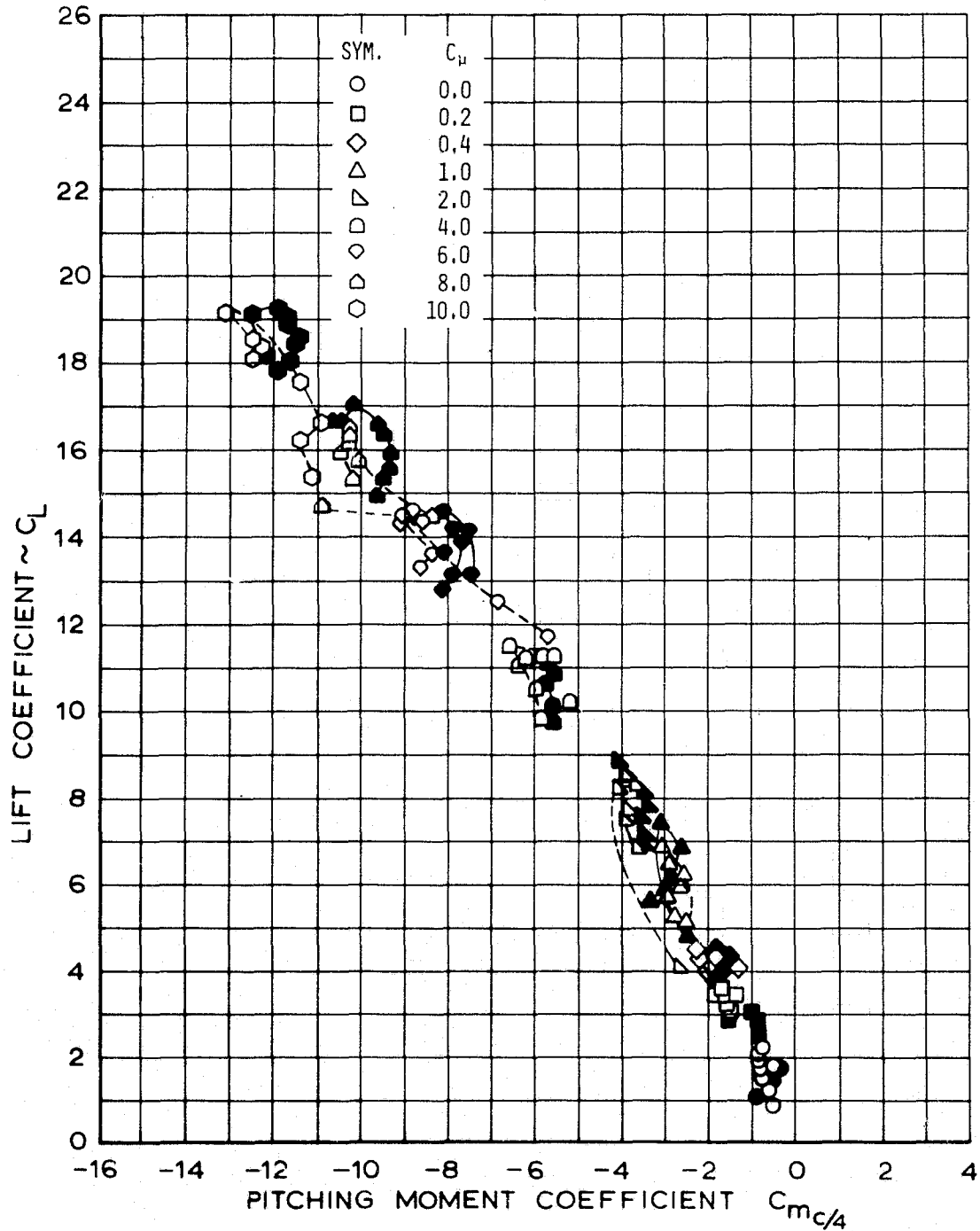


FIGURE 5-2(c) BASIC PITCHING MOMENT DATA

CONFIGURATION: BASIC WING, SLATS REMOVED (F)
 MODEL ON TUNNEL CENTERLINE

- NASA/AAMRDL 7x10 FOOT WIND TUNNEL ~ NO CORRECTIONS
- LOCKHEED 30x42 INCH WIND TUNNEL ~ CORRECTED FOR BLOCKAGE AND WALL EFFECTS

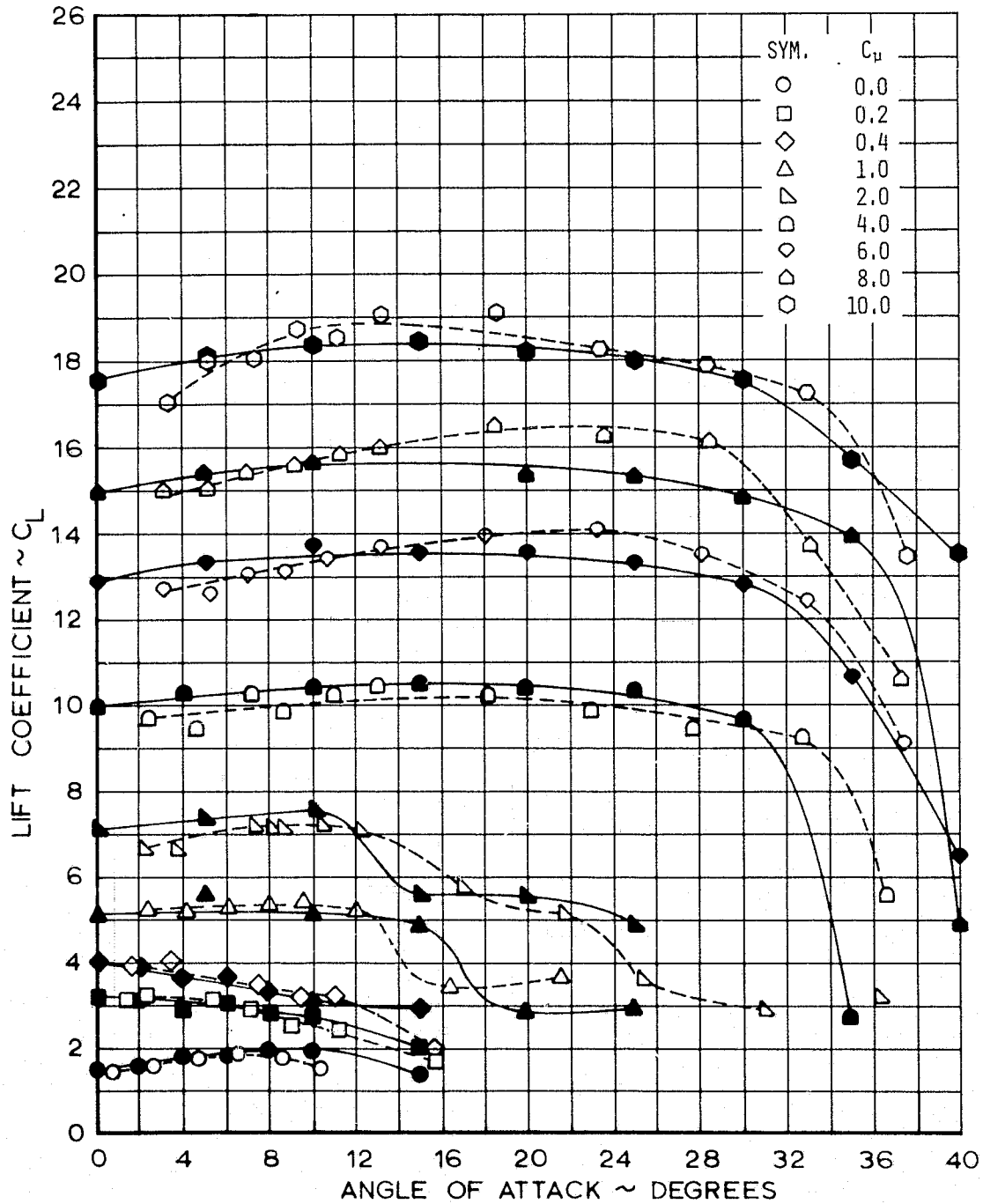


FIGURE 53(a) BASIC LIFT DATA

CONFIGURATION: BASIC WING, SLATS REMOVED (F)
 MODEL ON TUNNEL CENTERLINE

- NASA/AAMRDL 7x10 FOOT WIND TUNNEL ~ NO CORRECTIONS
- LOCKHEED 30x42 INCH WIND TUNNEL ~ CORRECTED FOR BLOCKAGE AND WALL EFFECTS

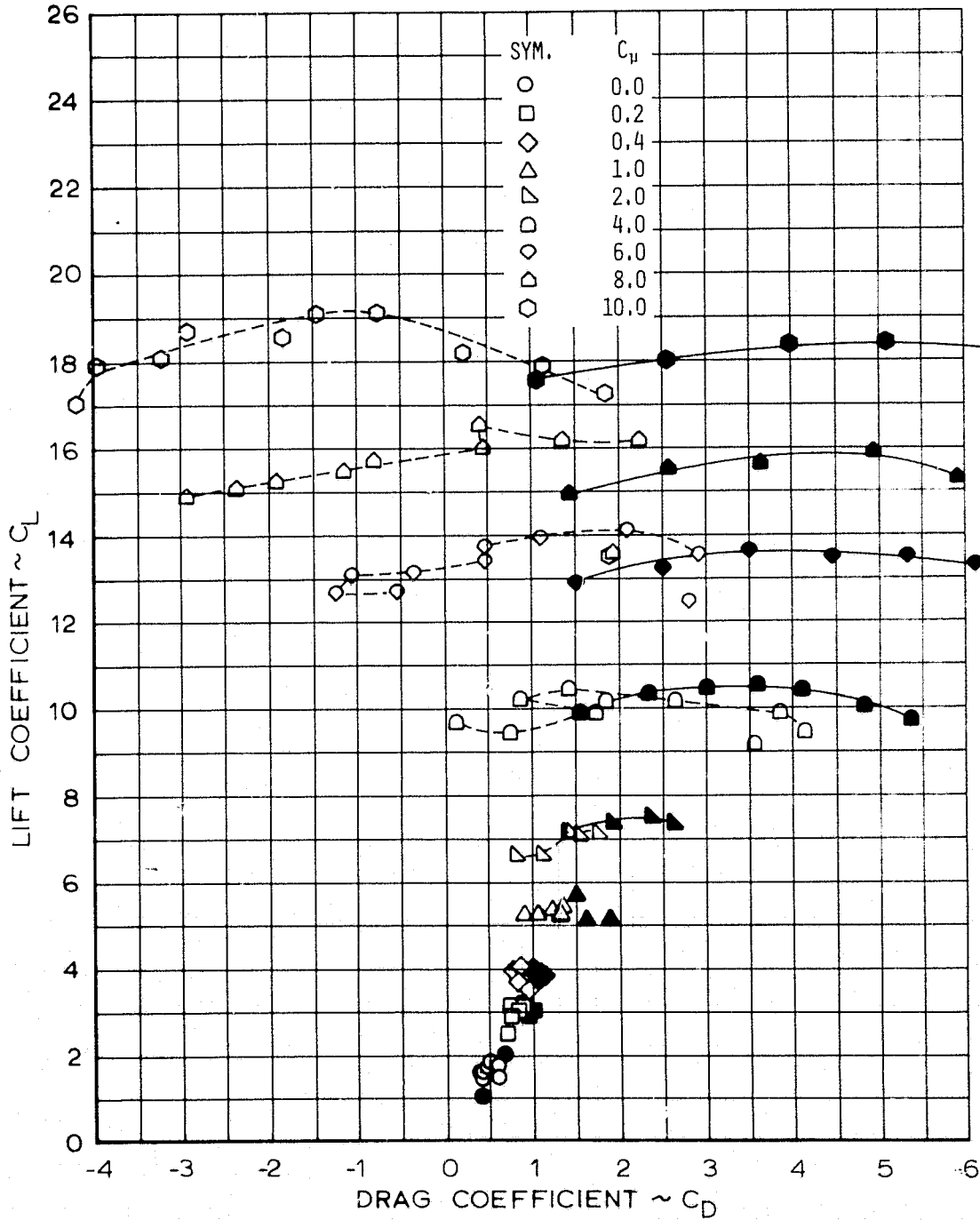


FIGURE 5.3(b) BASIC DRAG DATA

CONFIGURATION: BASIC WING, SLATS REMOVED (F)
 MODEL ON TUNNEL CENTERLINE

- NASA/AAMRDL 7x10 FOOT WIND TUNNEL ~ NO CORRECTIONS
- LOCKHEED 30x42 INCH WIND TUNNEL ~ CORRECTED FOR BLOCKAGE AND WALL EFFECTS

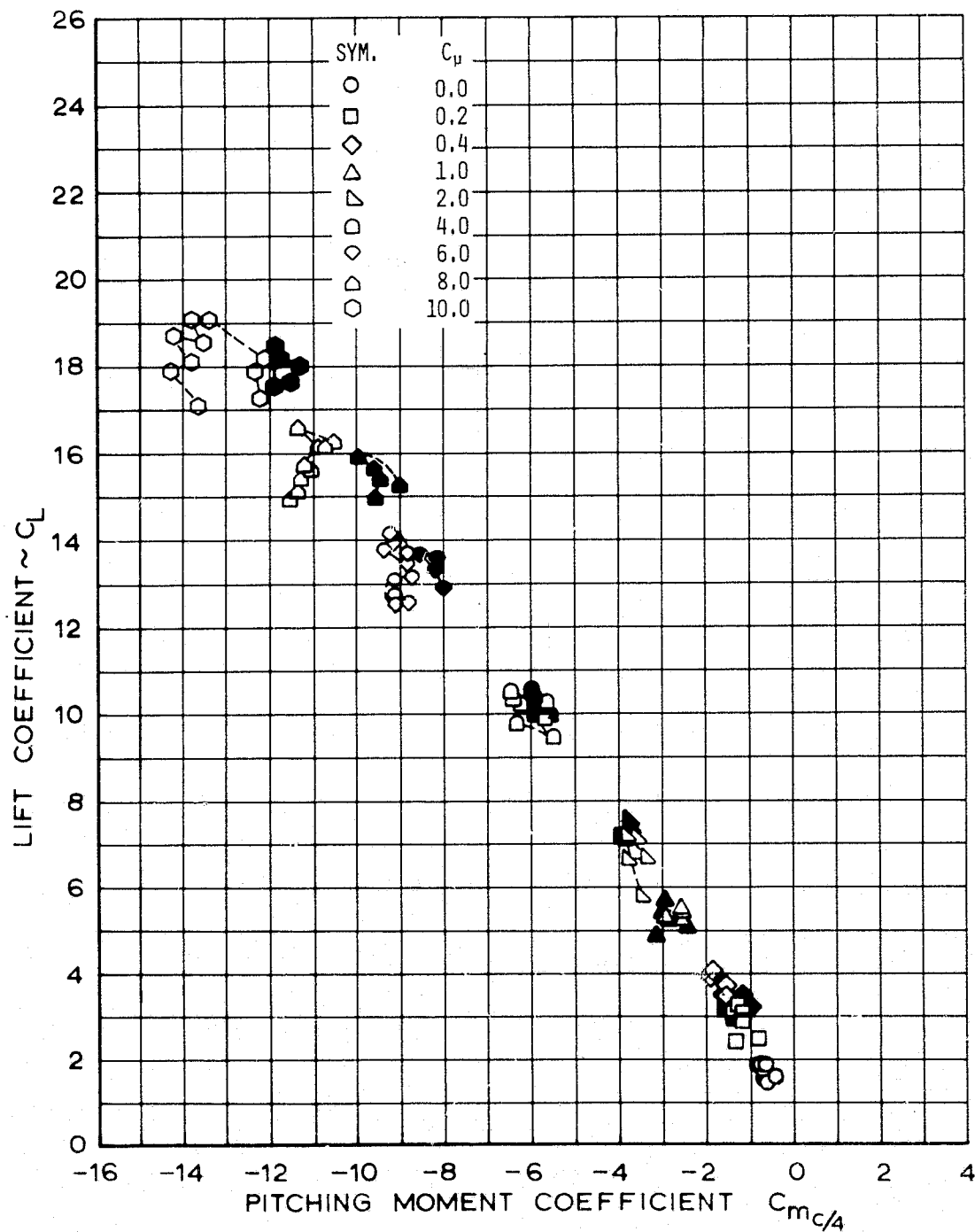


FIGURE 53(c) BASIC PITCHING MOMENT DATA

CONFIGURATION: WITH TIPS, FULL SLATS (B)
 MODEL ON TUNNEL CENTERLINE

- NASA/AAMRDL 7x10 FOOT WIND TUNNEL ~ NO CORRECTIONS
- LOCKHEED 30x42 INCH WIND TUNNEL ~ CORRECTED FOR BLOCKAGE AND WALL EFFECTS

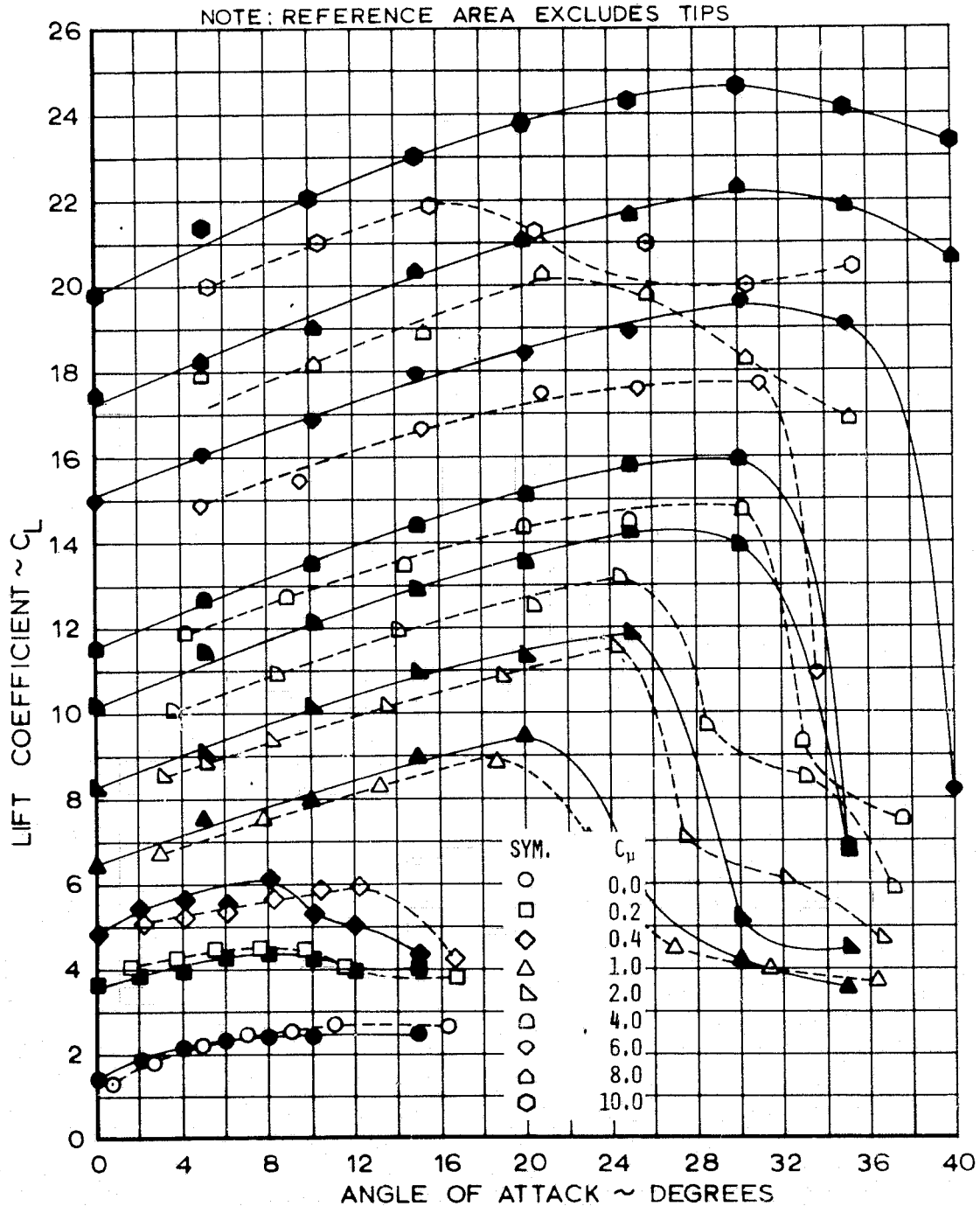


FIGURE 5.4(a) BASIC LIFT DATA

CONFIGURATION: WITH TIPS, FULL SLATS (B)
 MODEL ON TUNNEL CENTERLINE

- NASA/AAMRDL 7x10 FOOT WIND TUNNEL ~ NO CORRECTIONS
- LOCKHEED 30x42 INCH WIND TUNNEL ~ CORRECTED FOR BLOCKAGE AND WALL EFFECTS

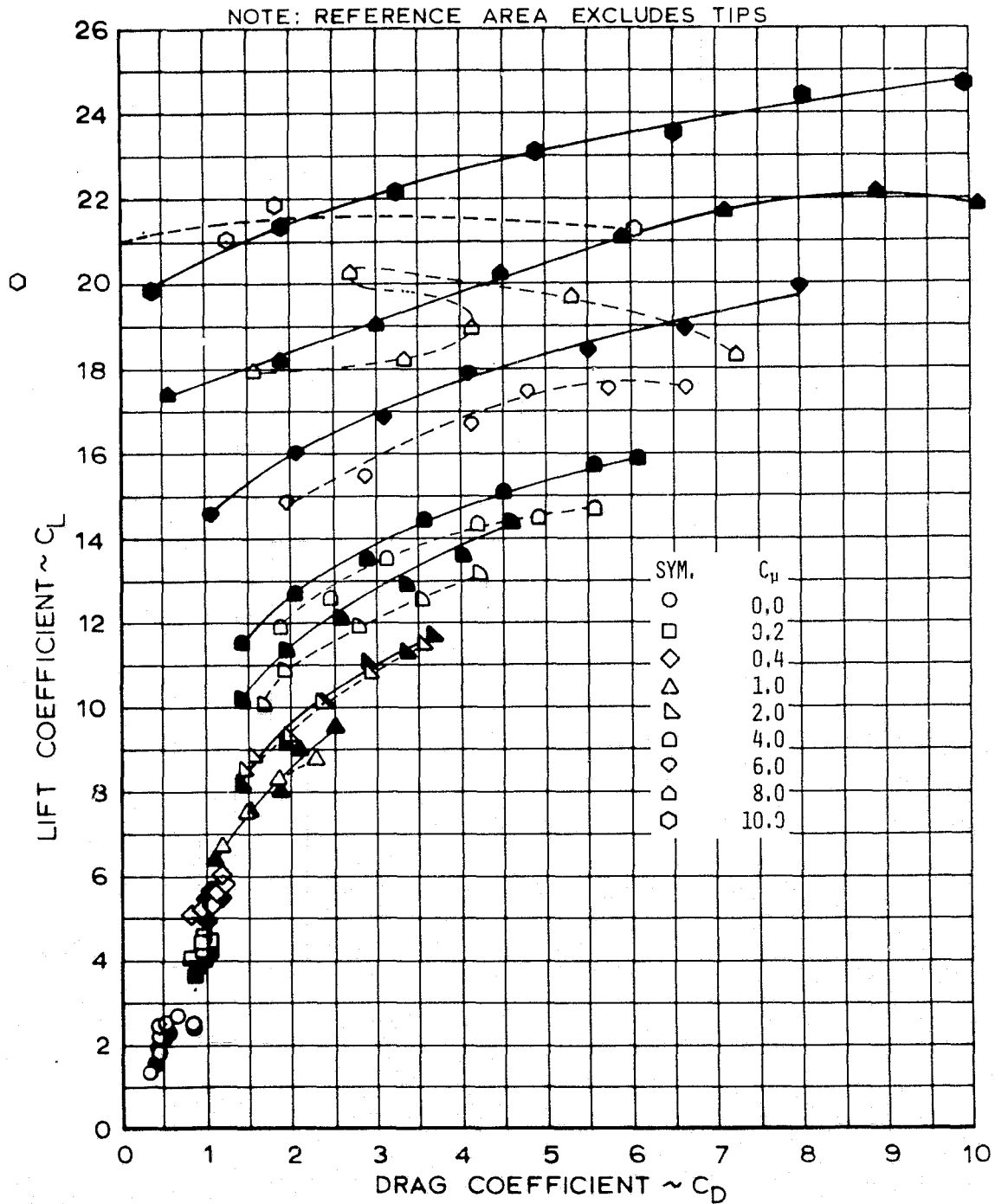


FIGURE 5.4(b) BASIC DRAG DATA

CONFIGURATION: WITH TIPS, FULL SLATS (B)
 MODEL ON TUNNEL CENTERLINE

- NASA/AAMRDL 7x10 FOOT WIND TUNNEL ~ NO CORRECTIONS
- LOCKHEED 30x42 INCH WIND TUNNEL ~ CORRECTED FOR BLOCKAGE AND WALL EFFECTS

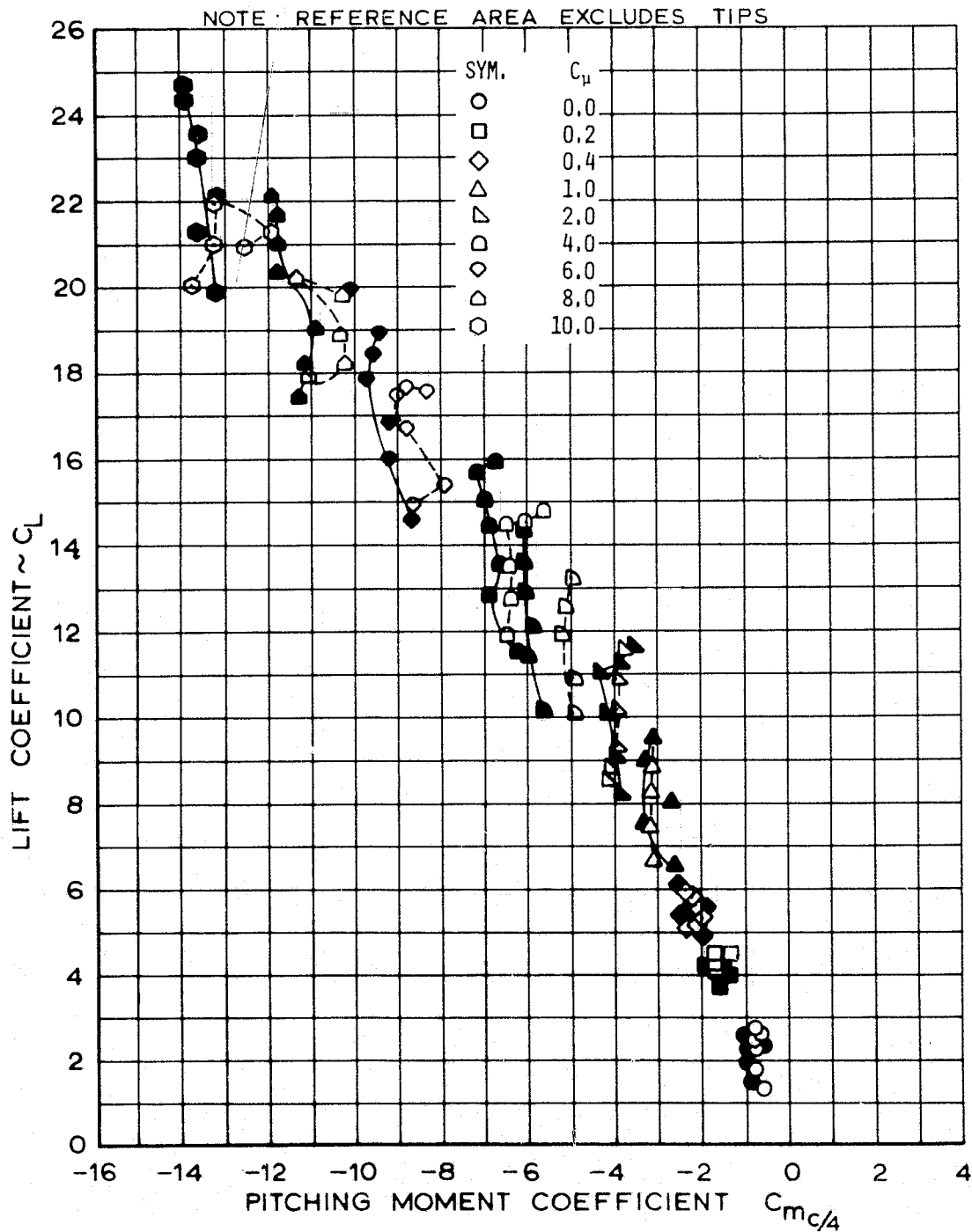


FIGURE 54(c) BASIC PITCHING MOMENT DATA

CONFIGURATION: WITH TIPS, OUTER SLATS REMOVED(G)
 MODEL ON TUNNEL CENTERLINE

- NASA/AAMRDL 7x10 FOOT WIND TUNNEL ~ NO CORRECTIONS
- LOCKHEED 30x42 INCH WIND TUNNEL ~ CORRECTED FOR BLOCKAGE AND WALL EFFECTS

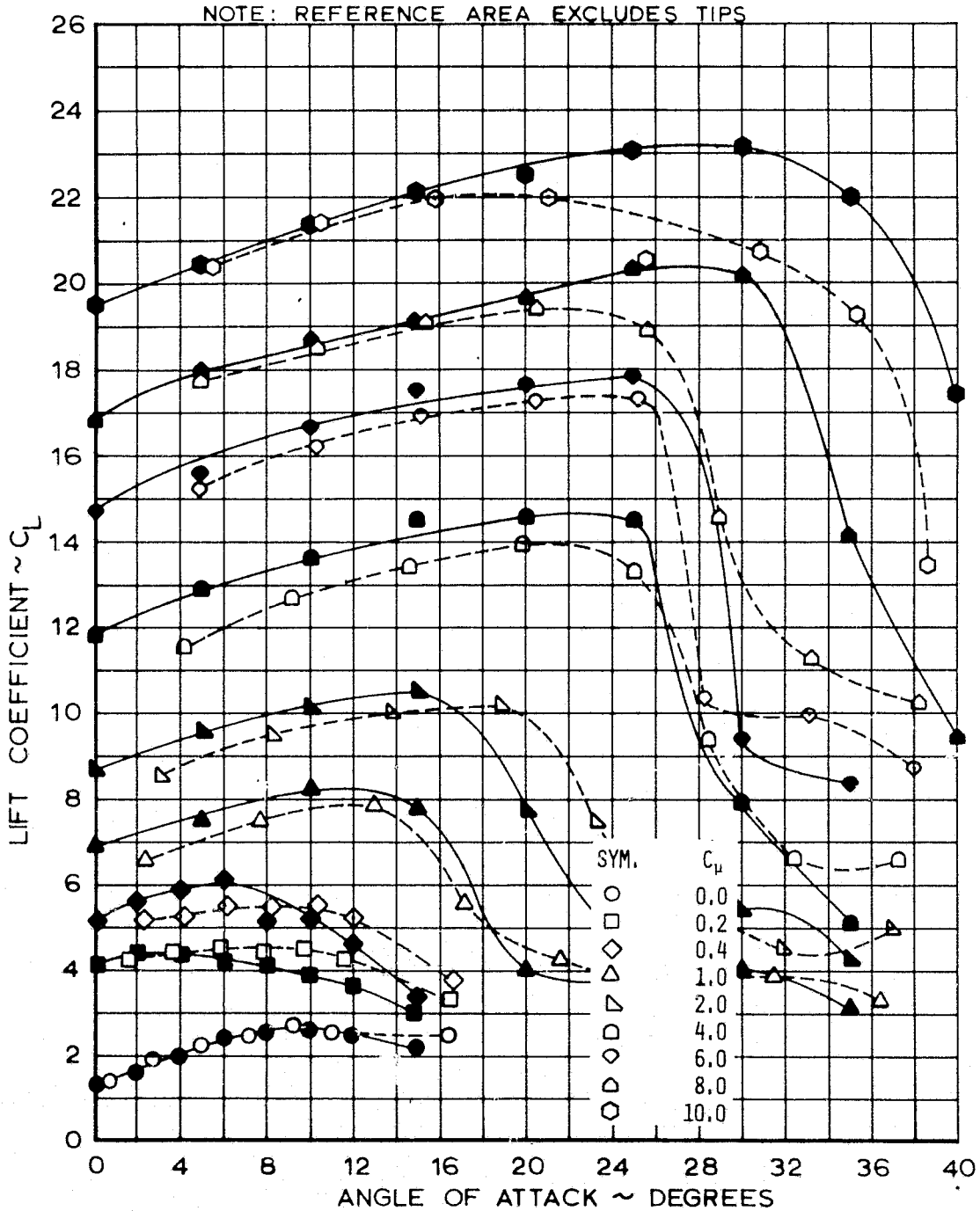


FIGURE 5.5(a) BASIC LIFT DATA

CONFIGURATION: WITH TIPS, OUTER SLATS REMOVED (G)
 MODEL ON TUNNEL CENTERLINE

- NASA/AAMRDL 7x10 FOOT WIND TUNNEL ~ NO CORRECTIONS
- LOCKHEED 30x42 INCH WIND TUNNEL ~ CORRECTED FOR BLOCKAGE AND WALL EFFECTS

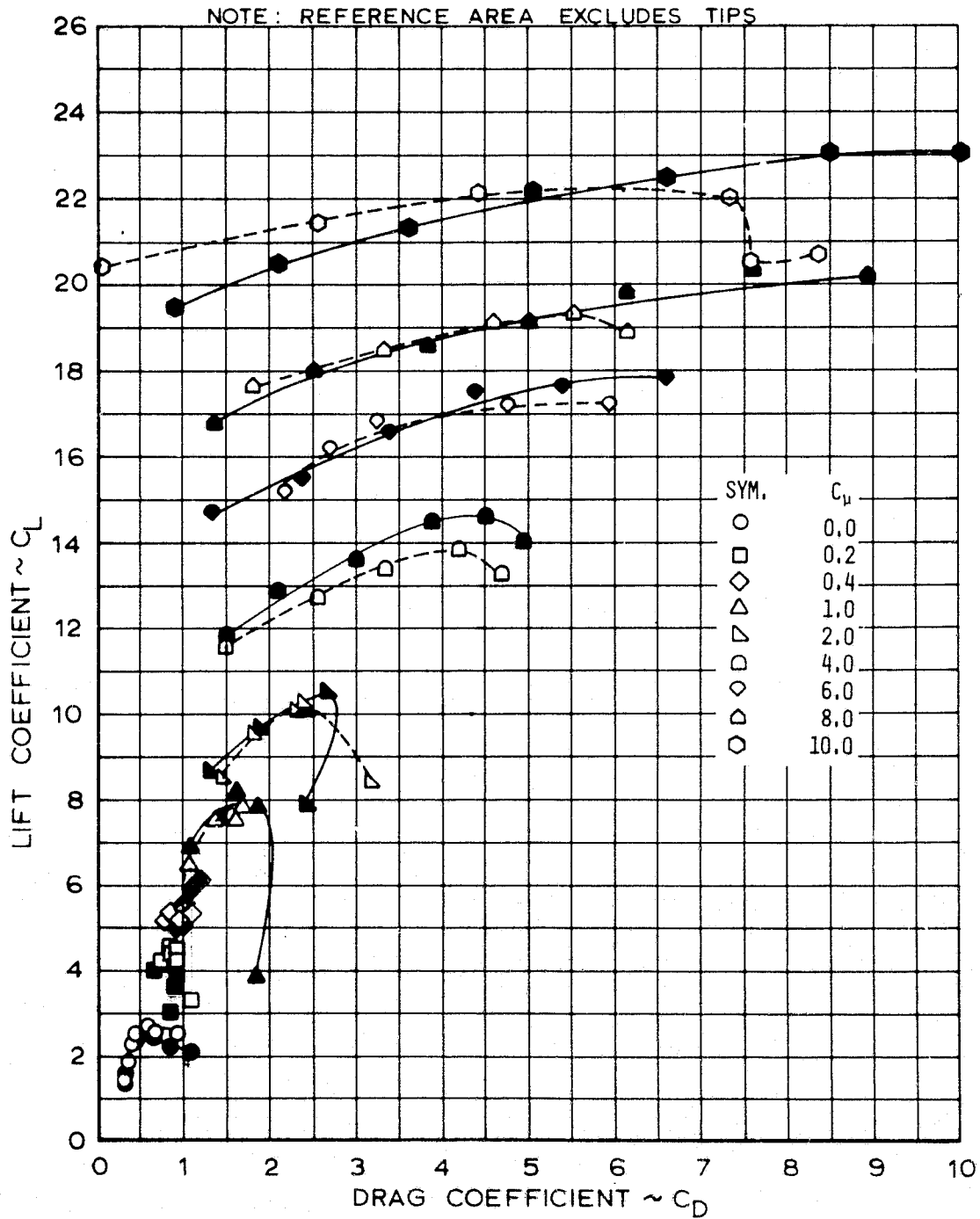


FIGURE 5.5(b) BASIC DRAG DATA

CONFIGURATION: WITH TIPS, OUTER SLATS REMOVED (G)
 MODEL ON TUNNEL CENTERLINE

- NASA/AAMRDL 7x10 FOOT WIND TUNNEL ~ NO CORRECTIONS
- LOCKHEED 30x42 INCH WIND TUNNEL ~ CORRECTED FOR BLOCKAGE AND WALL EFFECTS

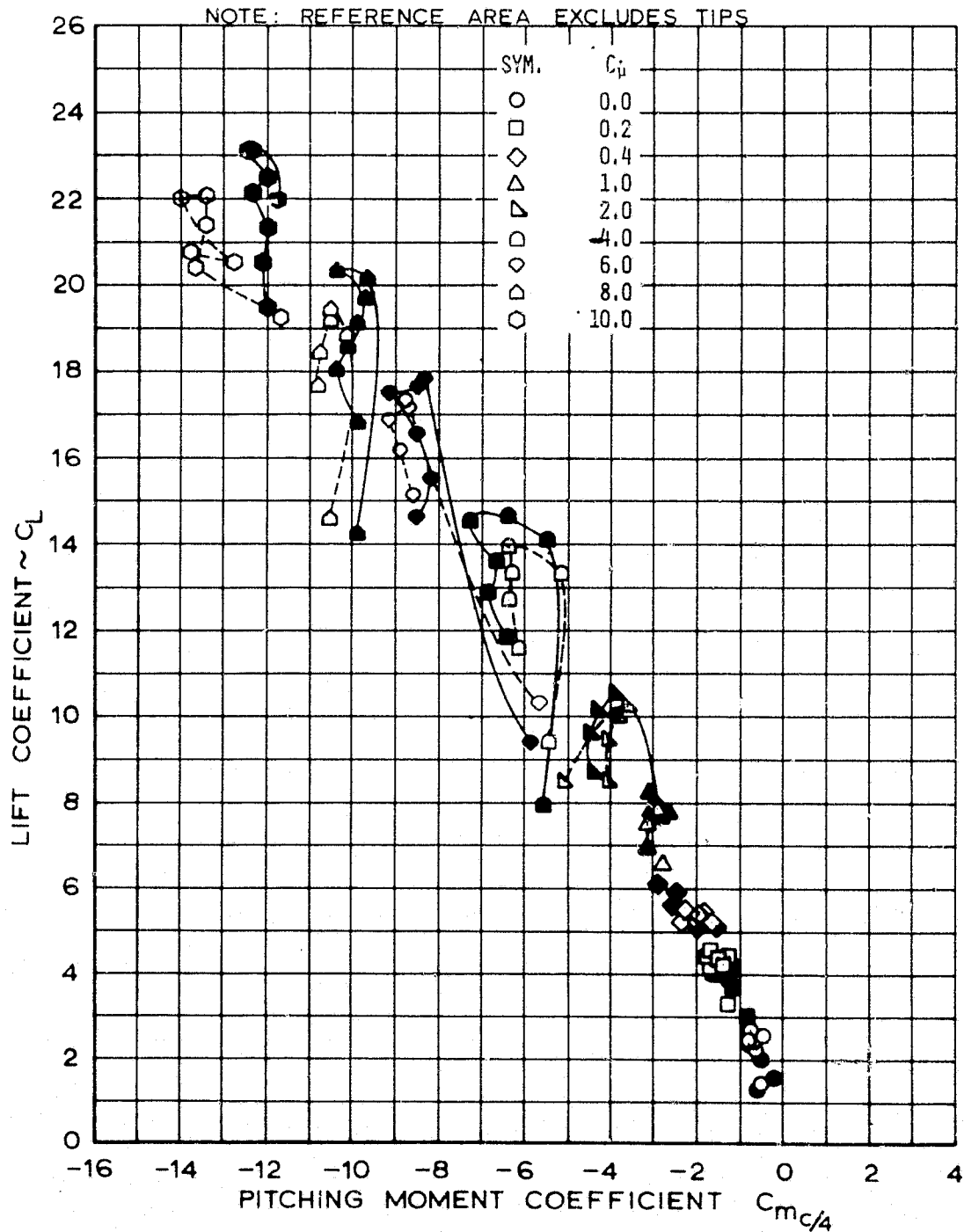


FIGURE 5.5(c) BASIC PITCHING MOMENT DATA

CONFIGURATION: WITH TIPS, INNER SLATS REMOVED (E)
 MODEL ON TUNNEL CENTERLINE

- NASA/AAMRDL 7x10 FOOT WIND TUNNEL ~ NO CORRECTIONS
- LOCKHEED 30x42 INCH WIND TUNNEL ~ CORRECTED FOR BLOCKAGE AND WALL EFFECTS

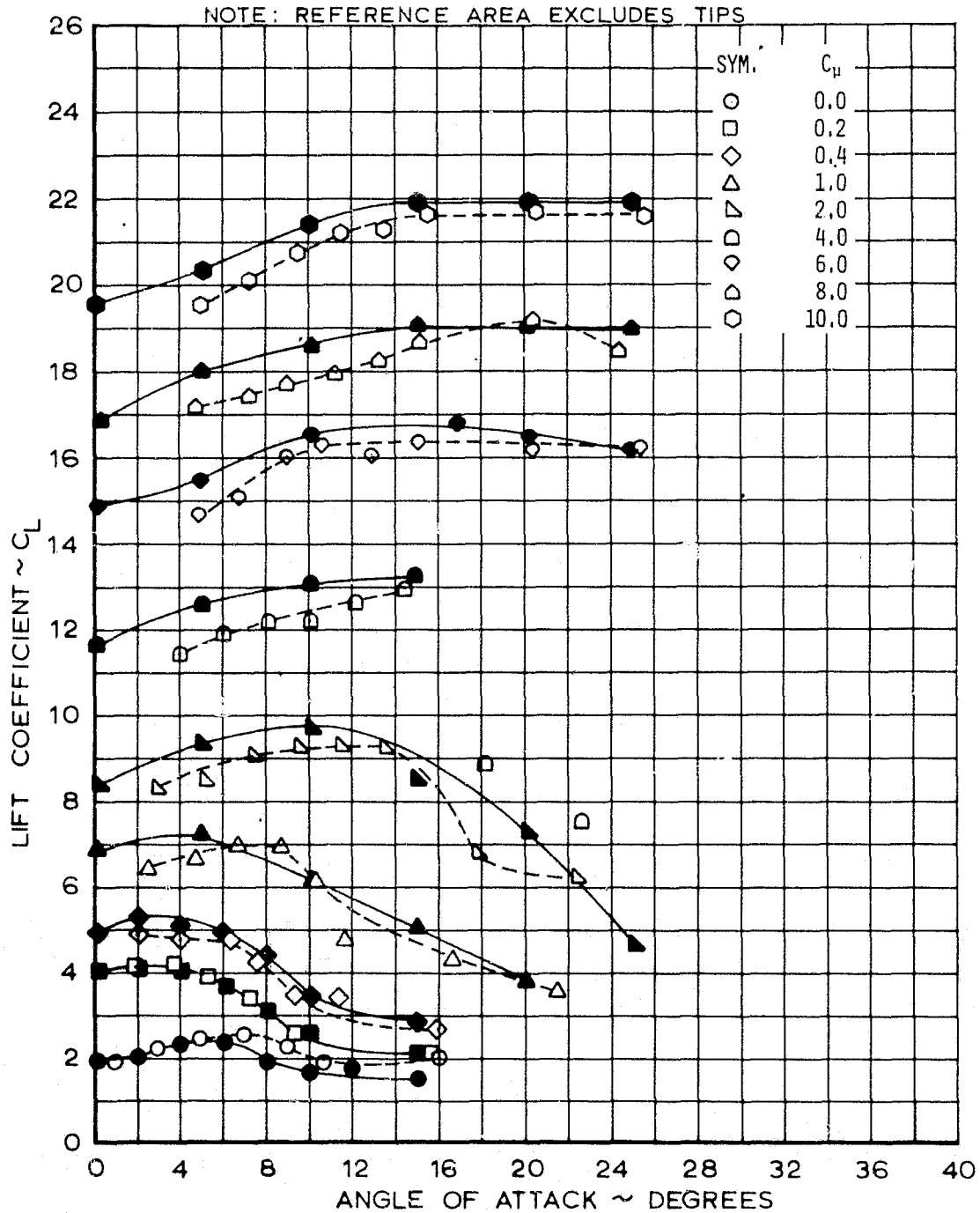


FIGURE 5.6(a) BASIC LIFT DATA

CONFIGURATION: WITH TIPS, INNER SLATS REMOVED (E)
 MODEL ON TUNNEL CENTERLINE

- NASA/AAMRDL 7x10 FOOT WIND TUNNEL ~ NO CORRECTIONS
- LOCKHEED 30x42 INCH WIND TUNNEL ~ CORRECTED FOR BLOCKAGE AND WALL EFFECTS

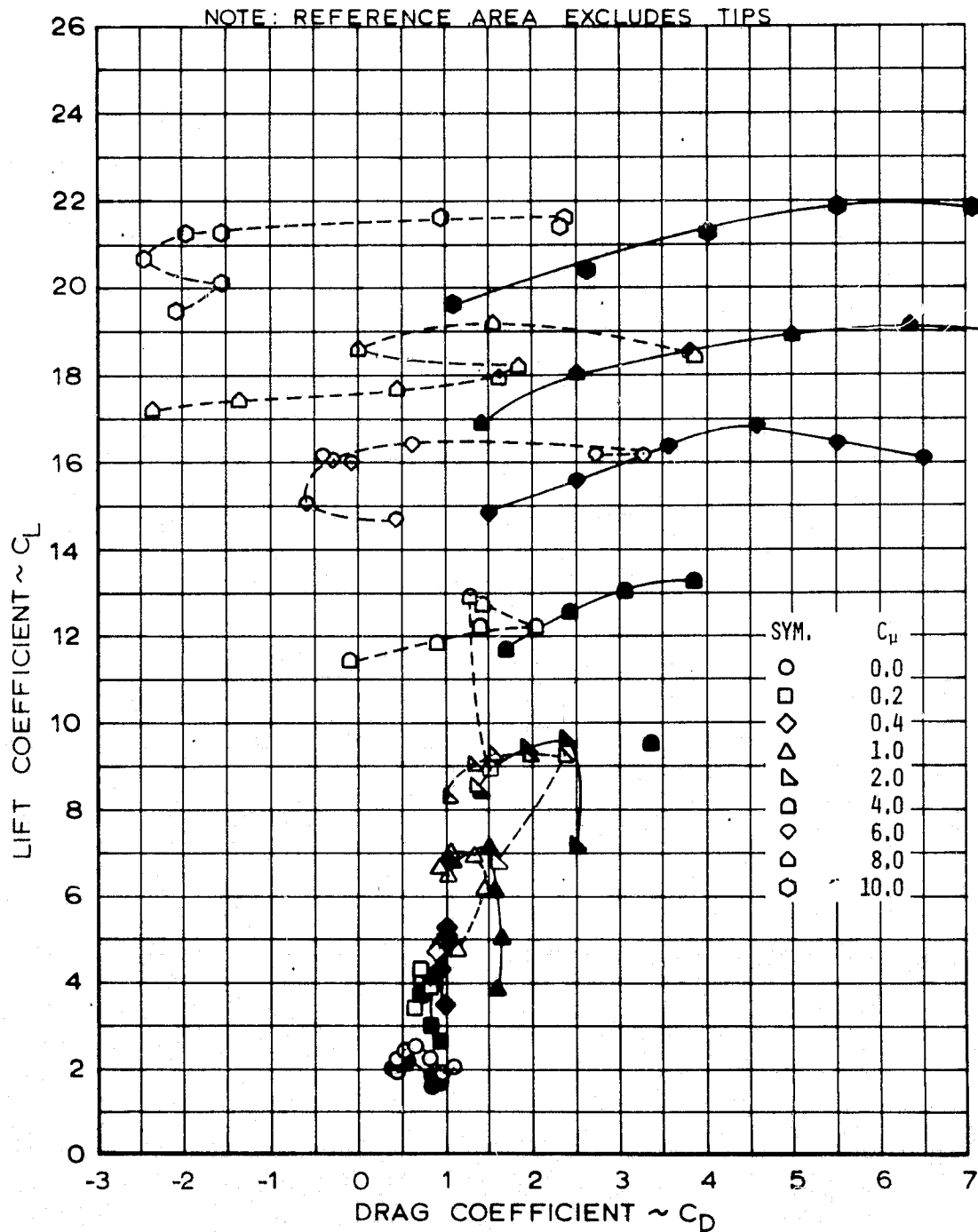


FIGURE 5.6(b) BASIC DRAG DATA

CONFIGURATION: WITH TIPS, INNER SLATS REMOVED (E)
 MODEL ON TUNNEL CENTERLINE

- NASA/AAMRDL 7x10 FOOT WIND TUNNEL ~ NO CORRECTIONS
- LOCKHEED 30x42 INCH WIND TUNNEL ~ CORRECTED FOR BLOCKAGE AND WALL EFFECTS

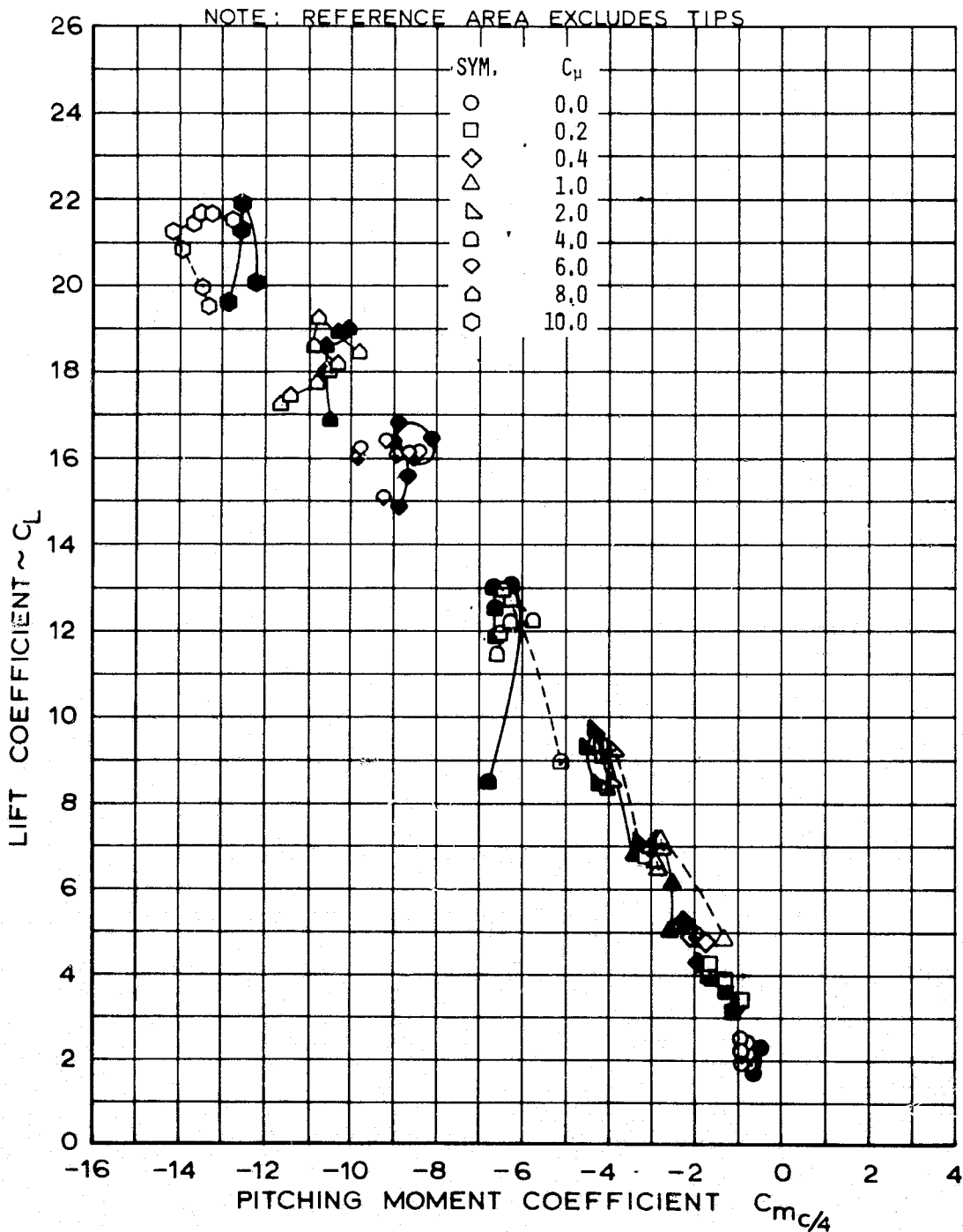


FIGURE 5.6(c) BASIC PITCHING MOMENT DATA

BASIC CONFIGURATION

◇ LOCKHEED 30" x 42" $i_H = 0^\circ$ ◆ NASA/AAMRDL 7' x 10' $i_H = 20^\circ$

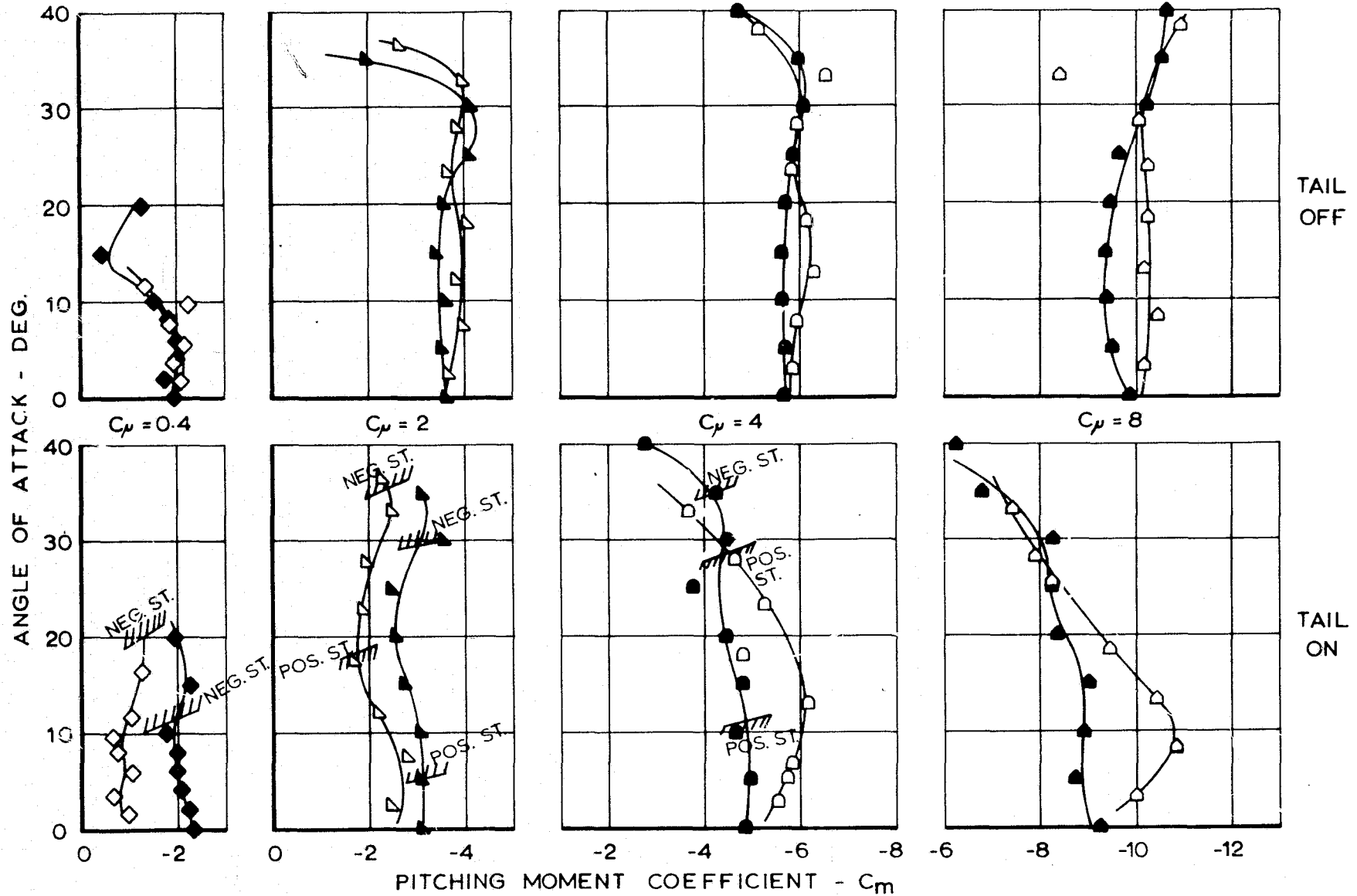


FIGURE 5.7 TAIL-ON AND TAIL-OFF PITCHING MOMENTS, BASIC CONFIGURATIONS (A-1, A-2)

CONFIGURATION WITH TIPS

◇ LOCKHEED 30" x 42" $i_H = 0^\circ$ ◆ NASA / AAMRDL 7' x 10' $i_H = 20^\circ$

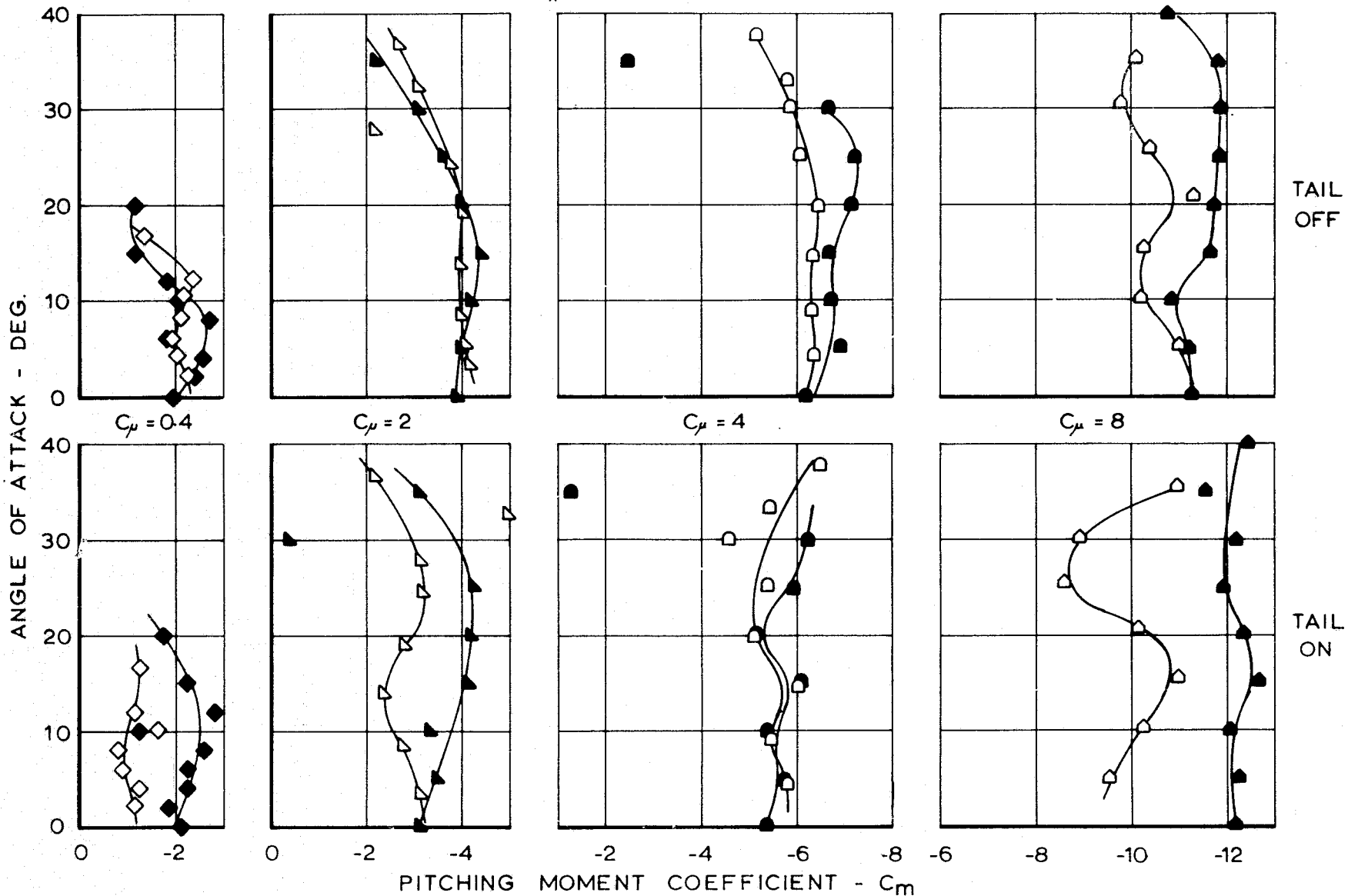


FIGURE 5.8 TAIL-ON AND TAIL-OFF PITCHING MOMENTS, WITH TIPS (B,C)

	LIFT	DRAG	PITCHING MOMENT		
UNPOWERED $1 < C_L < 2$	GOOD CORRELATION	SOMEWHAT HIGHER IN SMALL TUNNEL	REASONABLE CORRELATION	SLAT ON	A1
	STALL EARLIER IN SMALL TUNNEL, OTHERWISE GOOD CORRELATION	REASONABLE CORRELATION	GOOD CORRELATION	SLAT OFF	F
FLAP 'BLC' $C_{\mu} = 0.2$ $3 < C_L < 4$	SMALL TUNNEL BLC YIELDS BETTER LIFT CURVE SLOPE CORRELATION	REASONABLE CORRELATION	GOOD CORRELATION	SLAT ON	A1
	GOOD CORRELATION	SMALL TUNNEL SLIGHTLY LOW	GOOD CORRELATION	SLAT OFF	G
$3 \leq C_L \leq 10$	GOOD CORRELATION	GOOD CORRELATION	SOME DIFFERENCES BUT GENERALLY REASONABLE	SLAT ON	A1
	REASONABLE CORRELATION, SMALL TUNNEL SLIGHTLY LOW, STALL O.K.	POOR CORRELATION. DRAG SUCCESSIVELY LOWER AS C_{μ} INCREASES IN SMALL TUNNEL.	SOME DIFFERENCES BUT GENERALLY REASONABLE	SLAT OFF	F
$C_L < 10$	GOOD CORRELATION EXCEPT FOR PROGRESSIVELY EARLIER SMALL TUNNEL STALL AT $C_{\mu} = 6, 8, 10$.	GOOD CORRELATION EXCEPT IN PREMATURE STALL. DRAG DROPS WHEN STALL OCCURS.	PITCH-DOWN IN SMALLER TUNNEL AT HIGHER C_{μ} 's. INCREASING POST-STALL DIFFERENCES.	SLAT ON	A1
	TENDENCY TO "HUMP" IN $C_L \sim \alpha$ CURVES, BUT ERRORS MODERATE.	POOR CORRELATION, DRAG POLARS MOVED ABOUT 0.6 C_{μ} TO LEFT (THRUST).	INCREASING PITCH-DOWN IN SMALL TUNNEL	SLAT OFF	F

FIGURE 5.9 SUMMARY OF SMALL/LARGE-TUNNEL COMPARISONS FOR BASIC CONFIGURATIONS.

	LIFT	DRAG	PITCHING MOMENT		
UNPOWERED $C_L = 1$ ($1 < C_L < 3$)*	GOOD CORRELATION	GOOD CORRELATION	REASONABLE AGREEMENT	SLATS ON	B
	EXCELLENT CORRELATION	GOOD CORRELATION		OUTER REMOVED	G
	GOOD CORRELATION. STALL SLIGHTLY EARLIER IN LARGE TUNNEL	REFLECTS DIFFERENCES IN STALL		INNER REMOVED	E
FLAP 'BLC' $C_{\mu} = 0.106$ (0.20) $C_L = 2$ ($2 < C_L < 4$)	GOOD CORRELATION	REASONABLE AGREEMENT	REASONABLE AGREEMENT	SLATS ON	B
	GOOD LOW α CORRELATION. LARGE TUNNEL EARLY STALL.			OUTER REMOVED	G
	REASONABLE CORRELATION, STALL AGREES.			INNER REMOVED	E
$2 < C_L < 8$ ($4 < C_L < 15$)	SMALL TUNNEL ABOUT 5% LOW. GOOD STALL AGREEMENT.	REFLECTS LOWER C_L 's, OTHERWISE GOOD AGREEMENT	AGREEMENT FAIR, REFLECTS LIFT DEFICIT IN SMALLER TUNNEL	SLATS ON	B
	SMALL TUNNEL ABOUT 5% LOW. GOOD STALL AGREEMENT.			INNER REMOVED	G
	FAIR AGREEMENT. SCATTER IN SMALL TUNNEL RESULTS	REASONABLE AGREEMENT UP TO $C_L = 5$. POOR CORRELATION BEYOND THIS. DRAG CURVES SHIFTED BY $0.6 C_{\mu}$.		OUTER REMOVED	E
$C_L > 8$ ($C_L > 15$)	SMALL TUNNEL ABOUT 5% LOW. PROGRESSIVELY EARLIER STALL WITH INCREASING C_{μ} .	POOR CORRELATION UNDER STALLED CONDITIONS. STRONG LEFTWARD SHIFT OF POLARS.	REFLECTS EARLY STALL IN SMALLER TUNNEL	SLATS ON	B
	SMALL TUNNEL GENERALLY LARGER, SHOWS MORE SCATTER.	POOR CORRELATION. DRAG POLARS MOVED ABOUT 0.6 C_{μ} TO LEFT	PITCH-DOWN IN SMALLER TUNNEL	INNER REMOVED	G
	GOOD AGREEMENT EXCEPT FOR EARLIER STALL AT HIGHER C_{μ} 's.	REASONABLE AGREEMENT EXCEPT AT HIGHEST BLOWING RATE		OUTER REMOVED	E

*Parentheses refer to no-tips reference area.

FIGURE 5.10 SUMMARY OF SMALL/LARGE-TUNNEL COMPARISONS FOR TIPPED CONFIGURATIONS.

STATIC PRESSURE COEFFICIENT AT WALL MID-HEIGHT

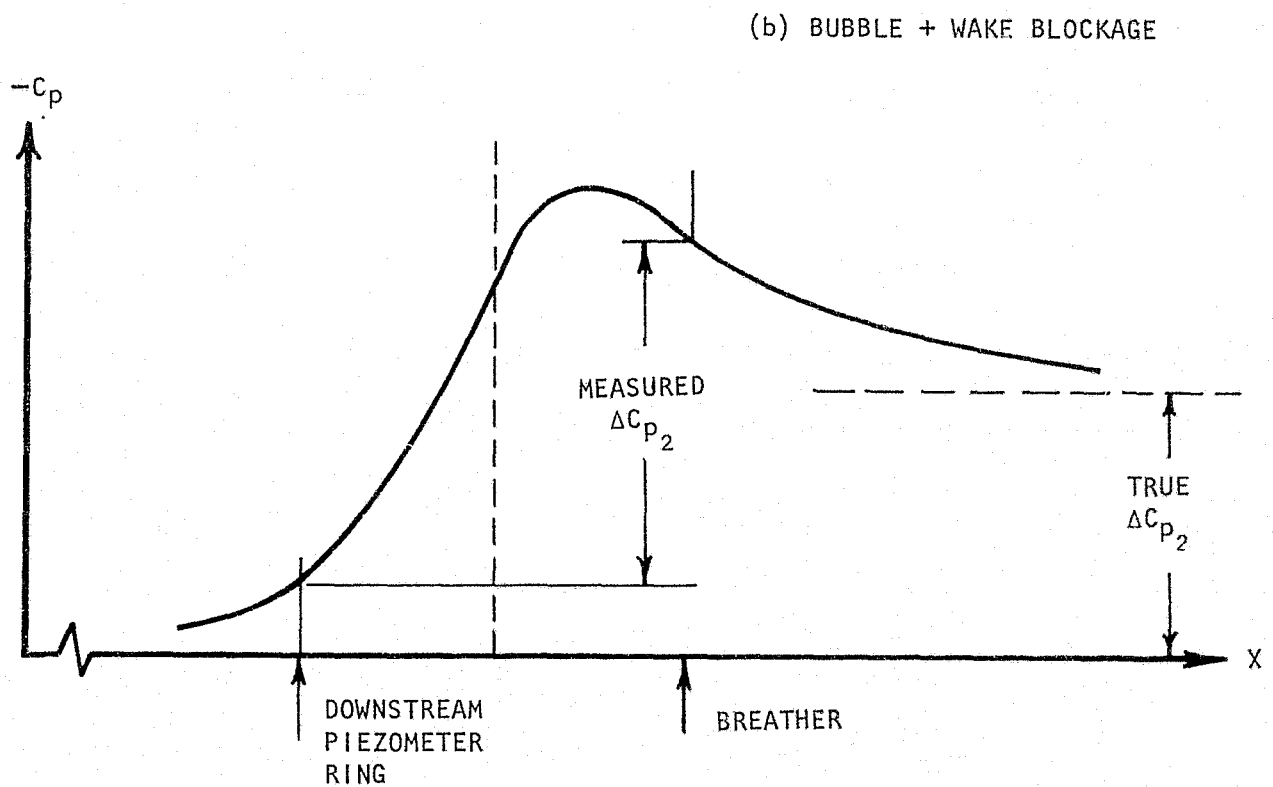
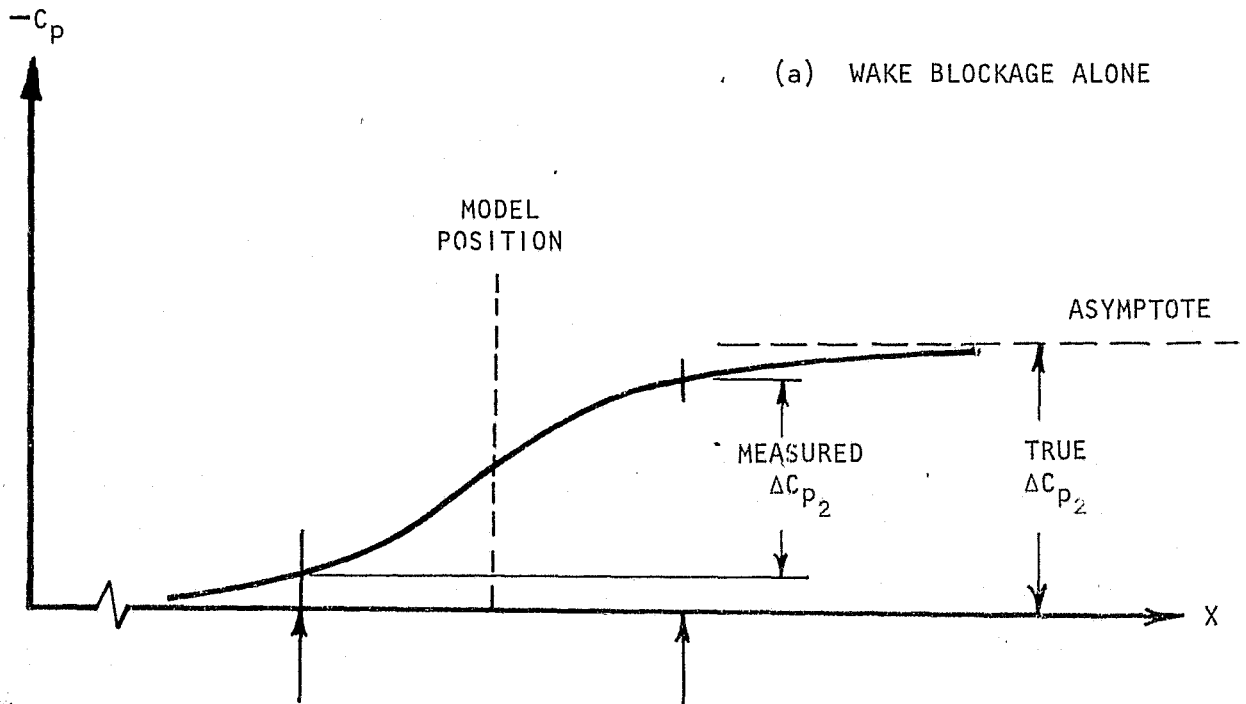
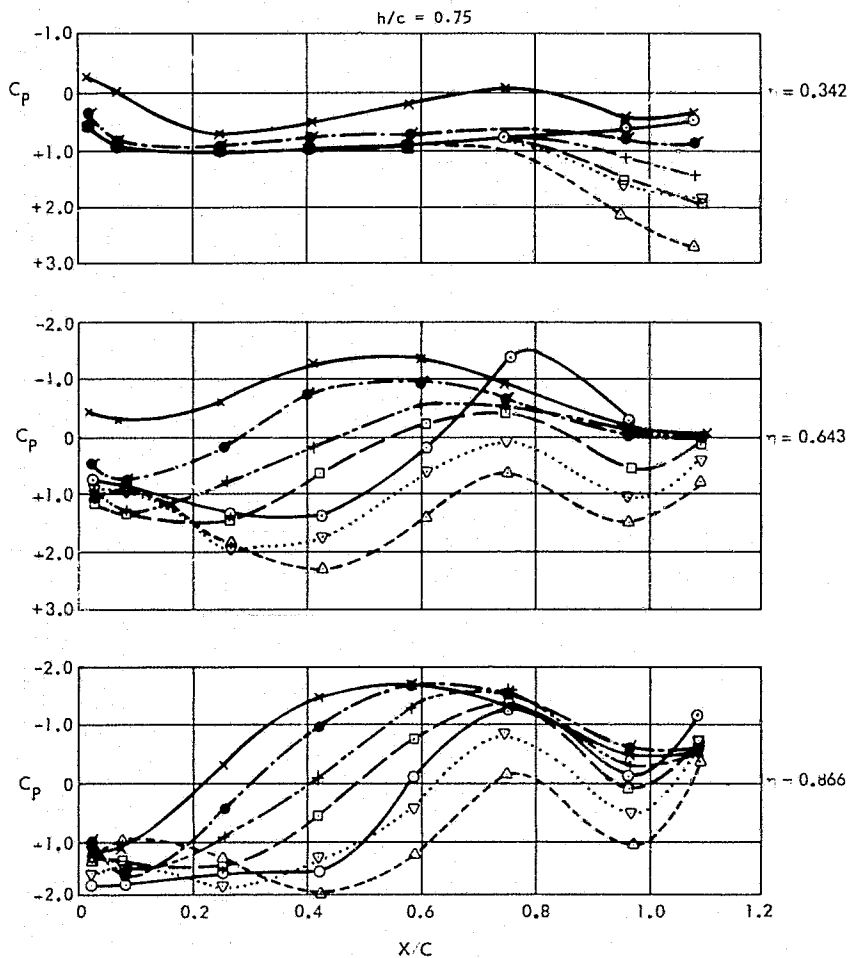
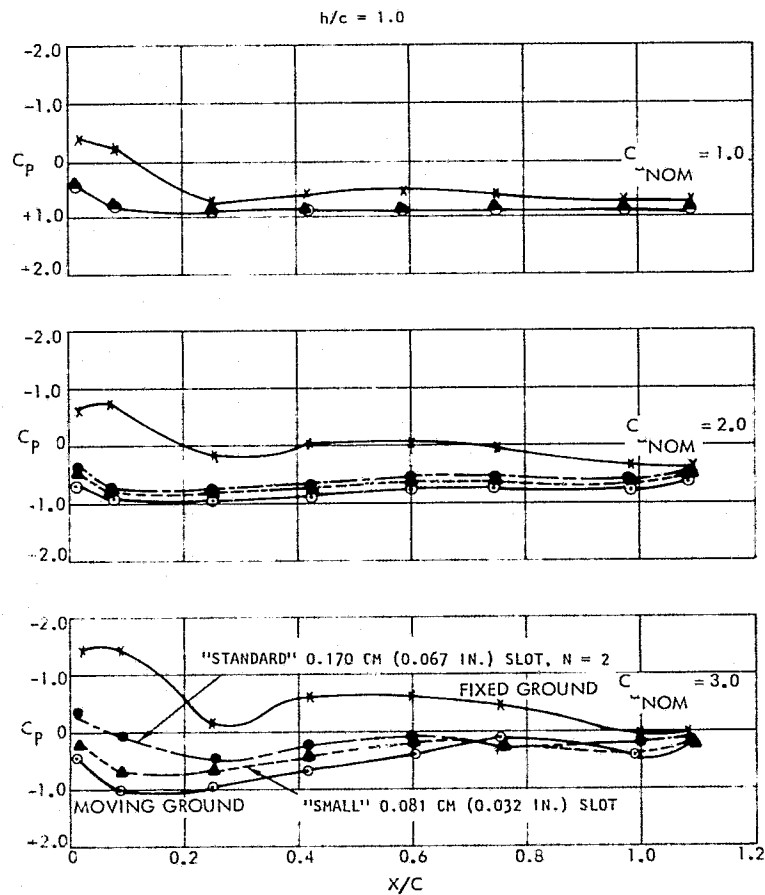


FIGURE 5.11 EFFECT OF SOLID BLOCKAGE ON WAKE BLOCKAGE CORRECTIONS.

SYMBOL	x	o	•	+	□	▽	△	▲
N	FIXED GROUND	MOVING GROUND	2.0	2.5	3.0	3.5	4.0	2.0
BLC SLOT HEIGHT			0.170 (0.067)	0.170 (0.067)	0.170 (0.067)	0.170 (0.067)	0.170 (0.067)	0.081 (0.032)



(a) EFFECT OF BLOWING BLC, AT THE GROUND,
ON WING LOWER SURFACE PRESSURES:
 $C_{L,NOM} = 3.0$



(b) EFFECT OF SLOT SIZE ON PERFORMANCE OF
GROUND BLC SYSTEM, $\tau = 0.643$

FIGURE 6.1 GROUND EFFECT ON UNDERSURFACE PRESSURES

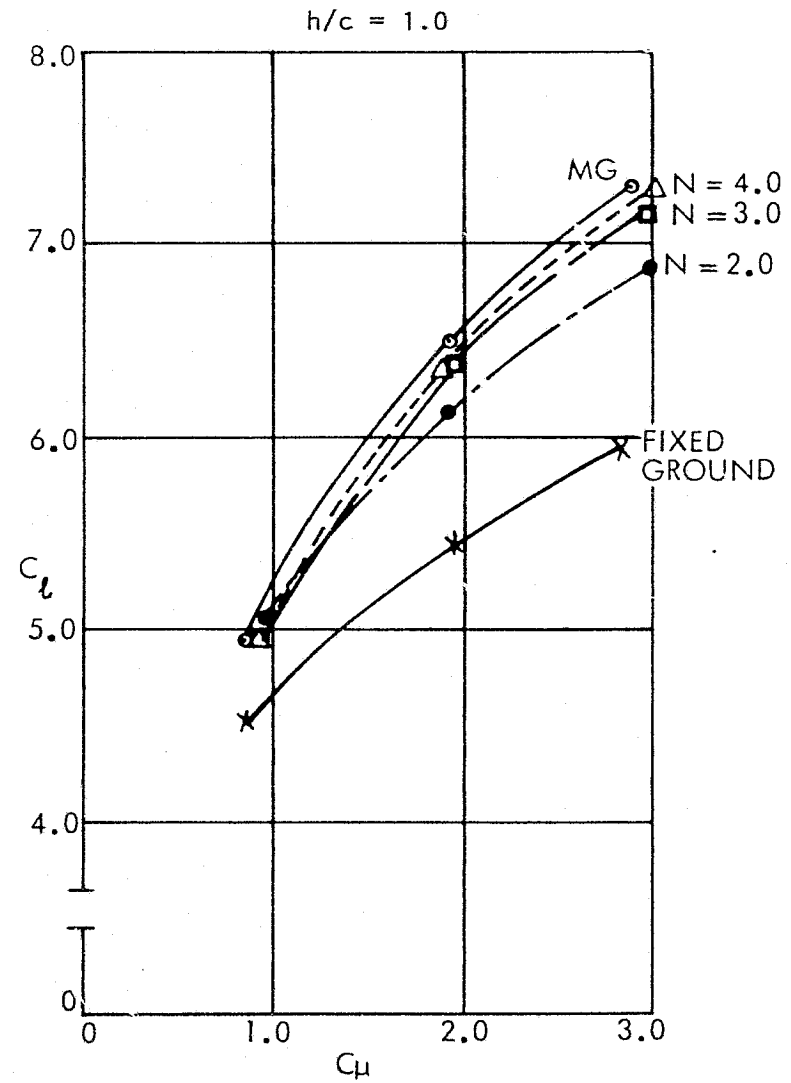
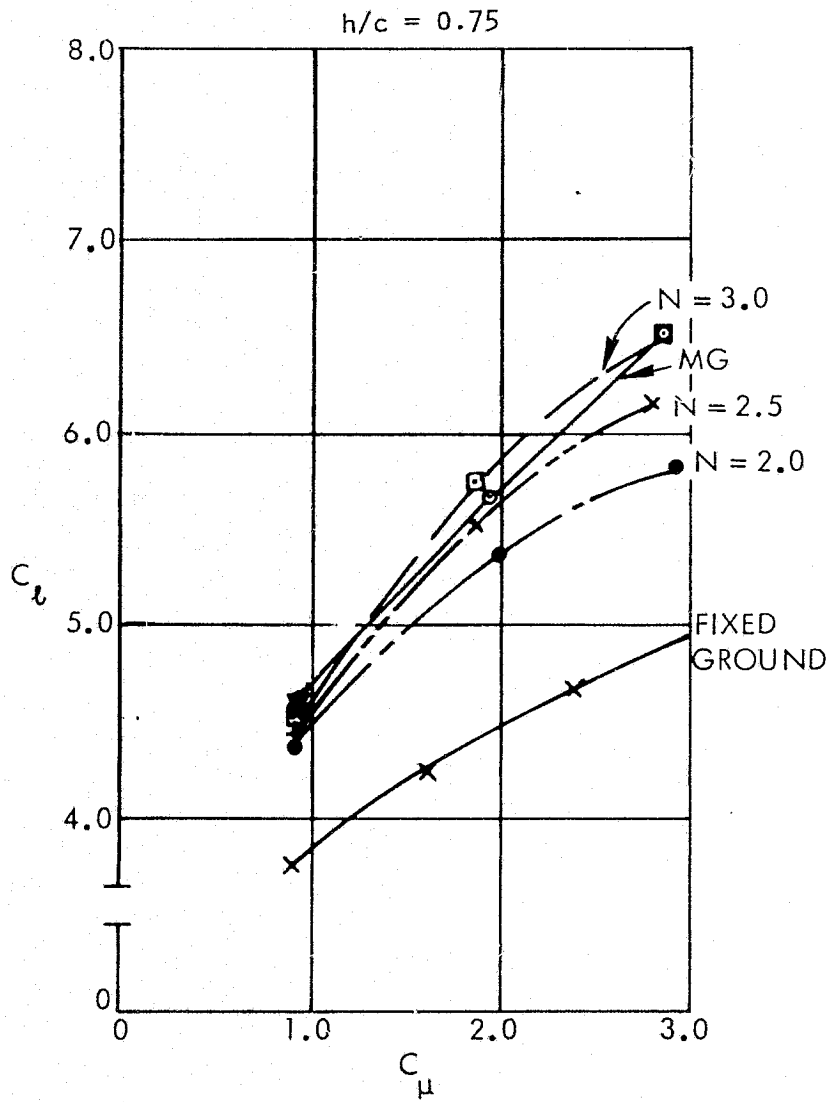


FIGURE 6.2 EFFECT OF GROUND BLC ON SECTIONAL LIFT COEFFICIENT, $\eta = 0.643$

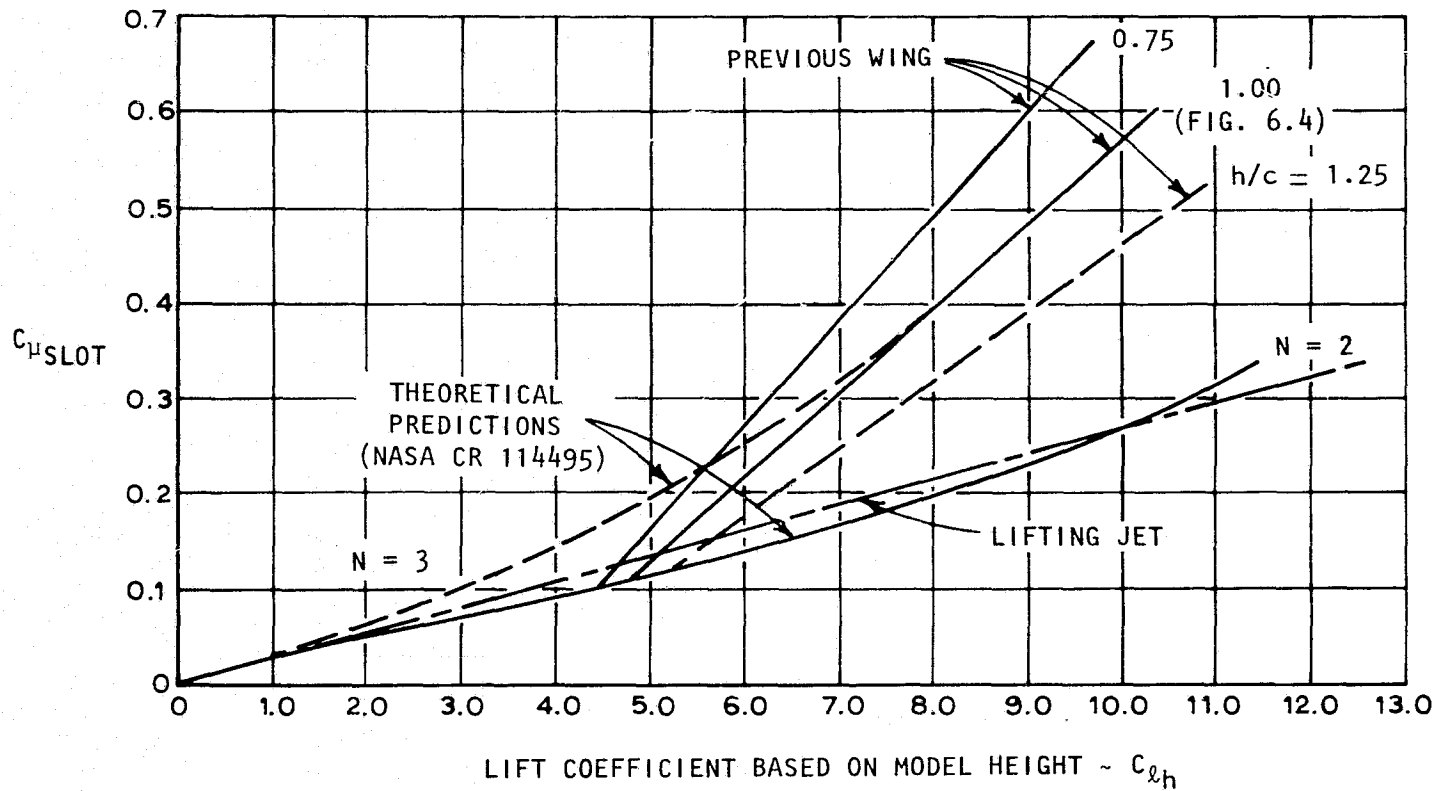


FIGURE 6.3 FLOOR TANGENTIAL - BLOWING REQUIREMENTS DERIVED VIA SURFACE PRESSURE INVESTIGATIONS (ADAPTED FROM NASA CR 114496, FIGURE 42).

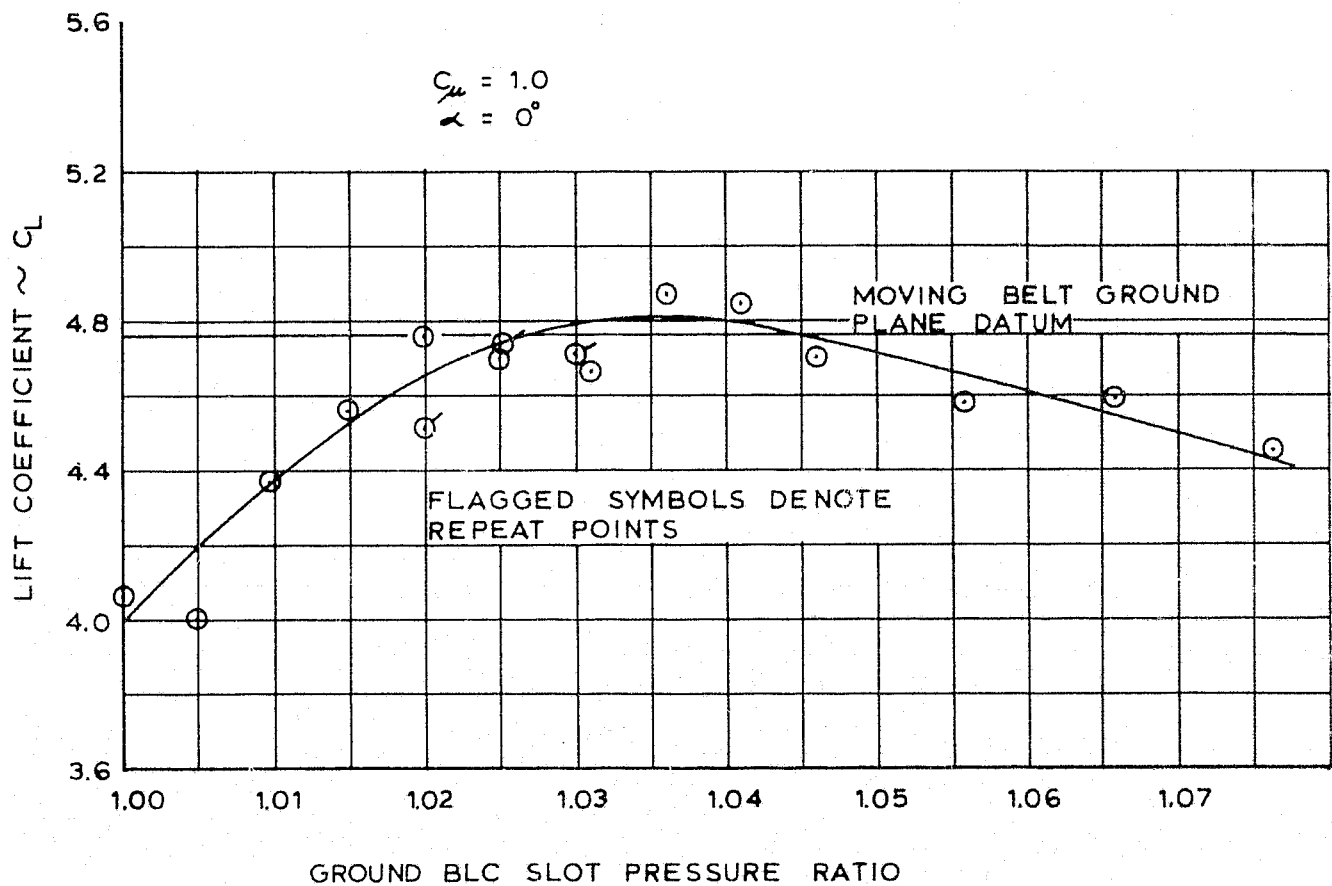
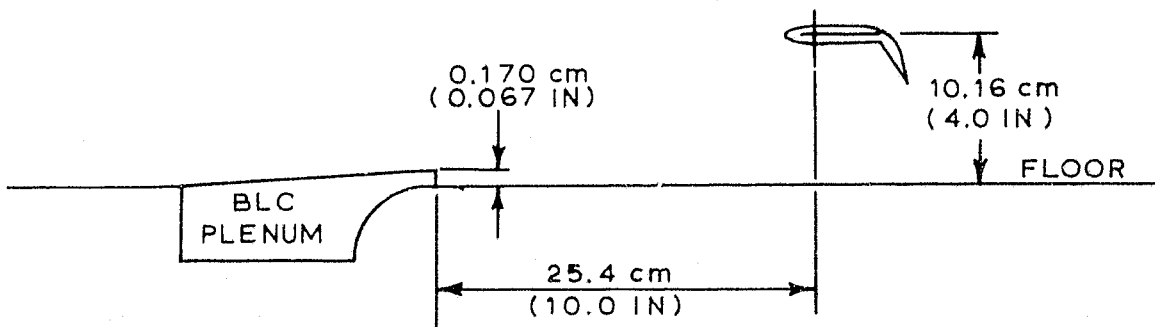


FIGURE 6.4 TYPICAL MOVING AND BLC GROUND TEST RESULTS

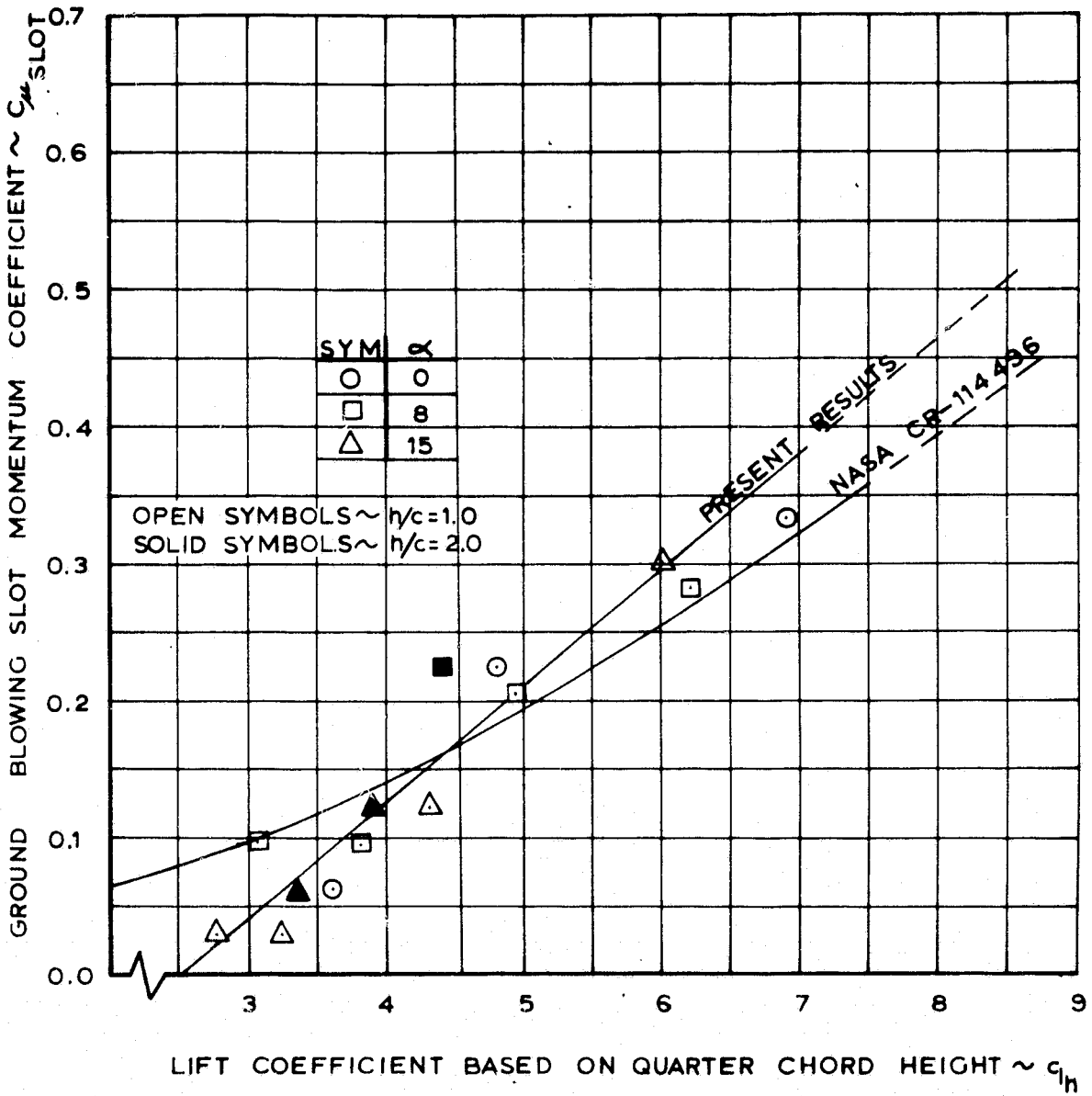
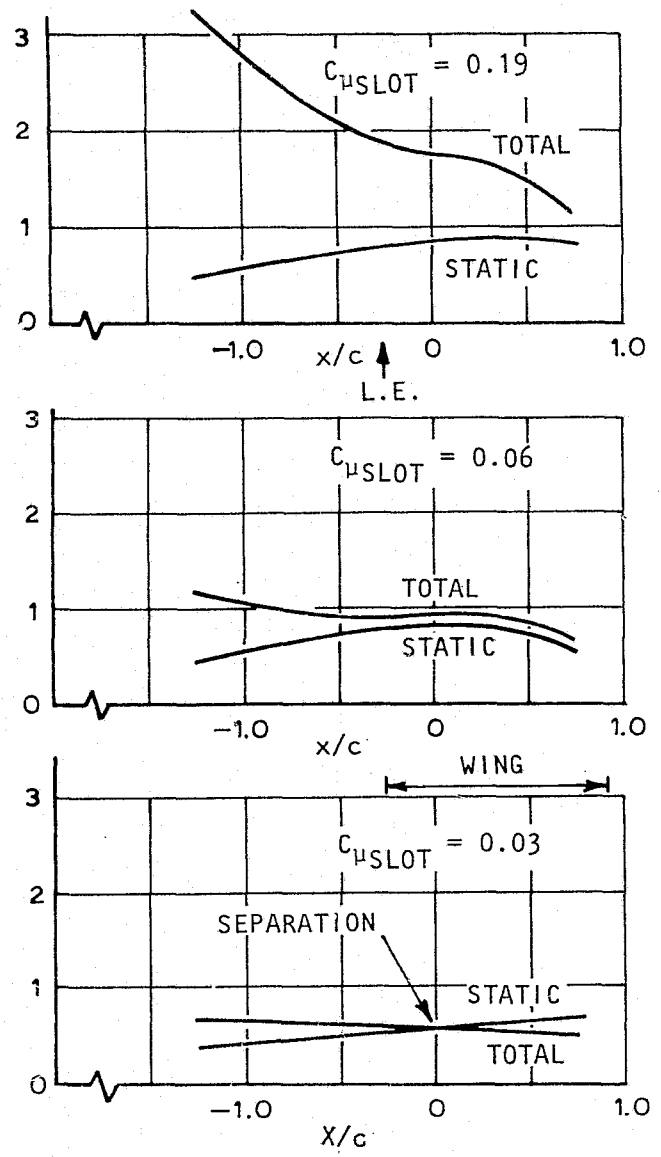
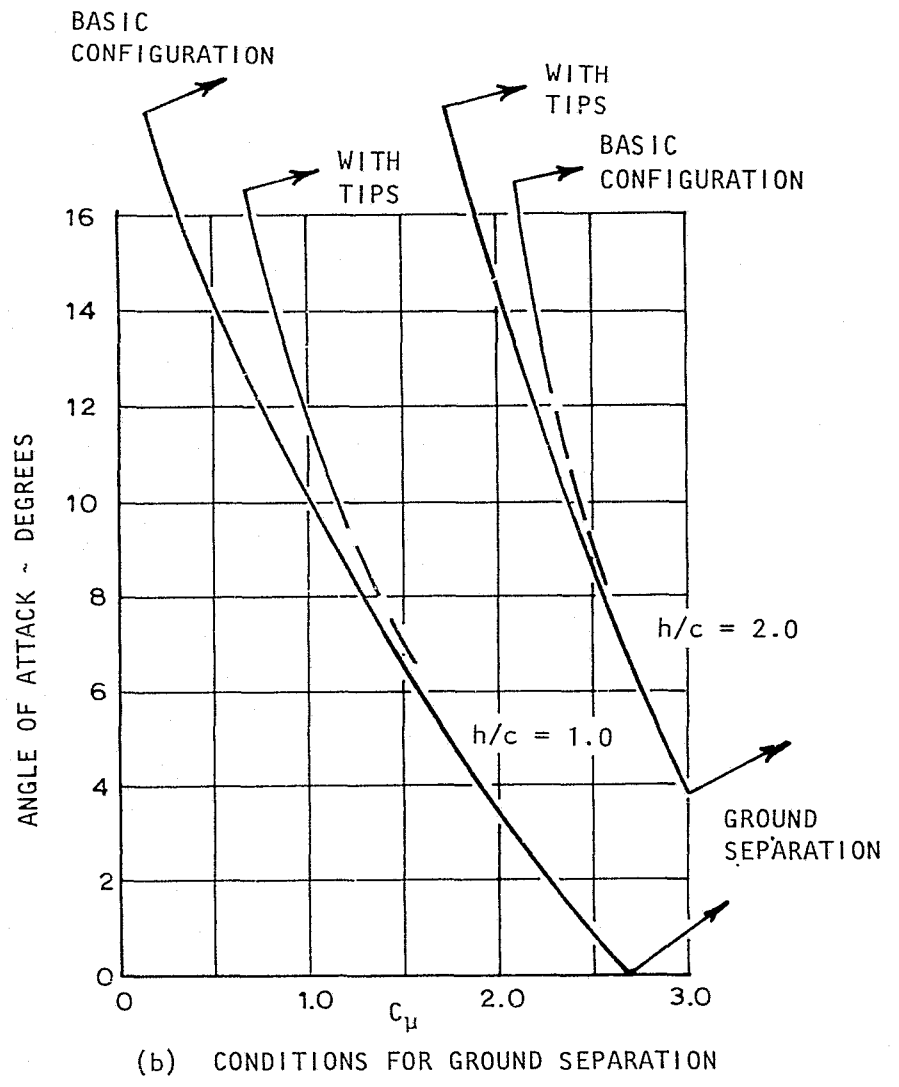


FIGURE 6.5 BLOWING BLC REQUIREMENTS FROM LIFT CONSIDERATIONS

PRESSURE COEFFICIENT ~ C_p



(a) TYPICAL PRESTON TUBE AND STATIC READINGS, $C_{\mu} = 0.4$, $\alpha = 15^\circ$



(b) CONDITIONS FOR GROUND SEPARATION

FIGURE 6.6 FLOW CONDITIONS AT THE GROUND.

ANGLE OF ATTACK ~ DEGREES

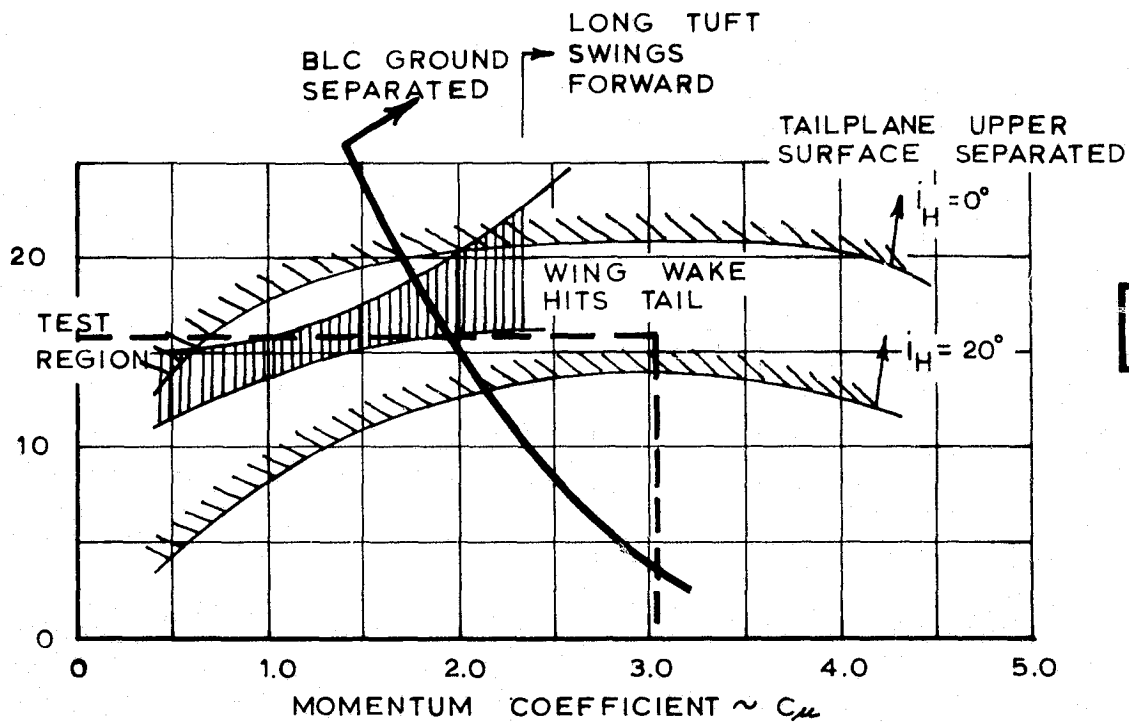
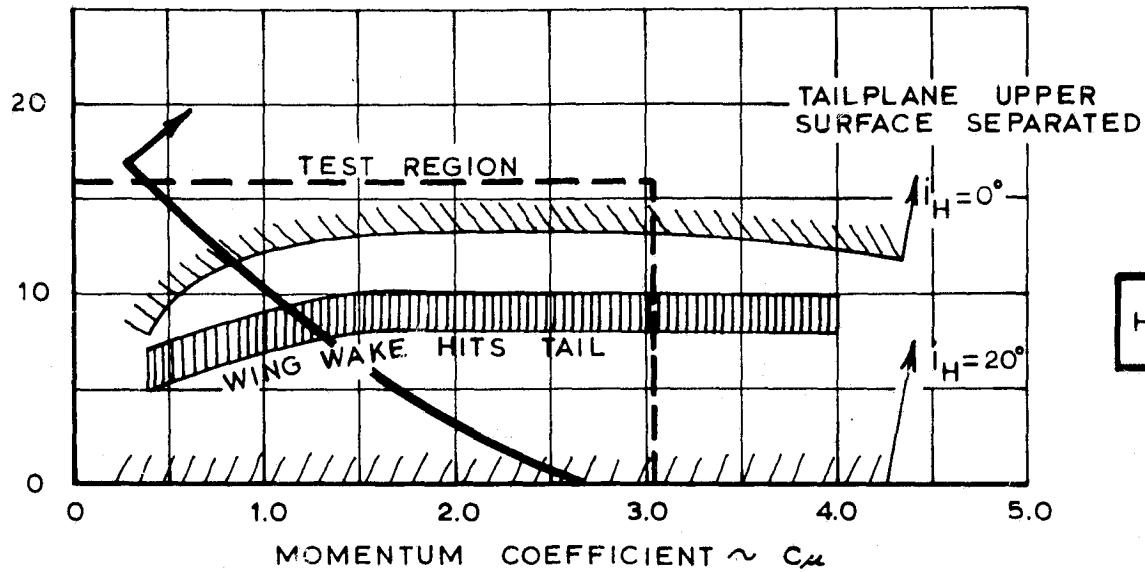


FIGURE 6.7 CONDITIONS FOR NEGATIVE TAIL STALL AND WING WAKE PENETRATION (MOVING GROUND)

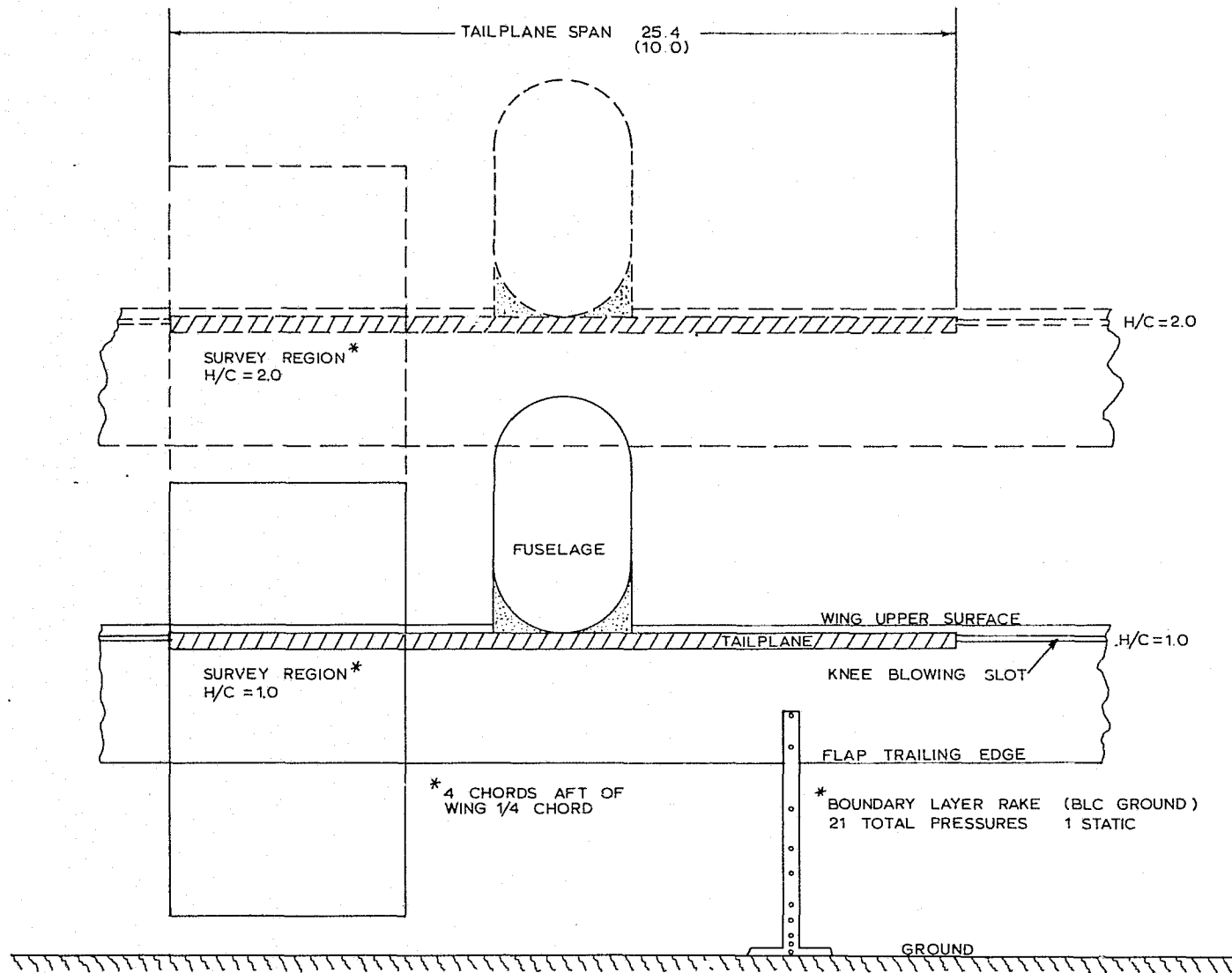


FIGURE 6.8 GEOMETRY OF TAILPLANE AND FLOW MEASUREMENTS

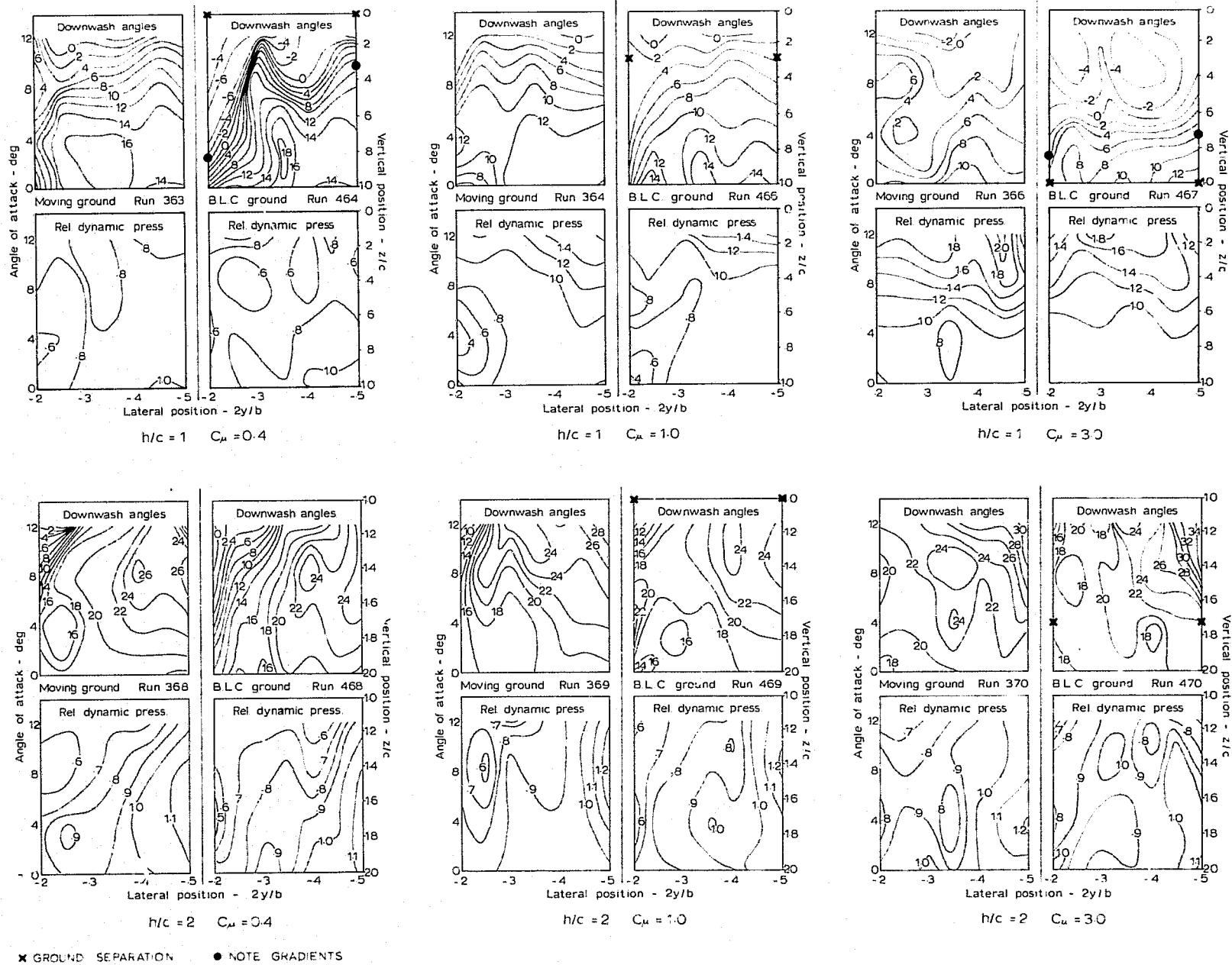


FIGURE 6.9 FLOW ANGLES AT THE TAIL: BLOWN AND MOVING GROUND

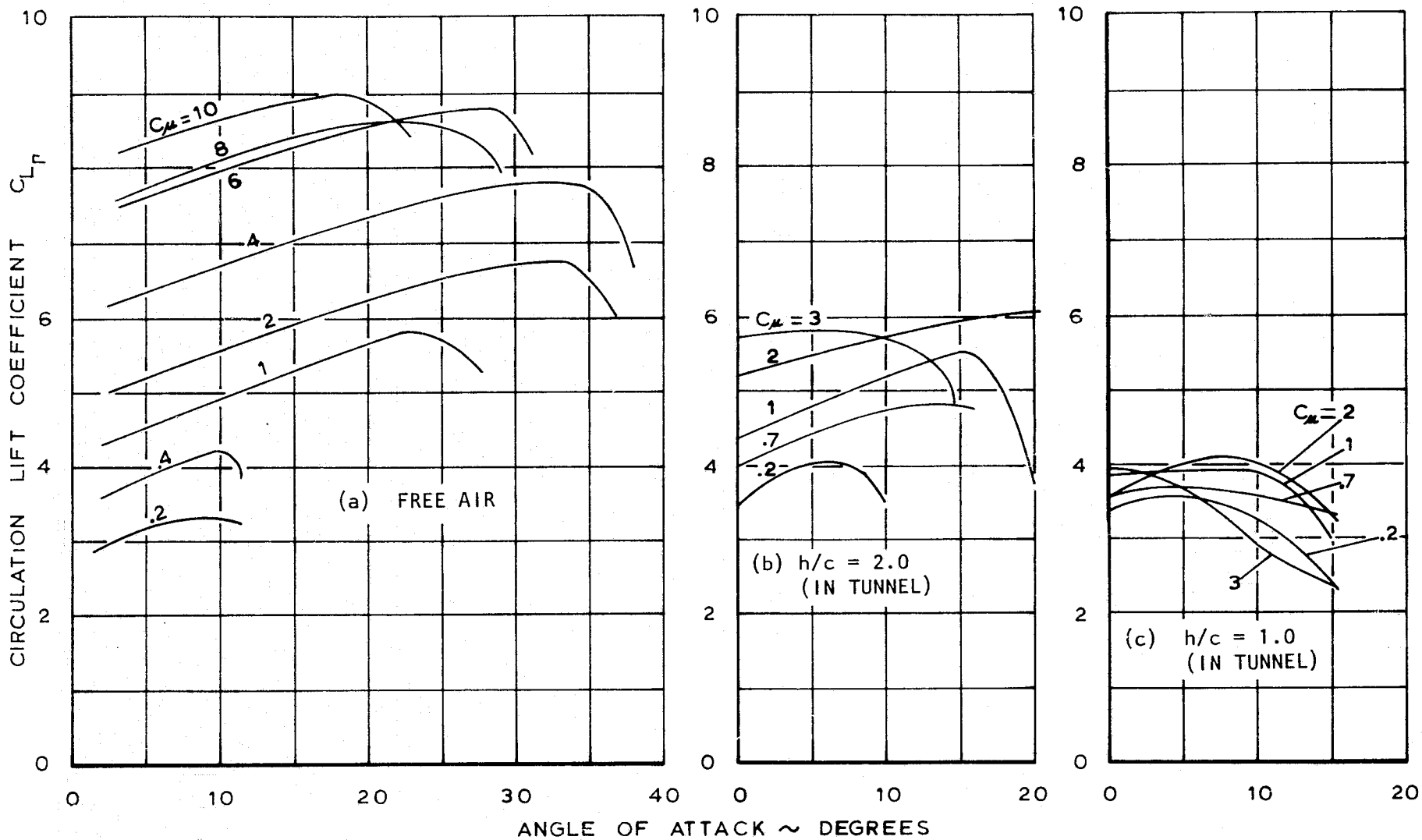


FIGURE 6.10 LIMIT LIFT IN GROUND EFFECT (BASIC CONFIGURATION - MOVING GROUND)

- ◇ MOVING BELT GROUND PLANE
- ◆ BOUNDARY LAYER CONTROL GROUND PLANE

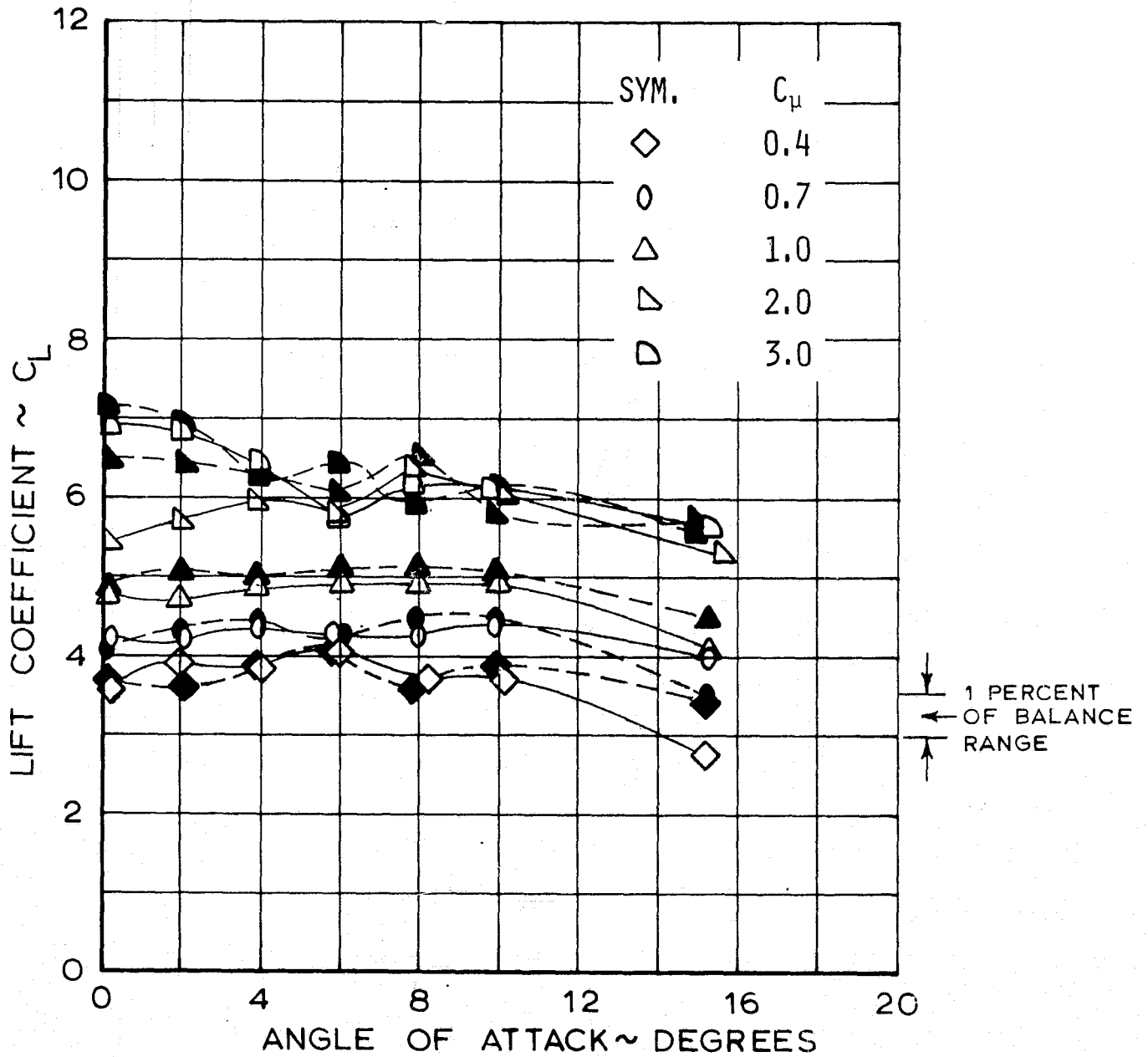


FIGURE 7.1 BASIC LIFT DATA IN GROUND EFFECT $h/c = 1$, BASIC WING WITH SLATS (A-1)

- ◇ MOVING BELT GROUND PLANE
- ◆ BOUNDARY LAYER CONTROL GROUND PLANE

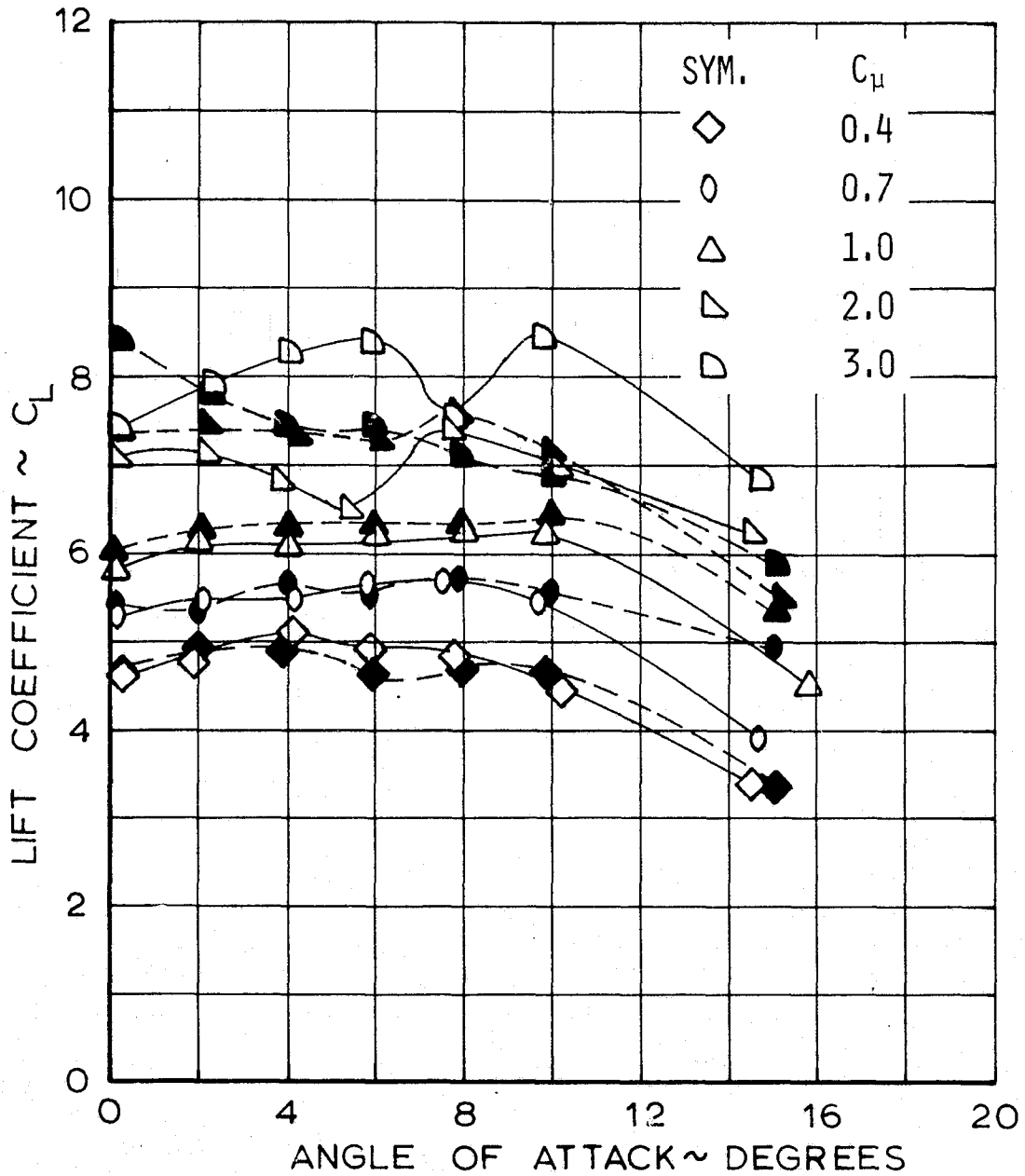


FIGURE 7.2 BASIC LIFT DATA IN GROUND EFFECT $h/c=1$, WITH TIPS, FULLY SLATTED (B)

◇ MOVING BELT GROUND PLANE
 ◆ BOUNDARY LAYER CONTROL GROUND PLANE

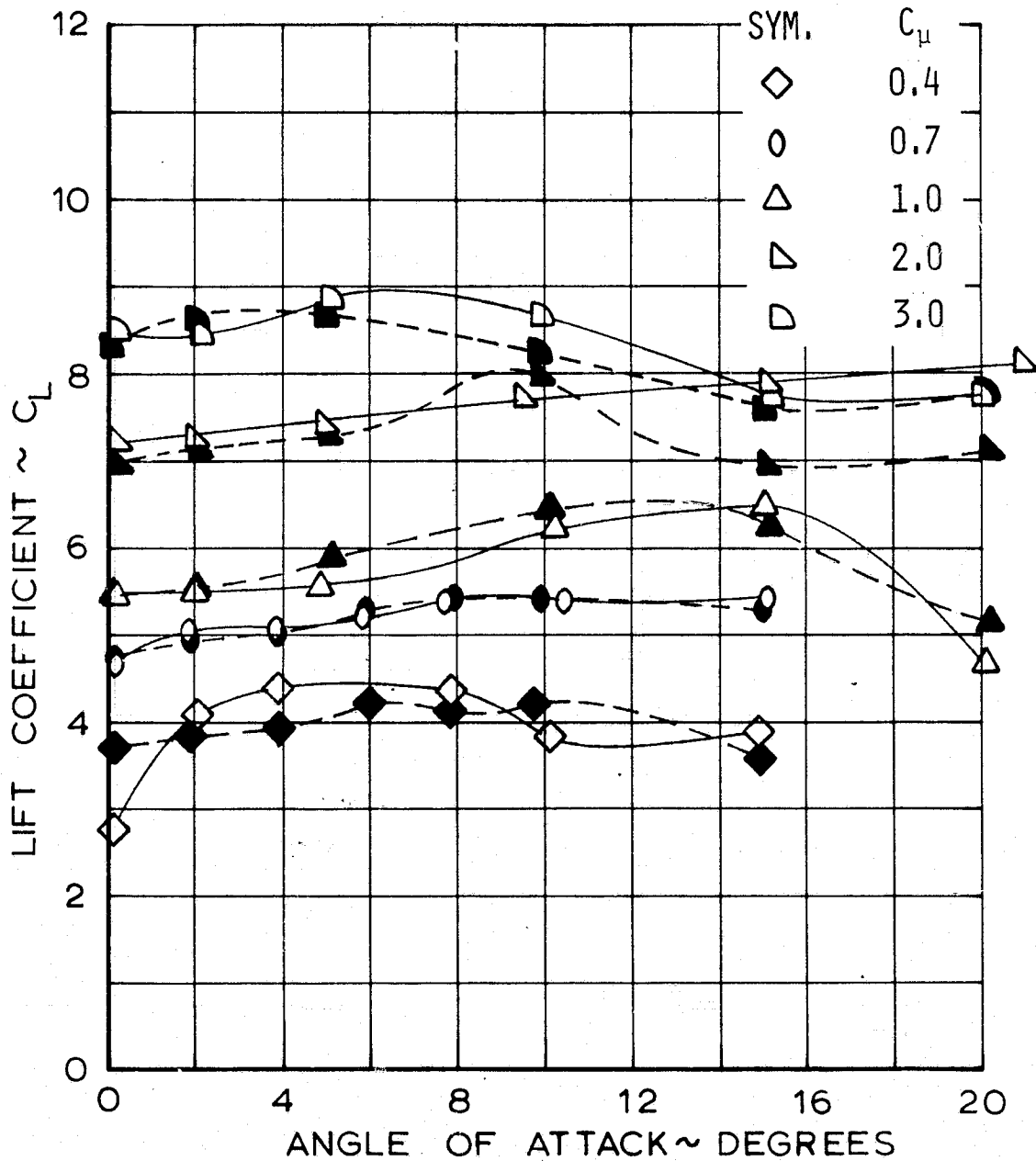


FIGURE 7.3 BASIC LIFT DATA IN GROUND EFFECT $h/c = 2$, BASIC WING WITH SLATS (A-1)

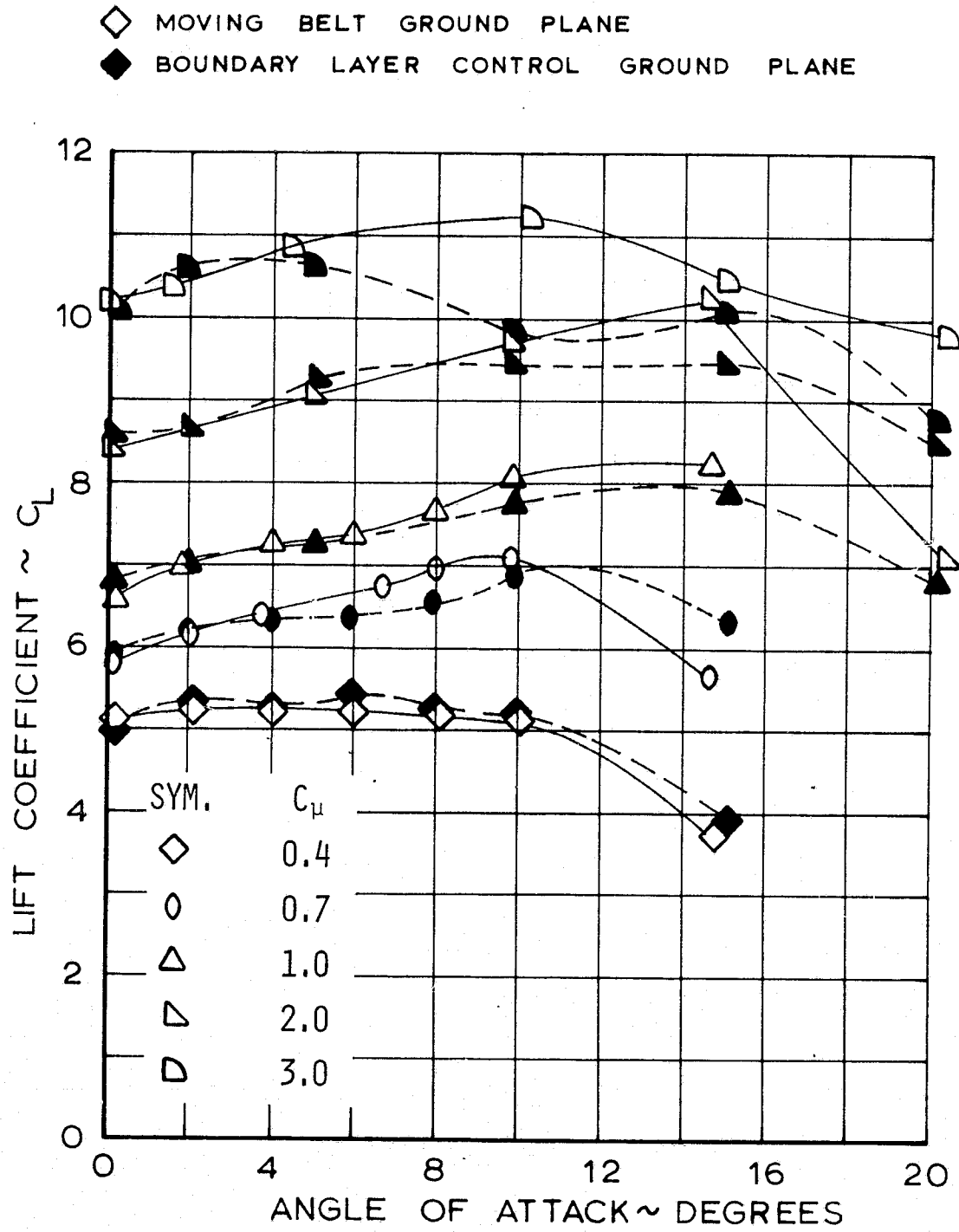


FIGURE 7.4 BASIC LIFT DATA IN GROUND EFFECT $h/c = 2$, WITH TIPS, FULLY SLATTED (B)

- ◇ MOVING BELT GROUND PLANE
- ◆ BOUNDARY LAYER CONTROL GROUND PLANE

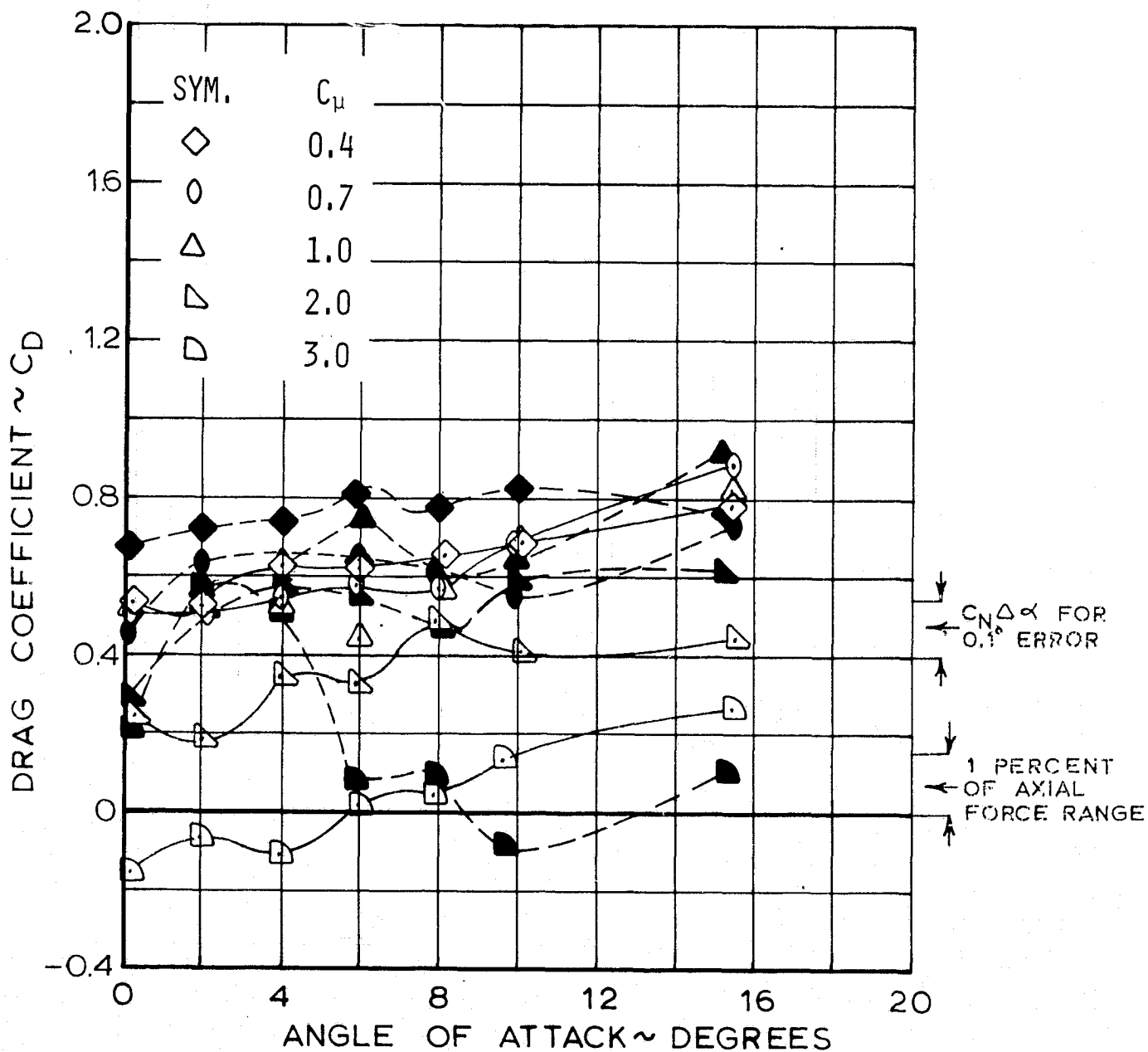


FIGURE 7.5 BASIC DRAG DATA IN GROUND EFFECT $h/c = 1$, BASIC WING WITH SLATS (A-1)

◇ MOVING BELT GROUND PLANE
 ◆ BOUNDARY LAYER CONTROL GROUND PLANE

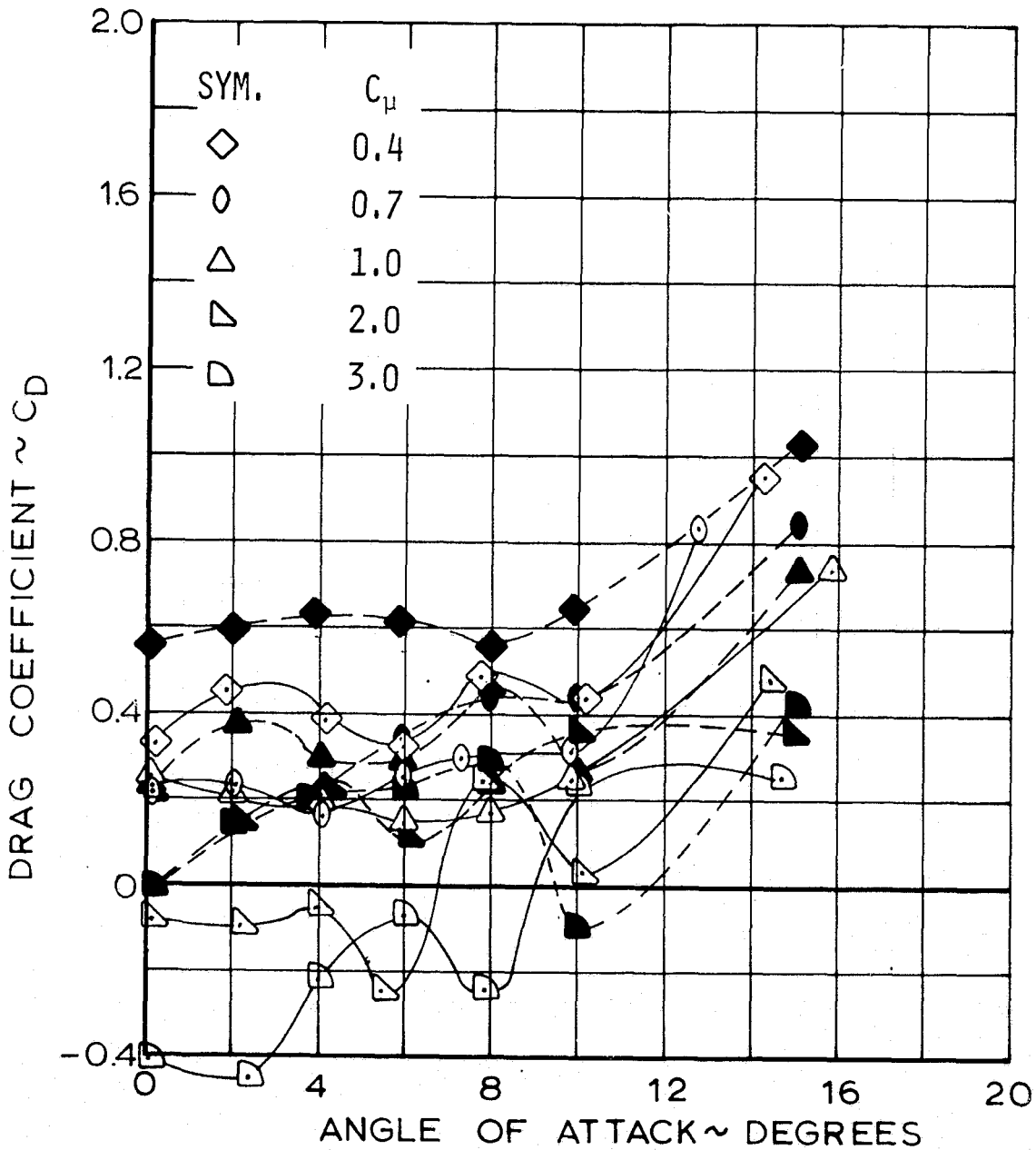


FIGURE 7.6 BASIC DRAG DATA IN GROUND EFFECT $h/c = 1$, WITH TIPS, FULLY SLATTED (B)

◇ MOVING BELT GROUND PLANE
 ◆ BOUNDARY LAYER CONTROL GROUND PLANE

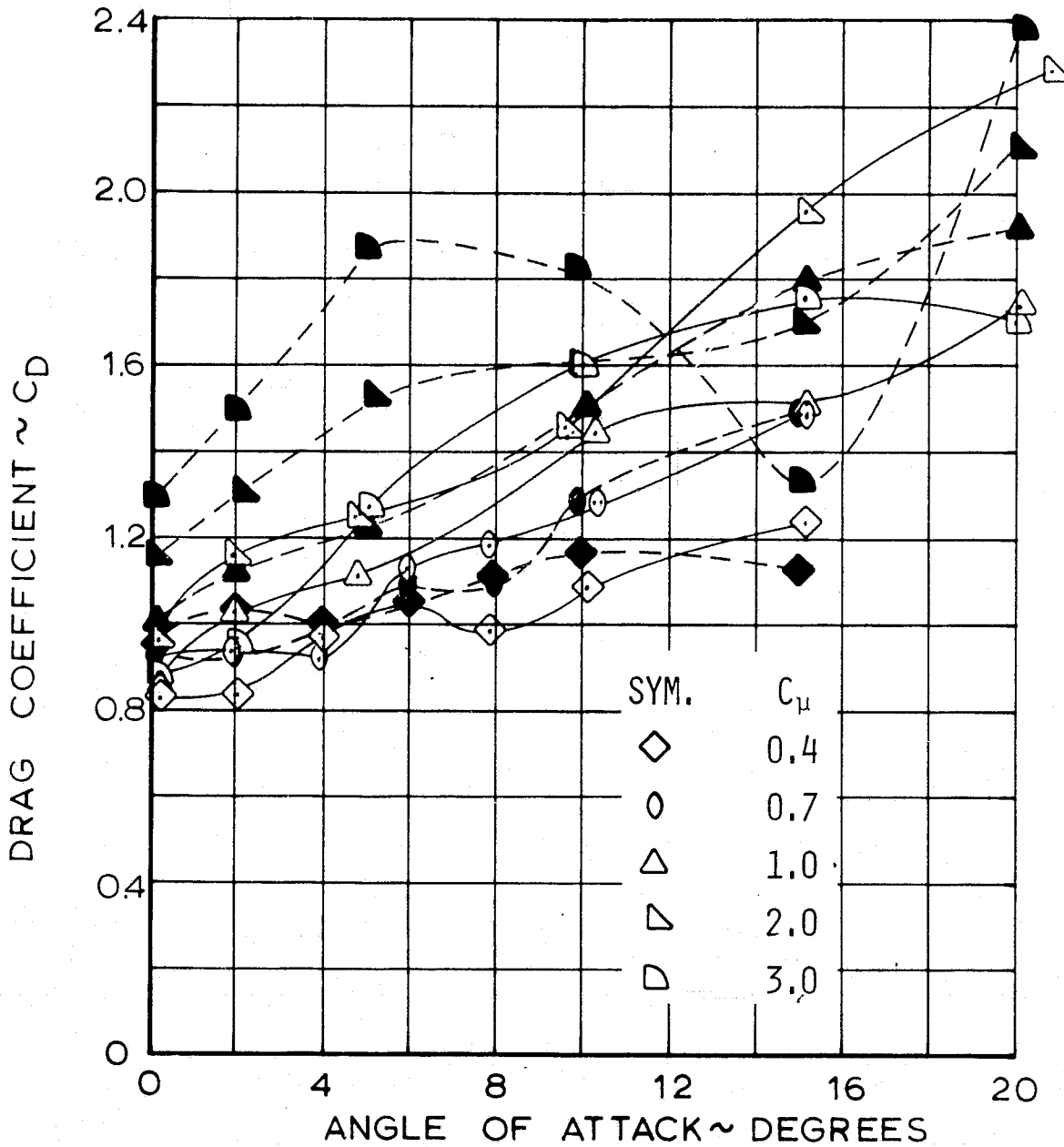


FIGURE 7.7 BASIC DRAG DATA IN GROUND EFFECT $h/c=2$, BASIC WING WITH SLATS (A-1)

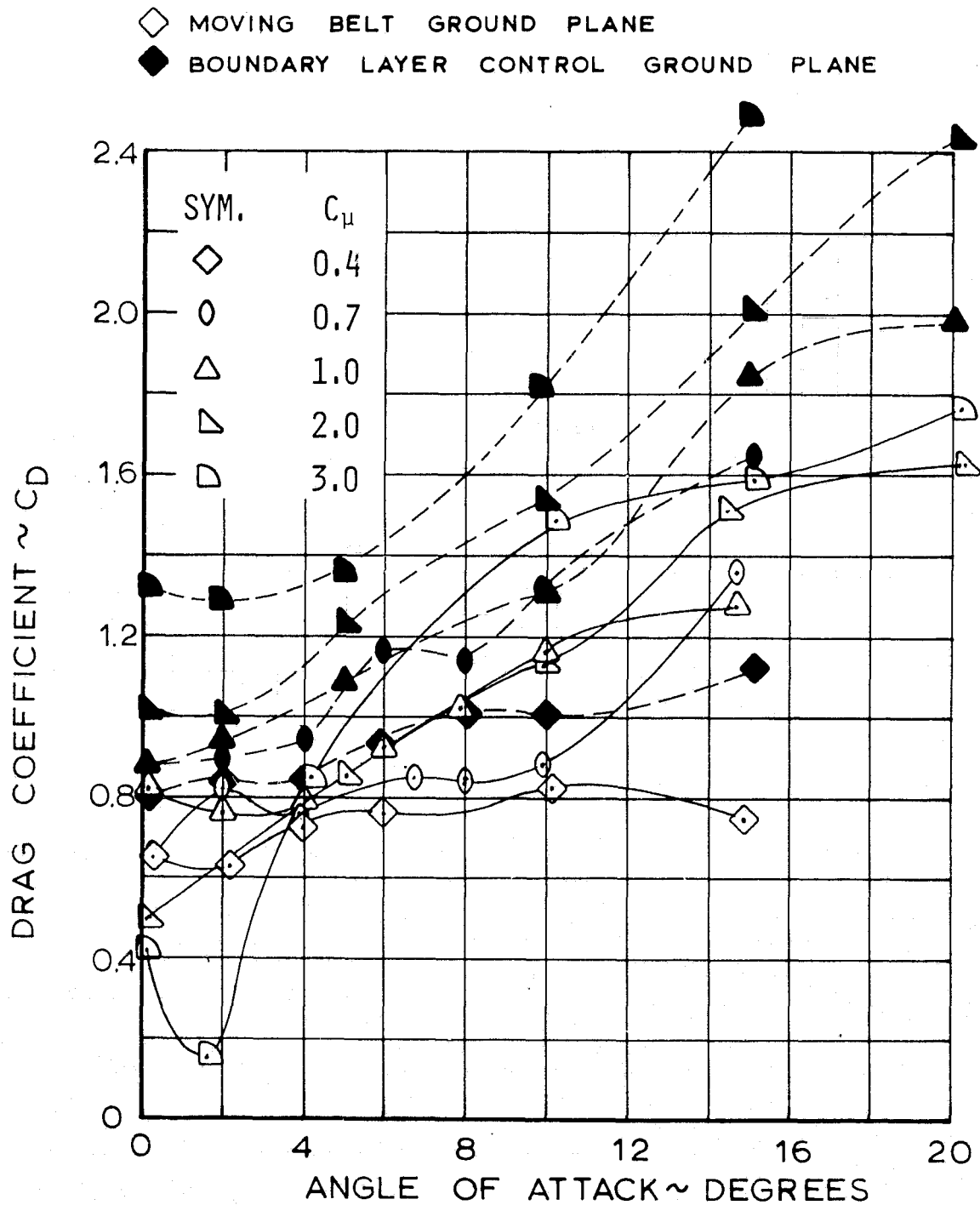





FIGURE 7.8 BASIC DRAG DATA IN GROUND EFFECT $h/c = 2$, WITH TIPS, FULLY SLATTED (B)

 F FLOOR SEPARATES AT HIGHER ANGLES
 T NEGATIVE TAIL STALL AT HIGHER ANGLES
 TAIL STRIKES GROUND AT HIGHER ANGLES

OPEN SYMBOLS - MOVING BELT
 FILLED SYMBOLS - BLC FLOOR
 TAGGED SYMBOLS - FIXED GROUND

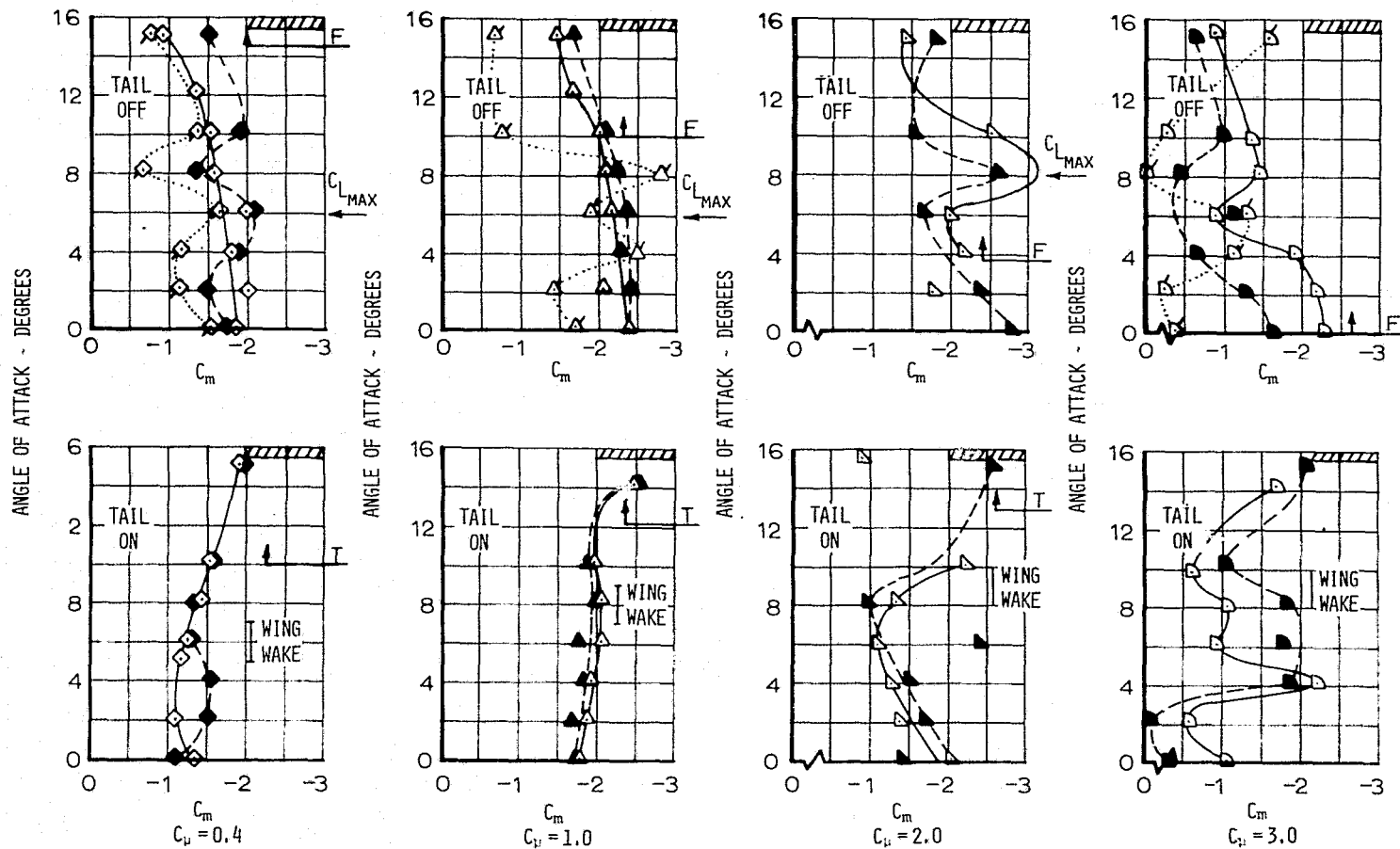


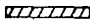


FIGURE 7.9 PITCHING MOMENTS IN GROUND EFFECT, $h/c = 1.0$, BASIC CONFIGURATIONS (A-1, A-2)

 F FLOOR SEPARATES AT HIGHER ANGLES
 T NEGATIVE TAIL STALL AT HIGHER ANGLES
 TAIL STRIKES GROUND AT HIGHER ANGLES

OPEN SYMBOLS - MOVING BELT
 FILLED SYMBOLS - BLC FLOOR
 TAGGED SYMBOLS - FIXED GROUND

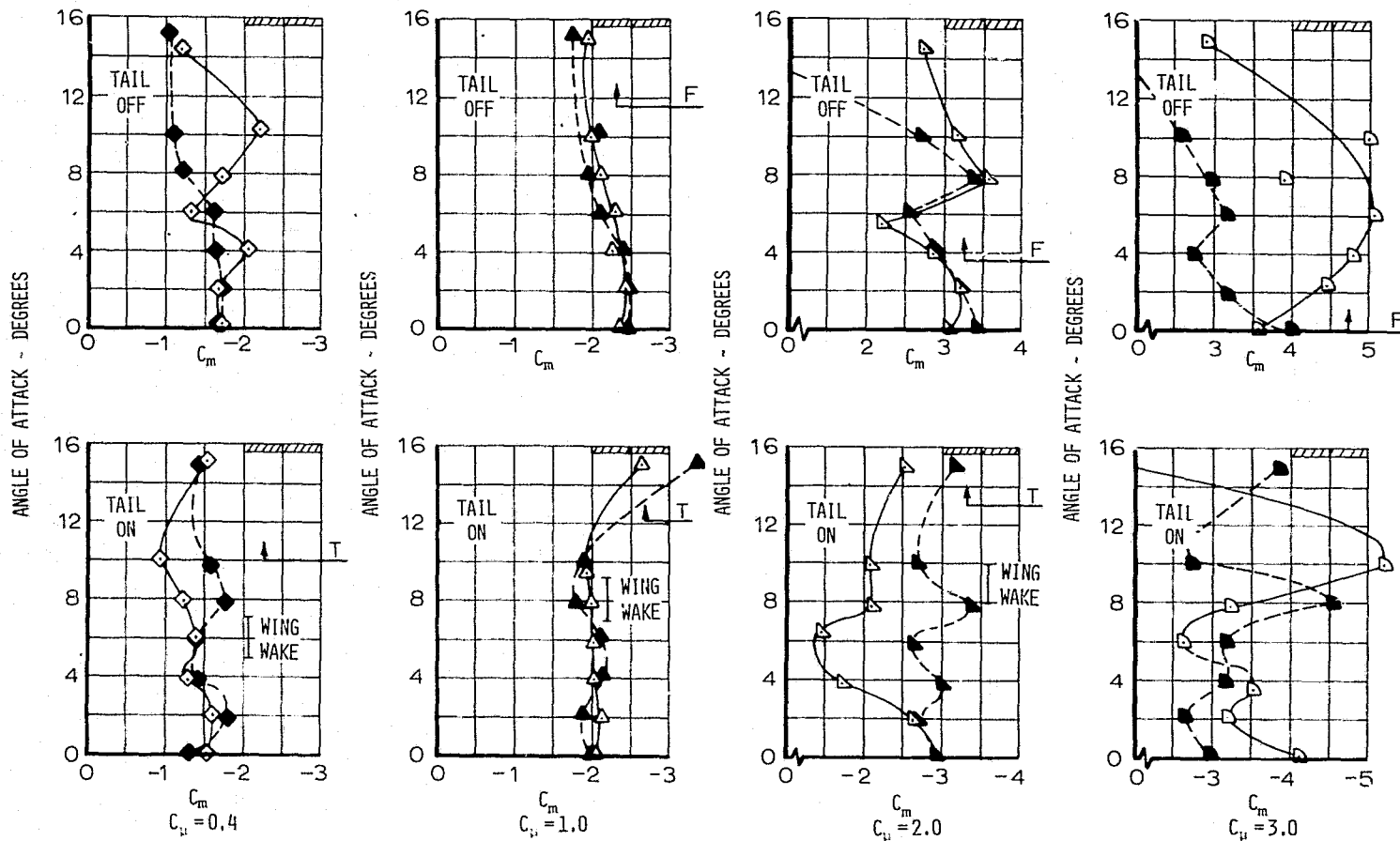


FIGURE 7.10 PITCHING MOMENTS IN GROUND EFFECT, $h/c = 1.0$, CONFIGURATIONS WITH TIPS (B, C)

F FLOOR SEPARATES
AT HIGHER ANGLES

T NEGATIVE TAIL STALL
AT HIGHER ANGLES

OPEN SYMBOLS - MOVING BELT

FILLED SYMBOLS - BLC FLOOR

TAGGED SYMBOLS - FIXED GROUND

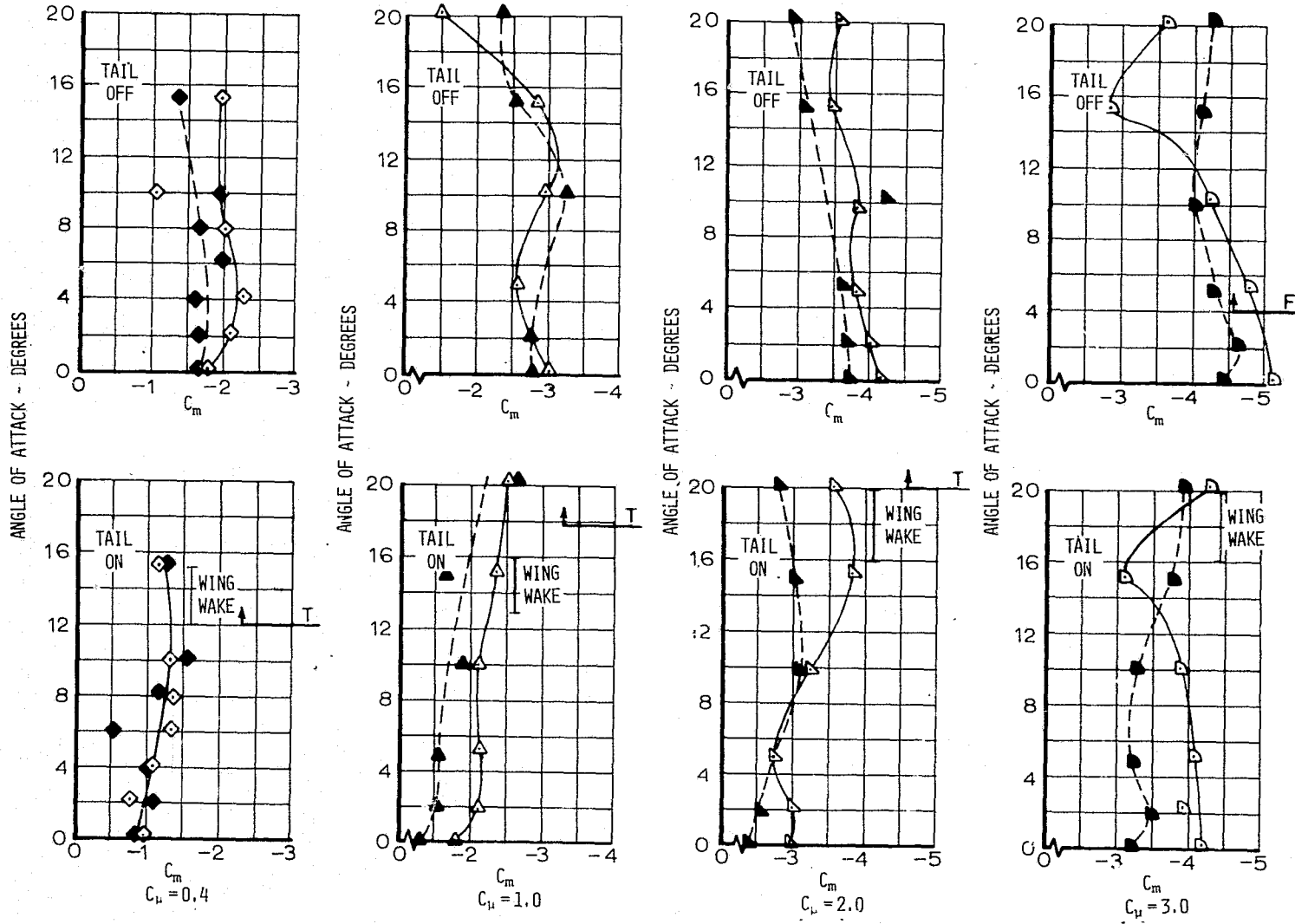
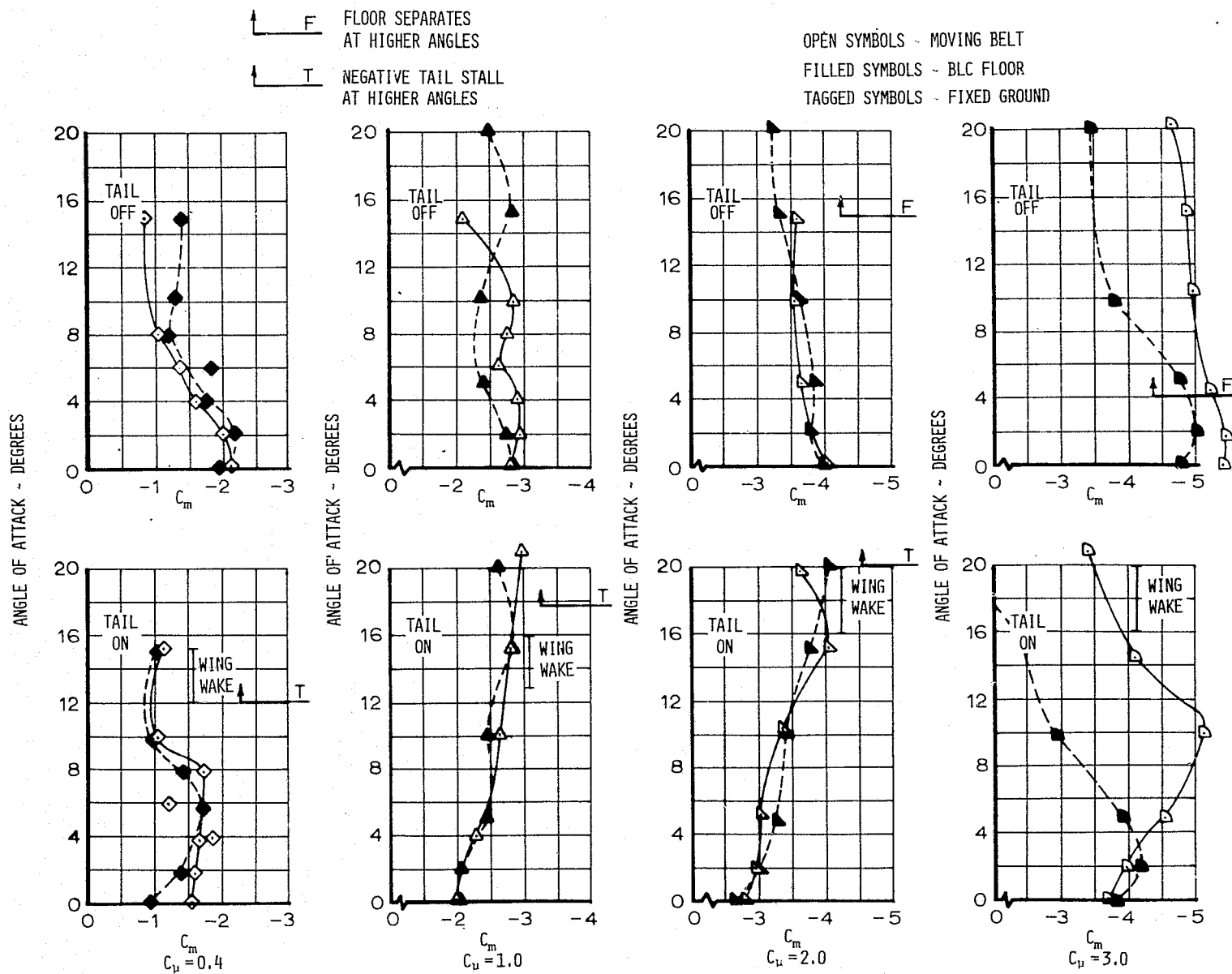


FIGURE 7.11 PITCHING MOMENTS IN GROUND EFFECT, $h/c = 2.0$, BASIC CONFIGURATIONS (A-1, A-2)


 FIGURE 7.12 PITCHING MOMENTS IN GROUND EFFECT, $h/c = 2.0$, CONFIGURATIONS WITH TIPS (B, C)

$\alpha \backslash C_{\mu}$	0.4		1.0		3.0	
	STD. RUN	FOR ATTACHMENT	STD. RUN	FOR ATTACHMENT	STD. RUN	FOR ATTACHMENT
0°	1.0135	--	1.0288	1.018	1.0377	≥1.09
8°	1.0173	1.008	1.0311	1.015	1.0442	≥1.09
15°	1.0041	1.013	1.0301	1.035	1.0408	?

BLC
BLOWING
PRESSURE
RATIO

$\alpha \backslash C_{\mu}$	0.4		1.0		3.0	
	STD.† RUN	AT ATTACHMENT	STD.† RUN	AT ATTACHMENT	STD.† RUN	AT ATTACHMENT
0°	3.6	3.45 (EST)	4.8	4.6	6.9 ϕ	NO DATA
8°	3.8*	3.7	4.95 ϕ	4.4	6.2*	NO DATA
15°	2.85*	3.2	4.35*	4.95	6.0*	NO DATA

MODEL
LIFT
COEFFICIENT

† Equals moving ground, by definition.

ϕ C_{Lmax}

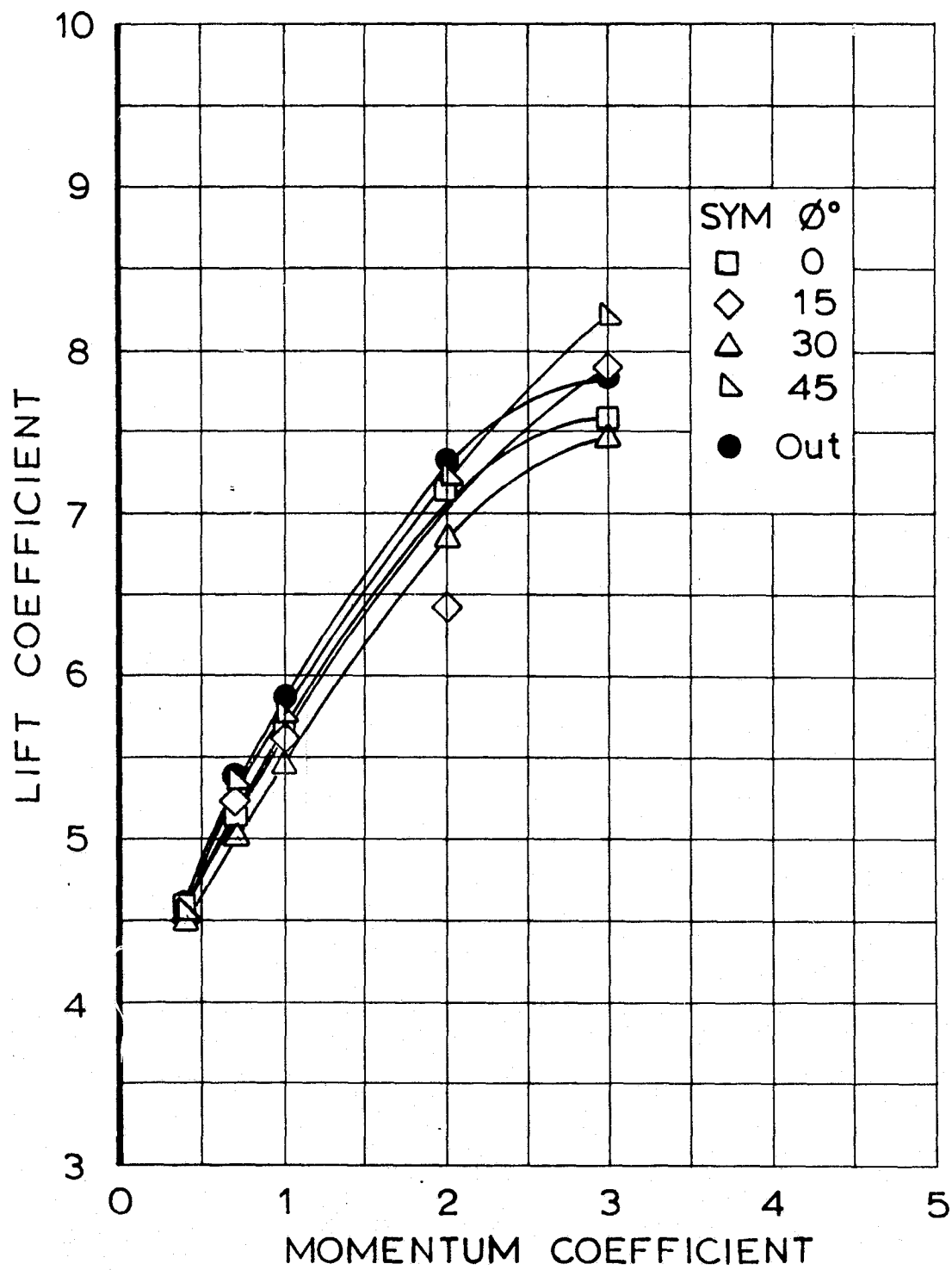
* Beyond C_{Lmax}

FIGURE 7.13 GROUND BLOWING PRESSURES FOR FLOW ATTACHMENT AND POSSIBLE ASSOCIATED LIFT RESULTS.

CONFIGURATION : A1

H/C = 1

ALPHA = 0



CONFIGURATION : A1

H/C = 1

ALPHA = 0

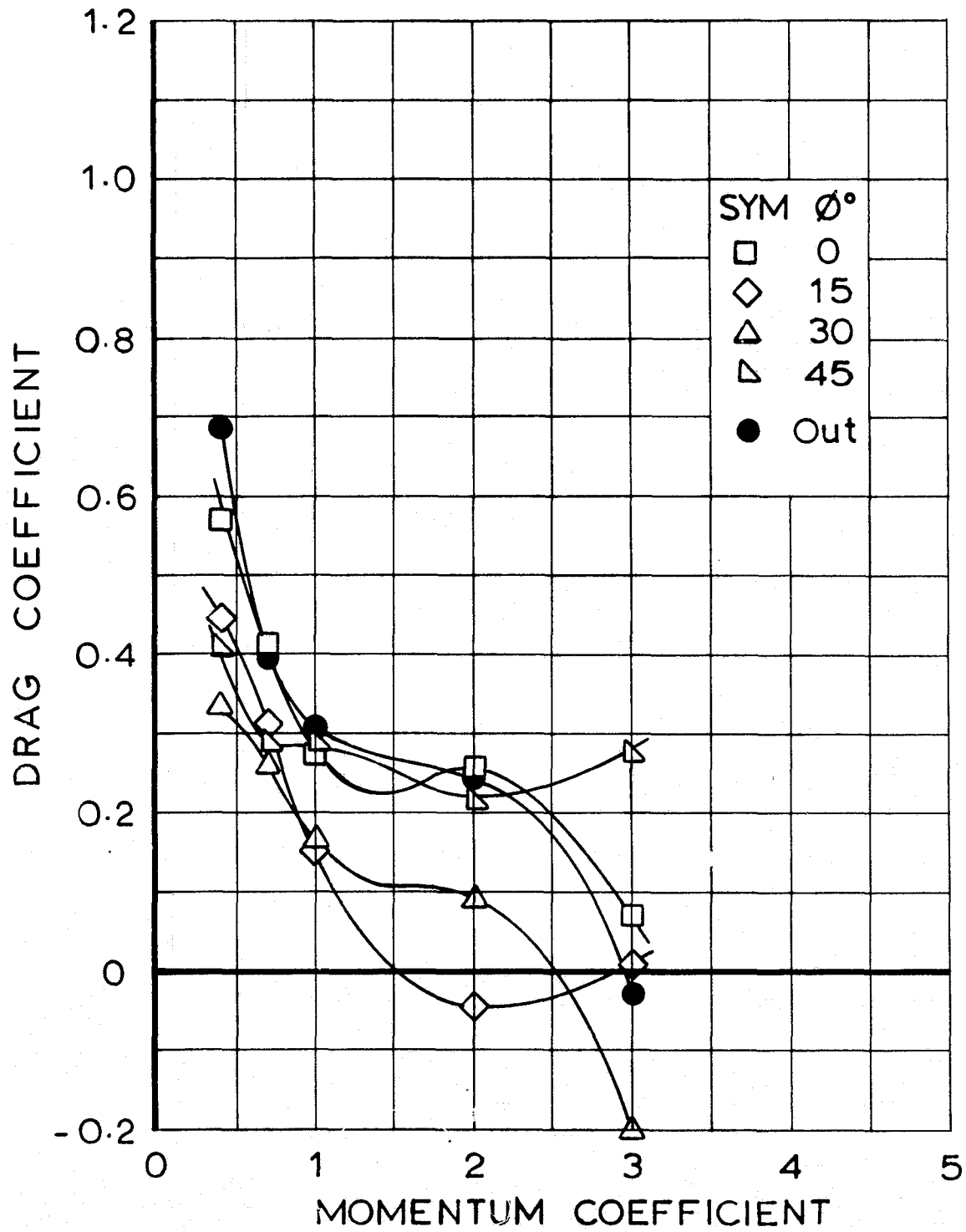


FIGURE 7.15 EFFECT OF SUPPORT STRUT FAIRINGS ON DRAG, $h/c=1$

CONFIGURATION : A1

H/C = 1

ALPHA = 0

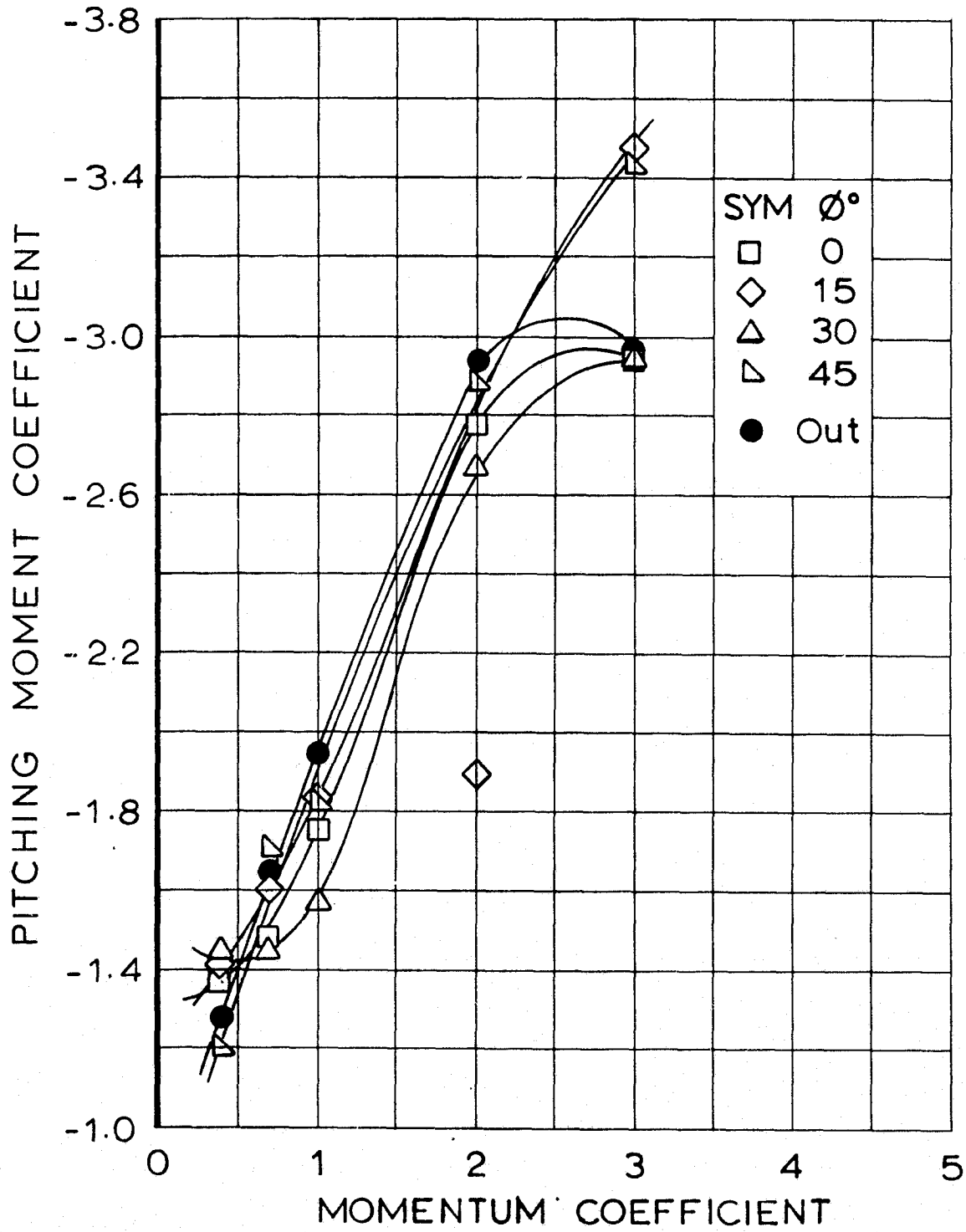


FIGURE 7.16 EFFECT OF SUPPORT STRUT FAIRINGS ON PITCHING MOMENT, $h/c = 1$

CONFIGURATION : A1

H/C = 2

ALPHA = 0

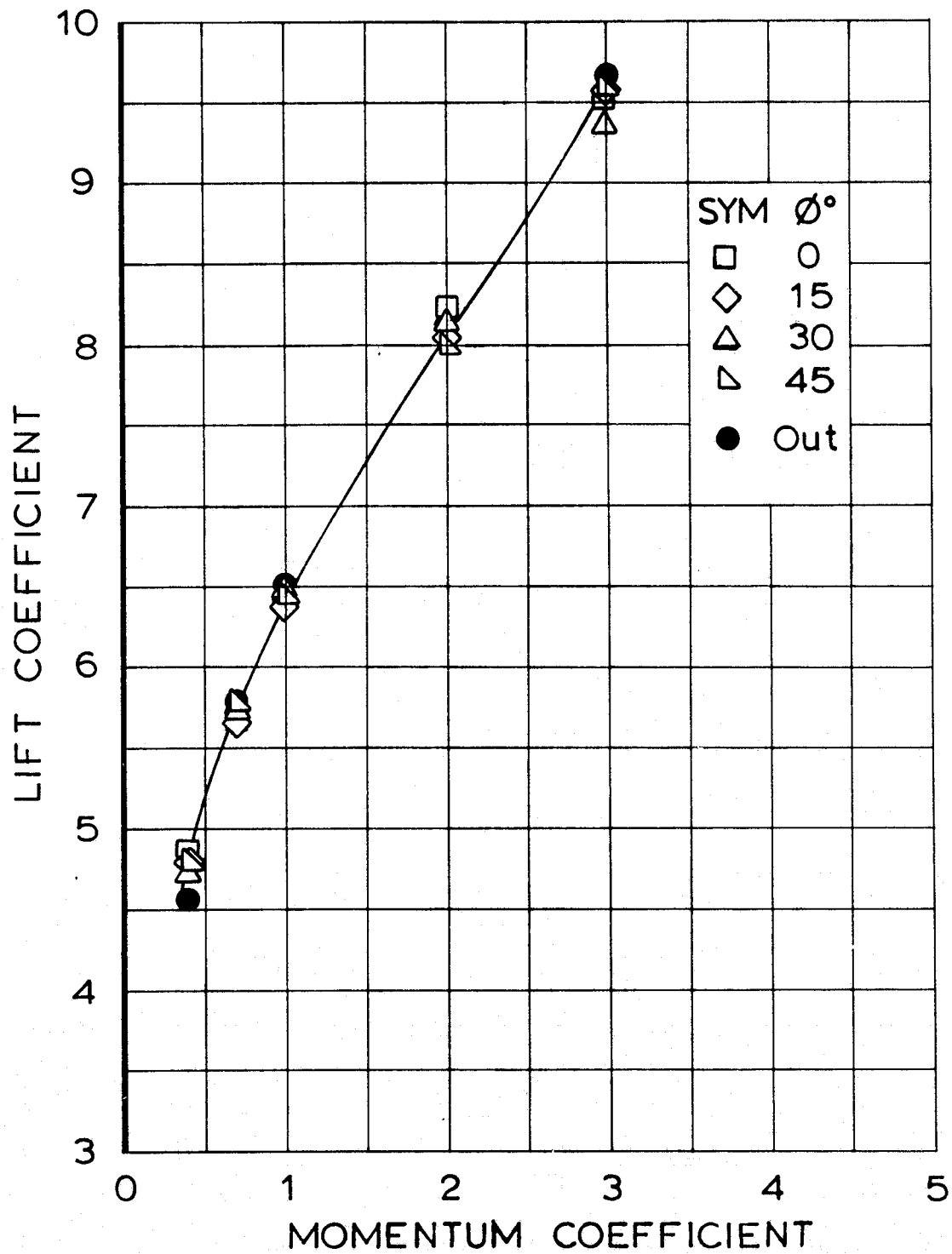


FIGURE 7.17 EFFECT OF SUPPORT STRUT FAIRINGS ON LIFT, $h/c = 2$

CONFIGURATION : A1

H/C = 2

ALPHA = 0

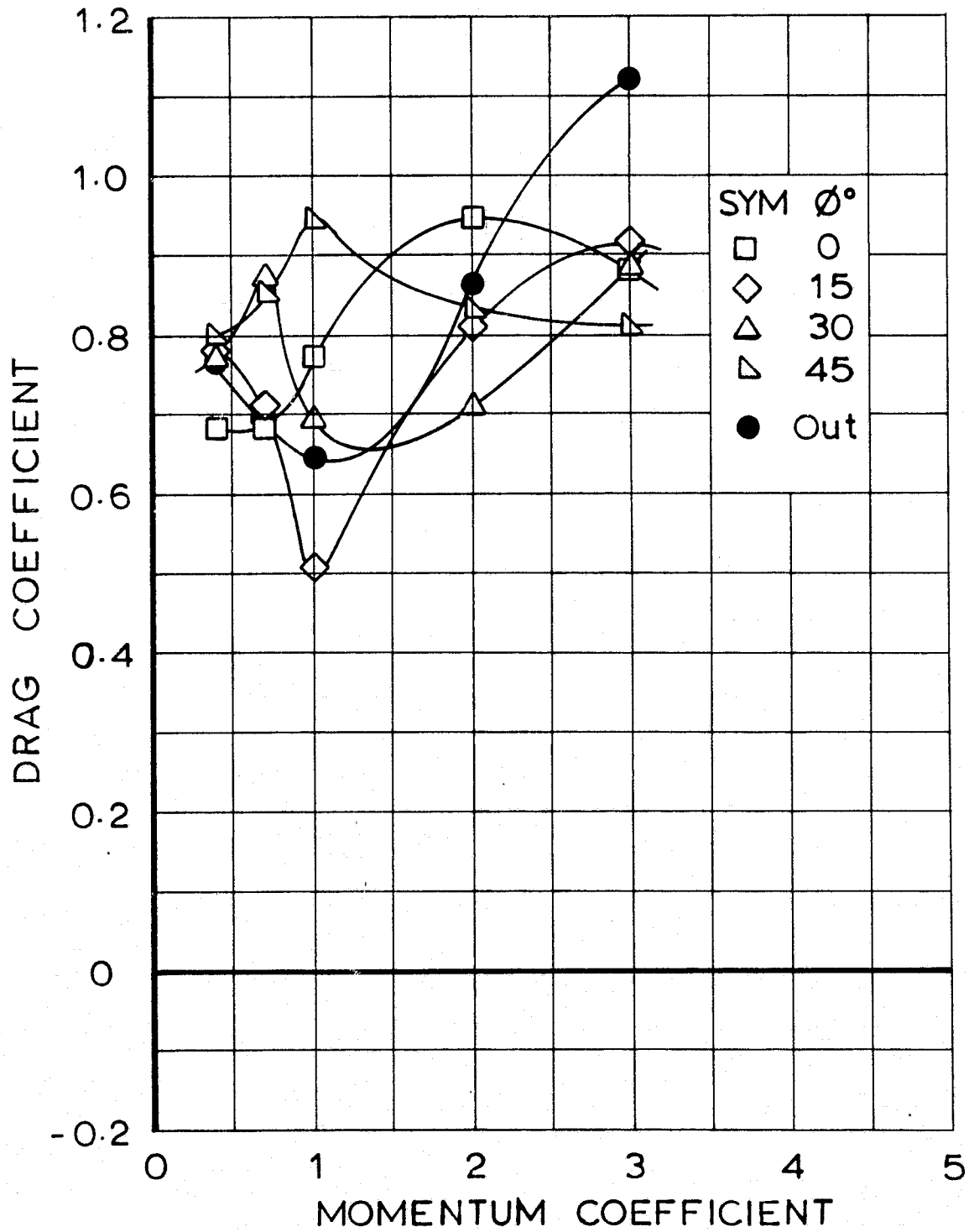


FIGURE 7.18 EFFECT OF SUPPORT STRUT FAIRINGS ON DRAG, h/c = 2

CONFIGURATION: A1

H/C = 2

ALPHA = 0

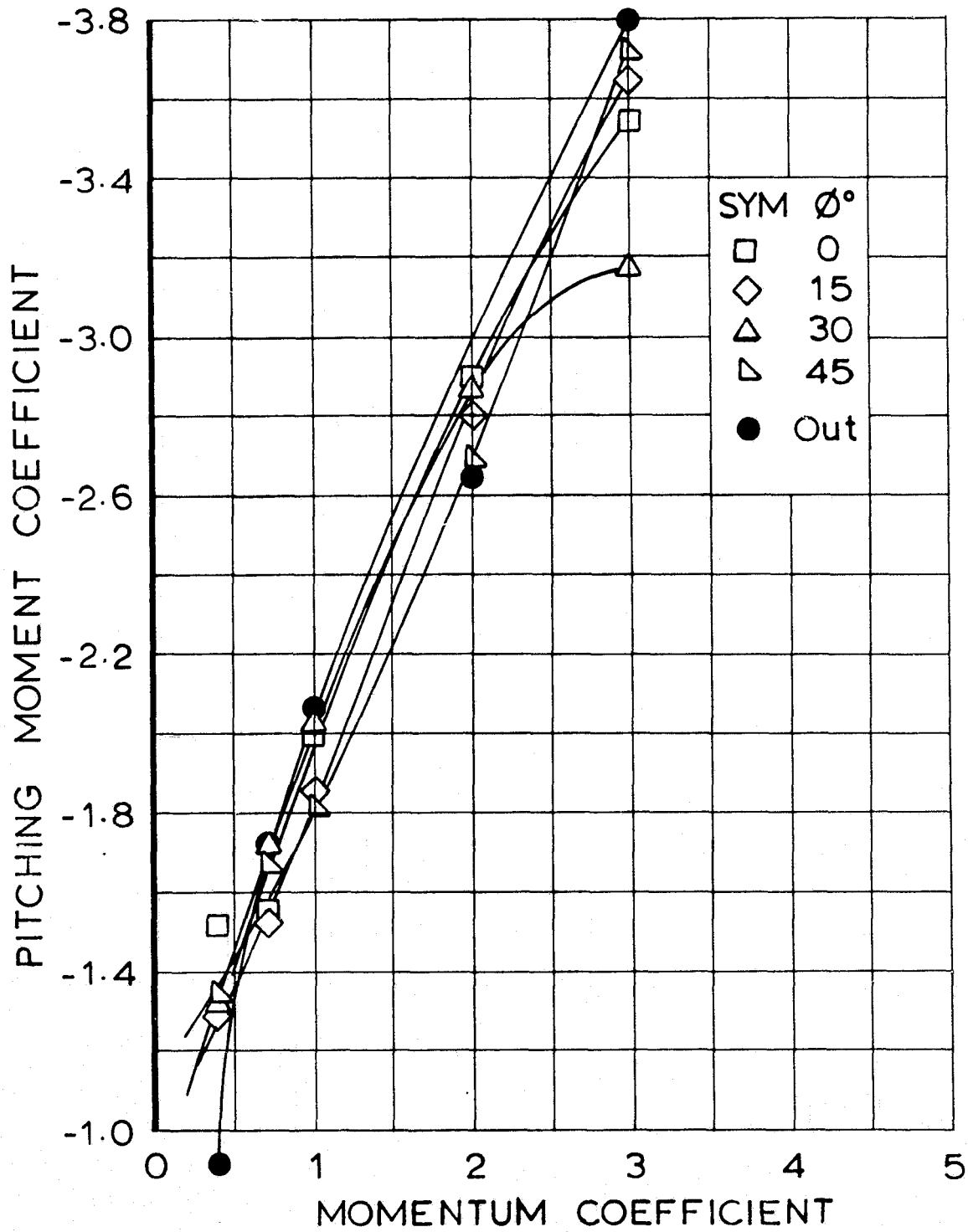


FIGURE 7.19 EFFECT OF SUPPORT STRUT FAIRINGS ON PITCHING MOMENT, $h/c = 2$